Reply to review comments

We thank the reviewers and James Menking for assessing this manuscript and for their time and effort. The useful comments by the referees are much appreciated and helped to improve the presentation of our results.

The original review comments are given below in black, our reply in blue, and quotes from the revised manuscript in olive. All page and line numbers given below refer to those given in the originally submitted MS. During revisions, we also slightly adjusted the design of the figures. Further we adjusted the names of the experiments to better reflect changes in the model set-up. Please find attached to this reply a revised manuscript where proposed changes are highlighted.

Reviewer 1

This paper describes the long-term evolution of CO_2-pulse experiments in the Bern3D EMIC on CO_2, $\delta^{13}C$, $\Delta^{14}C$. For this aim, especially the airborne fraction of these three variables are analysed, e.g. by a fit of a sum of 5 exponential functions. Furthermore, principal components of EOF are used to investigate the distribution of the signal in the ocean. The main target is the understanding of atmospheric $\delta^{13}C$ of CO_2 as is so far measured in ice cores covering the last 150 kyr. There, an offset in $\delta^{13}C$ between the penultimate and last glacial maximum (PGM, LGM) still lacks an explanation (Schneider et al., 2013; Eggleston et al., 2016), but also $\delta^{13}C$ during millennial-scale dynamics are also briefly discussed (Bauska et al., 2016, 2018). The paper is on a good way. Its focus is on the evolution of the isotopic signatures following a carbon pulse are to my knowledge new, while the long-term evolution of CO_2 pulses has already been analysed elsewhere (Colbourn et al., 2015; Lord et al., 2016), although with a different model. However, I still have a list of (partly major) points, in which I suggest the draft is revised in order to clarify open issues or sharpen its message. They are in detail:

We thank the reviewer for the support and thoughtful comments.

1. The main aim of this study is to better understand the observed evolution of $\delta^{13}C$ in the Earth system (as such explicitly written at the beginning of section 3) with special focus on the atmosphere. I therefore suggest to sharpen (and shorten) the introduction focusing on the available atmospheric $\delta^{13}C$ data (Schneider et al., 2013; Eggleston et al., 2016; Bauska et al., 2016, 2018), and delete the lengthly citations/discussion of CO_2 over the last 800 kyr. Maybe, also add a figure, which shows the relevant $\delta^{13}C$ data, both on glacial/interglacial and millennial-time scales, to give the reader an idea about the magnitudes of changes and the unsolved problems.

We deleted the sentence concerned with the CO_2 over the last 800 kyr. Concerning an additional figure we argue that in the literature plenty of such figures can be found (e.g. Schneider et al., 2013; Eggleston et al., 2016; Bauska et al., 2016, 2018). In order to not overload the manuscript we refrain from adding another figure.

2. At the end of the abstract (and maybe once in the discussion) volcanism is mentioned as a likely cause for the $\delta^{13}C$ offset between PGM and LGM. However, I believe no details on volcanism as assumed in the model are given. Is there a (constant?) volcanic CO_2 flux and what is its $\delta^{13}C$ signature? This final sentence of the introduction should be backed up with a more in-depth discussion, how this conclusion has been drawn. Right now on page 20 all examples given seemed to be not enough to explain the data, so an imbalance of weathering, volcanic, and burial fluxes seems to be the only possible solution, however the scenario mentioned to be the most likely one is not been investigated in detail. Maybe your insights on $\delta^{13}C$ can guide you to prescribe necessary changes in boundary conditions in such a way that the simulated $\delta^{13}C$ explains the offset between PGM and LGM (e.g. how needs volcanism change (in terms of its $\delta^{13}C$ signature and/or in its CO_2 release?) to generate the observed offset). This would be a real breakthrough.

We included information in the methods section (p.4, l.14) to illustrate how volcanic weathering in the model is implemented. It now reads:

Input fluxes by "weathering" of P, ALK, DIC, DI^{13}C, and Si are added uniformly to the coastal surface ocean. At the beginning of transient simulations, the global input fluxes of these compounds are set equal to the burial fluxes diagnosed at the end of the model spin-up. These input fluxes are jointly denoted as "weathering flux". These

1

fluxes are further attributed to weathering of organic material, of $CaCO_3$, of $CaSiO_3$, and to volcanic CO_2 out gassing. The flux of P is assigned to weathering of organic material and related C and ALK fluxes are computed by multiplication of the P flux with the Redfield ratios P:C:Alk = 1:117:-17 for organic material. Similarly, the Si flux is assigned to $CaSiO_3$-weathering and the related ALK flux is computed using Si:ALK=1:2 based on the simplified equation for $CaSiO_3$-weathering: $2CO_2 + H_2O + CaSiO_3 \rightarrow Ca^{2+} + 2HCO_3^- + SiO_2$ (Colbourn et al., 2013). The remaining ALK flux is attributed to $CaCO_3$-weathering with the stoichiometric ratio C:ALK=1:2 following from $CO_2 + H_2O + CaCO_3 \rightarrow Ca^{2+} + 2HCO_3^-$. The volcanic flux is the remaining flux needed to balance the C input flux. The diagnosed fluxes at the end of the spin up are 0.24 GtC yr^{-1} for weathering of organic material, 0.14 GtC yr^{-1} for $CaCO_3$ weathering, 0.08 GtC yr^{-1} for volcanic CO_2 outgassing, and 6.96 Tmol Si yr^{-1} for $CaSiO_3$-weathering. The isotopic signature of the weathering carbon corresponds to the respective signature of the burial fluxes and amounts to $\delta^{13}C$ = -9.2 ‰, intermediate between isotopically light organic carbon ($\delta^{13}C$ = -20.5 ‰) and heavier $CaCO_3$ ($\delta^{13}C$ = 2.9 ‰).

We changed the part of the discussion about long-term imbalances (p.20), please see our reply to the short-comment by James Menking for details. We are currently conducting additional experiments to investigate how volcanism would need to change to generate the observed offset in $\delta^{13}C$. These simulations are not yet done and including them here would be beyond the scope of this manuscript.

3. My understanding of the results here and of Lord et al. (2016) is, that the pulse size (labeled P here and E in the other paper) is also important for the time-dependent airborne-fractions. At least, this is the case for CO_2. For that reason E has been included in the sum of 5 exponential functions that fit to the model results in Lord et al. (2016) (their Eq 3), but E is missing in the fit used here (Eq 4). I believe this needs to be revised. I acknowledge that there is a subsection on the role of pulse size on page 14, but I am wondering why this is not included in the fitting equations. Maybe also compare airborne fraction of CO_2 with results shown in Colbourn et al. (2015); Lord et al. (2016). Any stricking difference?

The difference between Lord et al. (2016) eq. 3 and the IRF fit in this study eq. 4 is that Lord et al. (2016) fit the CO_2 concentration at time t in ppmv whereas we fit the remaining fraction (IRF) of the pulse at time t. Combining the definition of the IRF in eq. 1 and the IRF fit in eq. 4 in this study yields the same expression as shown in Lord et al. (2016) eq. 3 with the difference that in our case we have a fraction (a_0) which remains constantly in the atmosphere. In Lord et al. (2016) experiments were run long enough (1 mio years) so that all emissions have been removed from the atmosphere (see e.g. Fig. 4 in Lord et al. (2016)).

In the results section we added a comparison to airborne fractions of CO_2 in Colbourn et al. (2015) (p.9, l.5):

In comparison to others, our results show, up to a few percent, lower remaining fractions for the 5000 GtC pulse (p5000) than results presented by Colbourn et al. (2015) and Lord et al. (2016). The remaining airborne fraction of the CO_2 perturbation is 5 % and less after 100 kyrs in all studies.

4. While Lord et al. (2016) and Colbourn et al. (2015) had only future emission in mind (and therefore the starting point has always been the modern carbon cycle), here changs in the past are in focus. One section is missing, which discusses, if (and at best how) everything said here depends on the background state of the carbon cycle. Especially, these detailed changes in $\delta^{13}C$ discussed (PGM vs LGM; millennial-scale) happened during more glacial conditions. I understand all pulse experiments have been analysed starting from pre-industrial conditions. At best, everything needs to be repeated from LGM background, but saying that, I realize, that this might double all efforts, and might be too much for the paper at hand. However, it should be shown with at least one perturbation experiment, how things are different when starting from glacial background, in order to give the reader a feeling of the size of such a potential background dependency.

This is an important question which we did not address in detail in the manuscript. Running all experiments again under glacial conditions is beyond the scope of this manuscript, as already forcing the model into a sensible glacial state is not trivial. However, we add results from two existing additional runs and split Fig. 1 into two figures to illustrate the state dependence of our results. The new figure becomes Fig. 2 in the revised manuscript. We list the two runs in Table 1 and introduce them in the methods section by adding the following on p5, l.23:

We also assess the influence of glacial climate boundary conditions and of a different land biosphere model. In two additional simulations, LGM_{500} and $4box_{500}$, the Bern3D setup and spin-up is as in WEA_{500}, except that an atmospheric CO_2 concentration of 278 ppm instead of 284.7 ppm is used and the pulse is released in the first timestep of simulation year 100 instead of distributed over the year. The model configuration includes reactive sediments and weathering feedbacks. A four-box terrestrial biosphere model (Siegenthaler and Oeschger, 1987), that allows for CO_2 fertilization, instead of LPX-Bern is coupled to the Bern3D in these runs. In LGM_{500} the model is forced by glacial boundary conditions instead of preindustrial conditions as in $4box_{500}$ and in WEA_{500}. CO_2 is set to 180 ppm and northern hemisphere ice sheets are set to Last Glacial Maximum coverage (Peltier, 1994). It has to be noted, however, that by forcing the model with 180 ppm during spin-up leads to less carbon stored in the

ocean under LGM than PI conditions and results from LGM_{500} should be treated with some caution. Differences in results between WEA_{500} and $4box_{500}$ are due to differences in the two land biosphere models. Differences between $4box_{500}$ and LGM_{500} are exclusively due to differences in climatic boundary conditions.

In the results section we add on p12, l.34:

Next, we compare WEA_{500}, where LPX-Bern is used as land model, with $4box_{500}$, where a 4-box land biosphere is used. Differences in IRF($CO_{2,a}$) between WEA_{500} and $4box_{500}$ are due to the different land biosphere models. The four-box land biosphere model takes up less of the CO_2 perturbation than LPX-Bern. The root mean squared deviation in IRF($CO_{2,a}$) from the two simulations is less than 1 % of the perturbation. Differences are most pronounced between simulation year 1 and 10,000 (Fig. 6a). Differences in IRF($\delta^{13}C_a$) (Fig. 6b) are largest in the first decades after the pulse and the root mean square deviation in IRF($\delta^{13}C_a$) amounts to less than 1 % between the two simulations. Finally, we compare the simulations LGM_{500}, forced by glacial boundary conditions, and $B3D_{500}$, forced by preindustrial conditions. Differences between the two simulations are solely due to the difference in climate and CO_2 forcing. IRF($CO_{2,a}$) is lower by a few percent in LGM_{500} compared to $4box_{500}$. The difference is largest in the first 10 kyrs and up to 12 % of the perturbation. The RMSE between the two simulations amounts to ~2 %. The larger oceanic uptake in LGM_{500} than in $4box_{500}$ can be explained by the higher alkalinity simulated for LGM than for preindustrial conditions. A higher alkalinity implies lower values of the Revelle factor ξ and a larger carbon uptake capacity of the ocean. IRF($\delta^{13}C_a$) shows a similar pattern with lower values for the LGM background compared to the preindustrial background (cf. black dotted and dark violet dotted lines in Fig. 5b). The difference can be understood with the help of eq. 6; inserting the small glacial value for the atmospheric carbon inventory (381.6 GtC) in the nominator of the first term yields IRF$_\infty$($\delta^{13}C_a$)=0.027 compared to IRF$_\infty$($\delta^{13}C_a$)=0.032 when using the preindustrial value (589.4 GtC) in the equation. These estimates of IRF($\delta^{13}C_a$) are in good agreement with the results from LGM_{500} and $4box_{500}$, respectively (Fig. 2b). In summary, the influence of glacial compared to preindustrial boundary conditions on IRF($\delta^{13}C_a$ appears modest in our model.

In the discussion we add on p21 the following (see also our reply to the short-comment by James Menking:

We acknowledge that most of the idealized experiments presented here were run under preindustrial boundary conditions whereas cold glacial conditions prevailed during HS1 and HS4. A limited set of sensitivity simulations suggest that the IRFs for CO_2 and $\delta^{13}C$ are similar under preindustrial and glacial CO_2 in our model. The direct influence of lower atmospheric CO_2 on IRF($\delta^{13}C$) appears limited. Further work is needed to better quantify the dependency of IRFs on the climate state.

Nevertheless, our results suggest that a release of terrestrial carbon to the atmosphere, as sole mechanism for the CO_2 and $\delta^{13}C_{atm}$ excursion during HS4 and HS1 seems not very likely. Other mechanisms in addition to a terrestrial carbon release likely contributed to the reconstructed variations.

Further, references in the text are changed to account for the new Fig. 2. See attached diff for details on the changes.

5. Results (Table 2): I would expect the fit parameters also for $\Delta^{14}C$, and for all scenarios and not only for p500. Maybe they can also generalized by the consideration of E in the fitting functions, see point 3 above.

We now also provide fits for $\Delta\Delta^{14}C_{only}$ and $\Delta\Delta^{14}C_{dead}$. A generalization becomes difficult as soon as pulse sizes differ substantially (i.e. WEA_{500} vs. WEA_{5000}). This non-linearity is also visible in Fig. 4 and 5 of Lord et al. (2016).

6. When explaining why the airborne-fraction of $\delta^{13}C$ sinks at first more rapidly than that of CO_2, I believe this can be explained with the gross gas exchange (atmosphere-ocean), while for the CO_2 the net gas exchange (net oceanic uptake) is relevant, which is, as correctly written, slowed down by the carbonate chemistry (buffer or Revelle factor).

We prefer to keep our quantitative analysis which is derived in the appendix. We believe that the reviewer is referring to earlier work where the atmospheric budget for ^{13}C is solved by expressing change and fluxes in units of GtC ‰ yr^{-1}. The net air-sea flux for the isotopic perturbation is then be expressed by adding the product of the gross sea-to-air CO_2 flux times the air-sea isotopic disequilibrium and the product of the net air-to-sea CO_2 flux times the isotopic perturbation in the atmosphere (see for example eq. 16 and Tab. 3a in Joos and Bruno (1998)). The first term with the gross CO_2 flux and the air-sea isotopic disequilibrium dominates over the term with the net CO_2 flux during the first years after a perturbation. However, to understand why this is the case a similar analysis as given in the appendix is necessary.

7. Eq 5: Without saying that Eq 5 is wrong, I was intuitively expecting that the pulse size P might be relevant here. The buffer factor depends on the pulse size. This is explained on page 14, line 8ff under the heading "Influence of pulse size". In the main text we added a reference to the appendix, where eq. 5 is derived. Further, we removed 'P denotes again the pulse size' on p.10, l.9 which was mistakenly stated there. The sentence on page 10 line 11 is modified to read:

ξ varies with environmental conditions and increases with the size of the CO_2 perturbation. ξ is on the order of

10 for small pulse sizes. The dependency of IRF(CO_2) on the size of the carbon pulse is implicitly captured in the variable ξ.

8. I find the detailed discussion of C budget changes in GtC over time for one specific scenario p250 (page 13-14) not that interesting. It would be better, this is expressed in fractional changes (eg expressed as airborne fraction for the atmosphere), and the paper would especially benefit if it can be generalize from one scenario to more (all?), e.g. maybe by including the dependency on the pulse size.

Please note that Figure 2 (now Fig. 3) already shows the results for two simulations. We modified the text on p13 to make this clear to the reader:

Next, we discuss the budgets of the carbon and ^{13}C perturbations. Fig. 3 shows results for simulation WEA_{250}, with a pulse release of 250 GtC, and for simulation WEA_{-250}, with a pulse removal of 250 GtC. Differences between these two runs are clearly visible in Fig. 3, but the general evolution of the budgets is similar. In the following, we give numerical results for simulation WEA_{250}.

As the reviewer seems very interested in this issue, we added the figure below (Fig. 1) which illustrates the differences in responses for a range of simulations with different pulse sizes.
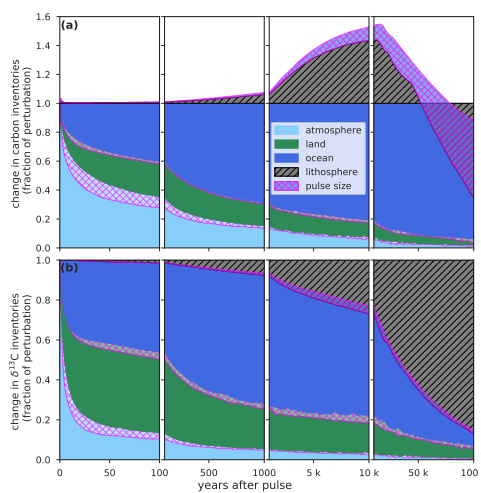

Figure 1: Changes in carbon and δ^{13}C reservoirs for pulse sizes -250 GtC to 500 GtC as fractional change. Pink area indicates the range from the pulse sizes.

9. Page 14, last sentence (on radiocarbon) does not make sense to me, e.g. the first part seems to say the opposite of the second part, maybe extend with details or revise.

We changed the sentence to read:

IRF($\Delta^{14}C_a$) is larger for $^{14}C_{-500}$ than for $^{14}C_{dead}$ on these very long time scales. This is because the perturbation in CO_2 and, in turn, the long-term perturbation in $\Delta^{14}C_a$ is the same for both experiments. However, the initial perturbation in $\Delta^{14}C$ - the denominator of the response function (see eq. 2) - is smaller in $^{14}C_{-500}$ than $^{14}C_{dead}$.

10. Discussion of millennial-scale changes (page 20, line 29ff): My reading of the papers of Bauska et al did not come to the conclusions, that they argue that the changes in CO_2 by 10 ppm and a decrease in δ^{13}C by 0.2 ‰ can be solely explained by carbon release from terrestrial sources, but they suggest alternative processes. Please revise this discussion of Fig 6 carefully.

We revised the sentence (p.20, l.32) to read:

A release of terrestrial carbon has been discussed as a possible cause of these events (Bauska et al., 2016, 2018). This is in accordance with what is stated in the discussion in Bauska et al. (2018) on page 7738

Further, we added a second panel to Fig. 6 (Fig. 7 in the revised manuscript) and expanded the discussion on this issue. Please see our answer to the comment by James Menking

11. Fig 1 has in some scenarios some abrupt (and unexpected) changes around 20k in all three variables. I believe, this was shortly mentioned, but I do not think it is entirely explained, especially not for the isotopes.

The change, as stated in the manuscript (p.9, l.3) occurs in the control run and results from a sea ice-albedo feedback. The change in CO_2 is less than 1 ppm and less than 0.03 ‰ in $\delta^{13}CO_2$. As the control run is subtracted from all experiments, the effect is visible in the different experiments with different relative importance, depending

on the size of the perturbation. For example, in the case of experiment WEA_{100} with an initial $\delta^{13}CO_2$ perturbation of about -2.5 ‰ (100 GtC with $\delta^{13}C$=-24 ‰), after 20 kyrs only about 1.5 % of the perturbation (-0.038 ‰) are left airborne. This is of the same order of magnitude as the effect of the sea ice-albedo feedback and very small. We added the information of the size of change in the control run to the text which now reads (p.9, l.3):

The jumps visible at around 20 kyrs in Fig. 1 arise from a sea ice-albedo feedback in the control run. They appear most pronounced in the experiments with small perturbations. The change in the control run in CO_2 is less than 1 ppm and less than 0.03 ‰ in $\delta^{13}CO_2$. These jumps are not of further relevance for our discussion.

12. Fig 5: The colorbar on the right hand side is from -30 to +30 ‰ in changes in $\delta^{13}C$. I hope there is a typo and this is wrong by some order of magnitude, otherwise it implies that on the local scale the reconstructions are complete off the target and not useful.

As stated in the figure caption, the colorbar on the right hand side shows the difference between modeled and reconstructed $\delta^{13}C_{DIC}$ using the first three principal components in % of the modeled perturbation and not the difference itself in ‰. We made this clearer in the figure caption by changing the first sentence to read:

Modeled $\delta^{13}C_{DIC}$ perturbation in ‰ (a,c,e,g) and difference between modeled and reconstructed $\delta^{13}C_{DIC}$ perturbation using the first three principal components. These differences are shown in % of the modeled perturbation (b,d,f,h).

Technical issues:

1. Subsection 2.4 Results is empty. Probably this is just the start of section 3 and Discussion is section 4.
Done.

2. Fig 2: Hatched area is "sed + wea" in the legend, but "lithosphere" in the caption. Please combine both somehow (e.g. merge to the same). Does this also include volcanism?
'sed + wea.' was changed to lithosphere' in the legend. Volcanism in the model is a constant flux of $0.08\ GtC\ yr^{-1}$ and part of the weathering input diagnosed after the spin-up. This information is now also included in the methods section (see reply to point 2 above).

3. Fig 3: grey line is called "data", but this is "modeled".
Done.

4. Fig 5: Please add in the caption the time units when describing the subfigures ("1 (c,d)" into "'1000 yr (c,d)" and "10 (e,f)" into "10 kyrs (e,f)" and "50 (g,h) kyrs" into "50 kyrs (g,h)".
Done.

5. page 11, line 1, change "fast" into "faster"
Done.

6. page 12, line 6. "additional addition" is a bit too much adding, delete one.
Done.

7. page 12, line 19, "long-term removal time scale " of what?
Of $\delta^{13}C_{atm}$; added to the text.

8. Throughout: I believe figure should be ordered by when they are refered to, but on page 2 a reference to Fig 5g shows up before any reference to Figs. 2-4.
Done. We removed the reference to Fig. 5 on p12, l20 and changed the order of Fig. 4 and Fig. 5. Further, we modified the caption of Fig. 3 to better conform with the text flow of the main text:

Figure 3: Modeled global-average perturbation of the isotopic signature of dissolved inorganic carbon in the ocean ($\delta^{13}C_{DIC}$; thick gray line) in response to a carbon pulse to the atmosphere of 500 GtC with a $\delta^{13}C$ signature of -24 ‰. The thin colored lines show the perturbation as reconstructed with one (blue), two (green, dash), and three (red) principal components.

9. Appendix: Maybe consider replacing "->" in you subscripts by "2" or "→" (command rightarrow in LaTeX), e.g. in Eq. A17: change $\alpha_{a->b}$ into α_{a2b} or $\alpha_{a\to b}$.
Done.

10. Reference list needs careful revision, since sub- and superscripts seems to be partly wrong, e.g. CO_2 instead of CO_2 etc. Futhermore, AGU paper from the time without page numbers need to have their paper numbers included, e.g. necessary for Parekh et al. (2008) where the missing paper number is PA4202, and the page number 1–14 are useless. This is probably the case for all papers from GBC, GRL, P, and from online only journals such as Nature Communcations which start with page number 1. Check Eggleston et al 2016; Köhler et al 2010; Menviel et al. 2012; Ridgwell and Hargreaves 2007; Skinner et al. 2017; Tarnocai et al 2009 Check also, when two links exist and reduce to one (DOI). Lord et al 2015 is incomplete. Last page number is missing in Wanninkhof 1992.
Done.

References

Bauska, T. K., Baggenstos, D., Brook, E. J., Mix, A. C., Marcott, S. A., Petrenko, V. V., Schaefer, H., Severinghaus, J. P., and Lee, J. E.: Carbon isotopes characterize rapid changes in atmospheric carbon dioxide during the last deglaciation, Proceedings of the National Academy of Sciences, 113, 3465–3470, doi: 10.1073/pnas.1513868113, 2016.

Bauska, T. K., Brook, E. J., Marcott, S. A., Baggenstos, D., Shackleton, S., Severinghaus, J. P., and Petrenko, V. V.: Controls on Millennial-Scale Atmospheric CO_2 Variability During the Last Glacial Period, Geophysical Research Letters, 45, 7731–7740, doi: 10.1029/2018GL077881, 2018.

Colbourn, G., Ridgwell, A., and Lenton, T. M.: The time scale of the silicate weathering negative feedback on atmospheric CO_2, Global Biogeochemical Cycles, 29, 583–596, doi: 10.1002/2014GB005054, 2015.

Eggleston, S., Schmitt, J., Bereiter, B., Schneider, R., and Fischer, H.: Evolution of the stable carbon isotope composition of atmospheric CO_2 over the last glacial cycle, Paleoceanography, 31, 434–452, doi: 10.1002/2015PA002874, 2016.

Lord, N. S., Ridgwell, A., Thorne, M. C., and Lunt, D. J.: An impulse response function for the long tail of excess atmospheric CO_2 in an Earth system model, Global Biogeochemical Cycles, 30, 2–17, doi: 10.1002/2014GB005074, 2016.

Parekh, P., Joos, F., and Müller, S. A.: A modeling assessment of the interplay between aeolian iron fluxes and iron-binding ligands in controlling carbon dioxide fluctuations during Antarctic warm events, Paleoceanography, 23, PA4202, doi: 10.1029/2007PA001 531, 2008.

Schneider, R., Schmitt, J., Köhler, P., Joos, F., and Fischer, H.: A reconstruction of atmospheric carbon dioxide and its stable carbon isotopic composition from the penultimate glacial maximum to the last glacial inception, Climate of the Past, 9, 2507—2523, doi: 10.5194/cp-9-2507-2013, 2013.

Reviewer 2

The authors explore the interactive responses of carbon and carbon isotopes in the land-ocean-atmosphere system to a suite of atmospheric perturbations on timescales spanning from decades to 100,000 years. By considering feedbacks from CaCO3 compensation and weathering as well as short term feedbacks from the land and ocean in an Earth system modeling framework, this study provides an important insight regarding changes in the global carbon cycle on a wide range of timescales. Another novel aspect of this study is that the authors developed and used analytical expressions to better understand the different responses in atmospheric CO2 and the d13C of CO2,simulated from the numerical model. This study is worth being published in Climate of the Past after clarifying the following few points:

We thank the reviewer for the support and thoughtful comments.

1. One of the main finding is that atmospheric CO2 perturbation is relatively gradually removed over a 100,000-year timescale, due to non-negligible effects of carbonate compensation and rock weathering feedbacks on atmospheric CO2. On the other hand, the atmospheric d13C-CO2 perturbation is relatively rapidly removed because the oceanic biological pump and the subsequent burial into sediments play a dominant role in removing atmospheric perturbation (as stated in Abstract). It is interesting to see that the biological pump and the burial into sediments can effectively remove the atmospheric d13C-CO2 perturbation on an e-folding timescale of 6 years (Table 2),while oceanic d13C-DIC is removed on much longer timescales (Figure 2b). What is the mechanisms by which the oceanic d13C-DIC is removed? If the burial of organic carbon from the biological pump is responsible for the long-term removal from the land-ocean-atmosphere system, I feel that the sedimentation model deserves a more detailed description than just pointing to a previous study. I also feel that the results are too briefly discussed in the manuscript. For example, how much organic carbon is buried in time with which d13C signatures?

There appears to be a misunderstanding. The biological pump and sediment burial are not responsible for the initial reduction of the atmospheric perturbations. Rather, air-sea gas exchange and physical ocean transport as well as land biosphere processes are responsible for the initial reduction of the perturbations. We added a corresponding sentence in the abstract and the text reads now (p.1, l.5):

On timescales from years to many centuries the atmospheric perturbations in CO_2 and $\delta^{13}CO_2$ are reduced by

6

air-sea gas exchange and physical transport from the surface to the deep ocean and by the land biosphere. Isotopic perturbations are initially removed much faster from the atmosphere than perturbations in CO_2 as explained by aquatic carbonate chemistry. On longer time scales, the CO_2 perturbation is removed by carbonate compensation and silicate rock weathering. In contrast, the $\delta^{13}C$ perturbation is removed by the relentless flux of organic and calcium carbonate particles buried in sediments.

The fast decrease in IRF($\delta^{13}C$) in the first decade is due to the fast redistribution of the perturbation in the atmosphere-ocean-land system. The main difference to IRF(CO_2) is that the isotopic ratio is not affected by the chemical buffering from the acid-base reactions. The six year timescale from the IRF($\delta^{13}C$) fit is to the time scales of air-sea gas exchange and upper ocean mixing. This is discussed in the manuscript starting on p.9, l.16. We modified the text for the initial response at p.11, l.4 to read:

Further, the top 300 m with a carbon inventory of 2,600 GtC are approximately ventilated within a decade through air-sea gas exchange and upper ocean physical transport processes (circulation, mixing).

On long time scales, the isotopic perturbation in the ocean-atmosphere-land system are indeed jointly removed by the burial flux to the lithosphere. The isotopic perturbation in the ocean, the land biosphere and atmosphere are coupled by air-sea and air-land gas exchange. The burial flux therefore reduces the perturbations in all three reservoirs as evident in Fig. 2b. The sediment module of Bern3D is introduced on p.4, l3-22 in the methods section. The equations, parameters and evaluation of the module have been published earlier. For convenience and further reference, we add a table with all parameters in the appendix. We added the following text on p.4, l.4 to point the interested reader to the details of the model:

The governing equations of the sediment model are given in the appendix A of Tschumi et al. (2011). A comparison of simulated versus observation-based sediment composition for the setup used in this study is given in Appendix B of (Jeltsch-Thömmes et al., 2019). A table with all parameters applied here and by (Jeltsch-Thömmes et al., 2019) is given in the appendix (Table C1).

The following text is added in addition on p.4, l.12 to inform the reader on simulated burial fluxes and sedimentary stocks:

The burial flux at preindustrial steady state is 0.22 GtC yr^{-1} in the form of $CaCO_3$, 0.24 GtC yr^{-1} in the form of POC, and 6.96 TmolSi yr^{-1} in the form of opal, all within the observational range. The global inventories in the interactive sediment layers amount to 916 GtC for $CaCO_3$, to 510 GtC for POC, and to 21,460 Tmol for opal.

Further, we add the equations of the weathering feedback parameterization as documented in (Colbourn et al., 2013) in the appendix.

The marine $\Delta\delta^{13}C_{DIC}$ perturbation is removed by the burial flux of organic carbon and $CaCO_3$. We now add further information about how much organic carbon and $CaCO_3$ is buried over time and with which signature in the section where the carbon and isotopic perturbation budgets are discussed. The new text on p.14, l. 7 reads:

We further illustrate the contribution of the burial and weathering fluxes to the carbon and isotope budgets for the simulation with (WEA_{500}) and without weathering feedbacks (SED_{500}) in Fig. 4. The inventory in the relatively fast exchanging pools – atmosphere, ocean, reactive sediments, land biosphere - increases by 350 GtC in addition to the pulse input of 500 GtC over the course of simulation SED_{500}. This additional increase is mainly due to a reduction in the burial of $CaCO_3$. In contrast, $CaCO_3$ burial is enhanced in simulation WEA_{500} and ~430 Gt of carbon are removed from the fast exchanging reservoirs. This removal is only partly compensated by enhanced weathering (~380 GtC), leading to a reduction in the inventory of the fast exchanging pools from 500 GtC immediately after the pulse to 453 GtC at 100 kyr. Changes in POC burial fluxes are negligible for the carbon budget.

Turning to the isotopic pertubation budget, the initial perturbation due to the pulse input of -12,000 GtC ‰ is mainly removed by anomalies in the POC burial flux both in SED_{500} (~10,000 GtC ‰) and WEA_{500} (~7,000 GtC ‰). Changes in $CaCO_3$ burial and weathering mitigate about a quarter (~2,900 GtC ‰) of the initial isotopic perturbation in the two simulations. This leaves a relatively small isotopic inventory perturbation of +1,100 and -1,600 GtC ‰ in the fast exchanging reservoirs at 100 kyr in simulations SED_{500} and WEA_{500}.

The contributions of the anomalies in the POC and $CaCO_3$ burial fluxes may be approximately attributed to changes in the signature ($\Delta\delta$) and to changes in flux (ΔF) relative to the initial flux, F_0, and signature, δ_0, before the perturbation:

$$\Delta(F \cdot \delta) = F_0 \cdot \Delta\delta + \Delta F \cdot \delta_0 \qquad (1)$$

The isotopic perturbation of the POC burial flux is mainly mediated by a change in the signature of the organic carbon buried ($\Delta\delta^{13}C(POC)$). For example, the signature of the total POC burial flux is on average 0.29 ‰ more negative than the corresponding input from weathering in simulation WEA_{500}. This change in signature of the total POC burial flux leads to an effective reduction of the isotopic perturbation. The change in POC burial flux ($\Delta F(POC)$) is, as mentioned above, negligible. Both changes in the signature of the total $CaCO_3$ burial flux and

changes in CaCO$_3$ burial contribute significantly to the isotopic perturbation. At the end of simulation WEA_{500}, the mean δ^{13}C signature of CaCO$_3$ burial is on average 0.14 ‰ more negative than the input from weathering. In turn, the term $F_0 \cdot \Delta\delta$ for CaCO$_3$ burial contributes $\sim$ -3,100 GtC·‰ to the mitigation of the initial isotopic perturbation. This is partly counteracted by excess burial of CaCO$_3$, with $\Delta F \cdot \delta_0$ equal $\sim$1,300 GtC·‰. This yield an overall burial contribution of $\sim$ -1,800 GtC·‰. The δ^{13}C perturbation is further removed by increased weathering input of CaCO$_3$ (see methods), contributing about 1,100 $GtC \cdot$ ‰ over 100 kyrs in WEA_{500}.

In summary, the isotopic perturbation is mainly mitigated by a change in the signature of the mean POC burial flux. The smaller contributions from the CaCO$_3$ cycle to the isotopic budget is related to both a change in the signature of the mean CaCO$_3$ burial flux and to changes in burial and weathering carbon fluxes.

Further, we add an additional figure (Fig. 2 in the reply) to the revised manuscript, in conjunction with the new text above.
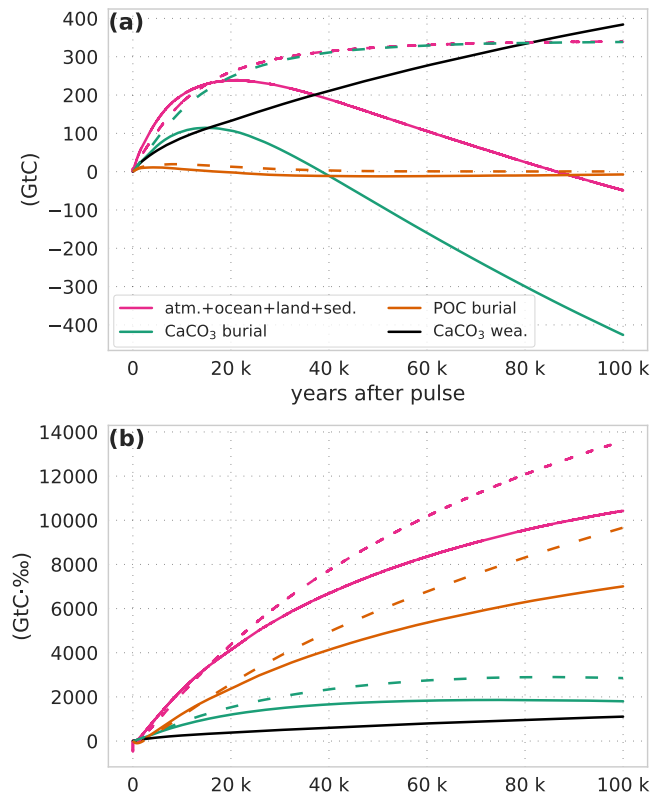

Figure 2: **New Fig. 4 for the revised manuscript:** Budget plot of the anomaly fluxes in (a) GtC and (b) GtC·‰ split up in the atmosphere-ocean-land, atmosphere-ocean-land-reactive sediment, CaCO$_3$ burial, POC burial, and CaCO$_3$ weathering contribution. Solid lines show results from experiment WEA_{500}, dashed lines from experiment SED_{500}.

2. It is also possible that the dissolution and weathering fluxes of CaCO3 and the subsequent mixing with seawater might be responsible for the long-term removal of the d13C-DIC perturbation from the ocean. Furthermore, weathering fluxes to the ocean,with a d13C signature of -9.2 permil (as stated in the introduction, if I understood it correctly), might be important for the oceanic d13C-DIC budget, although this may not be directly important for the atmospheric d13C-CO2. How does the contribution from weathering fluxes to the d13C budget compare with the contribution from the burial fluxes to marine sediments? How does the weathering fluxes in the model change in time and why? It would help if the authors discuss it in more detail. In any case, it is interesting that these slow, yet persistent, carbon burial or weathering fluxes over 100,000 years can remove about 80% of the total d13C perturbation in 100,000 years. A related question is the carbon isotopes budgets for the simulations SED and CLO (i.e., Figure 2 for SED and CLO simulations)?
See also our reply to the point above. Further, we now add a table (Table 1 in the reply) to the revised manuscript that gives the carbon and carbon isotopic budgets at year 100,000 (year 90,000 for experiment CLO_{500}) in GtC and

Table 1: Carbon and carbon isotopic budget at year 100,000 (year 90,000 for exp. CLO_{500}) for atmosphere, land, ocean, sediment, excess organic carbon burial, excess $CaCO_3$ burial, and $CaCO_3$ weathering for the three experiments WEA_{500}, SED_{500}, and CLO_{500}. Values are given in GtC for the carbon and GtC·‰ for the carbon isotopic perturbation.

	exp.	atm.	land	ocean	sediment	excess burial $CaCO_3$	excess burial POC	$CaCO_3$ weathering
	WEA_{500}	11	18	394	30	426	7	384
GtC	SED_{500}	38	71	741	-1	-338	-7	-
	CLO_{500}	73	123	308	-	-	-	-
	WEA_{500}	-98	-662	-1,028	164	-1,801	-7,006	1,106
GtC·‰	SED_{500}	-205	-1,761	3,503	-25	-2,852	-9,664	-
	CLO_{500}	-580	-3,629	-6,343	-	-	-	-

GtC·‰for the contributions from: atmosphere, land, ocean, sediment, lithosphere (split into excess organic carbon burial, excess $CaCO_3$ burial, and excess $CaCO_3$ weathering). The table is shown below and added together with the new text (see point above) on p.13.

3. Another major finding from this study is that the burial flux of d13C is influenced by the spatial (vertical?) d13C gradients. It would be convincing if the authors show the temporal changes in the burial fluxes of d13C along with an index of the spatial d13C gradient for the suite of simulations.
Please see our response to your point 2. We now show the evolution of the burial flux in a new figure. In Fig. 3 below (added to the appendix of the MS), we show the evolution of horizontally-averaged $\delta^{13}C$ of DIC in a Hovmoeller-type diagram and replace '(not shown)' on p.12, l.14 with the reference to the new figure in the appendix.
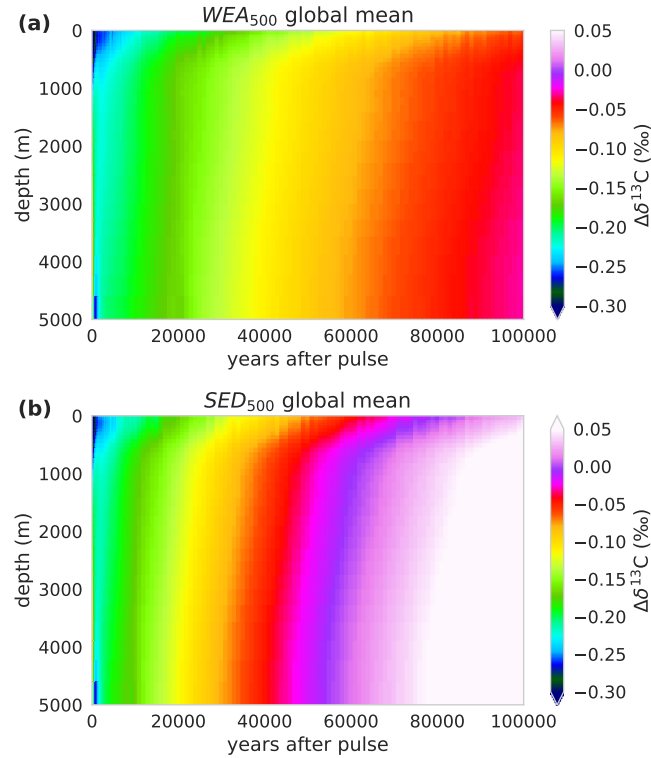

Figure 3: **New Fig. B1 for the revised manuscript:** Hovmoeller-type diagram of global $\Delta\delta^{13}C_{DIC}$ for experiment (a) WEA_{500} and (b) SED_{500}.

4. The analytical expressions for the impulse responses indeed help to better understand the different behavior for CO2 and d13C-CO2, yet require some calcifications.The authors assumed 2 ocean-atmosphere boxes for the equation related to CO2 while assuming 3 ocean-atmosphere-land boxes for the equation related to d13C-CO2. Is it because for CO2 budget the land carbon storage can be neglected? I can follow the derivation except (A1). From

(A1), I can infer that atmospheric carbon concentration is equal to DIC0 at time = 0. I think that a scaling factor might be missing here, as only 1 mol of CO2 is equilibrated with every 200 moles of DIC. The scaling factor might be included in the authors' definition for ha, and would be canceled out eventually, resulting in the same analytical expression as equation (5). Yet it should be clarified. The scaling factor depends on the perturbation P when P is large, hence we would end up arriving at an equation (5) that depends on P when P is large, which might be a reason that we see a different response for the p5000 simulation in Figure 1a (?).

We add the following sentences from the appendix to the main text to justify our choice of a 2-box model for the CO_2 and a 3-box model for the $\delta^{13}C$ perturbation. The text on p.10, l.6 now reads:

Changes in land biosphere carbon storage can be considerable, in particular during the first century (see Fig. 3a). However, the role of the land carbon stock changes becomes smaller, the more carbon is taken up by the ocean and is thus for simplicity not considered in the analytical expression for CO_2. For CO_2 the expression reads: [...]

In case of the isotopic perturbation, we add on p.10, l.15:

For $\delta^{13}C_a$, we also consider the initial carbon inventory of the land biosphere ($N_{b,0}$), as a substantial amount of the isotopic perturbation is contained in the land biosphere on multi-centennial to millennial timescales (Fig. 3b). The corresponding expression reads (for the derivation see the appendix):

There is no scaling factor missing in the equations and equation A7 does not explicitly depend on the size of the pulse. The concentration C is specifically defined for our box model and should not be confused with the concentration or mixing ratio of CO_2 in the real-world atmosphere. We note now that the Revelle factor depends on the pulse size. We have clarified the text starting on p22, l5 to read:

We consider a two box model of the atmosphere (index: a) and ocean (index: o) with area $A=A_a=A_o$ and heights h_a and h_o. All boxes are assumed to be well mixed. Before the pulse addition, the model is in equilibrium and the initial CO_2 partial pressure is $pCO_{2,0}=pCO_{2,a,0}=pCO_{2,o,0}$. The initial concentration of dissolved inorganic carbon (DIC) in the ocean is DIC_0 and the carbon inventory in the ocean is given by $N_o=DIC \cdot h_o \cdot A$. We relate the atmospheric carbon inventory, N_a, to a time-varying atmospheric concentration C_a and to the fixed volume of the model atmosphere: $N_a=C_a \cdot h_a \cdot A$. We are free to select the units of the model-specific concentration C_a. Here, we express C_a in units of DIC_0 and set the initial atmospheric concentration $C_{a,0}$ equal to DIC_0. The atmospheric inventory is proportional to the atmospheric partial pressure, $pCO_{2,a}$ and, correspondingly, C_a has to be proportional to $pCO_{2,a}$. This leads to the following definition of C_a:

$$C_a = \frac{pCO_{2,a}}{pCO_{2,0}}DIC_0, \tag{2}$$

C is specifically defined for our box model and should not be confused with the concentration or mixing ratio of CO_2 in the real-world atmosphere. The atmospheric scale height h_a is given by the requirement that volume times concentration equals inventory:

$$h_a = \frac{N_{a,0}}{A \cdot DIC_0}. \tag{3}$$

The perturbation (Δ) from the initial equilibrium in pCO_2, and similarly for other quantities, is defined by: $\Delta pCO_2(t)= pCO_2(t)-pCO_2(t_0)$. The perturbation in $pCO_{2,o}$ is related to that in DIC by the Revelle factor ξ (Revelle and Suess, 1957):

$$\xi = \frac{\Delta pCO_{2,o}}{pCO_{2,0}} \cdot \frac{DIC_0}{\Delta DIC} \tag{4}$$

We note that the carbonate chemistry is non-linear and ξ varies with environmental conditions (DIC, alkalinity, temperature, salinity). Assuming a constant Revelle factor ξ is therefore an approximation. In particular, ξ increases with increasing DIC. As a consequence, the "effective" value of ξ increases with increasing carbon emission and is thus the larger the larger the magnitude of the carbon pulses. [This yields for the perturbation in the net air-to-sea carbon flux...]

Equation 5 implicitly includes a dependence on the pulse size in form of the buffer factor ξ. The larger the pulse size the larger also the buffer factor and thus also the remaining atmospheric fraction. We state this in the appendix on p.27, l.17-18 and now also include it in the main text on p.11, l.6:

It has to be noted here that we assume ξ constant for small perturbations. With increasing pulse sizes, also ξ increases, leaving larger airborne fractions (c.f. WEA_{500} versus WEA_{5000} in Fig. 1a after 1-2 kyrs). Regarding $\delta^{13}C$, the corresponding [...]

Short Comment by James Menking

Hi Aurich and Fortunat, Great paper! In my opinion, this is already well-written and clearly presented. The work is relevant to anyone interested in the carbon cycle, especially to those of us interested in d13C.

I'm curious about two things:

(1) One conclusion of the paper is that you cannot get a 0.2 ‰ depletion in atmospheric d13C-CO2 and a 10 ppm rise in CO2 concentration from a terrestrial pulse, as is suggested by Bauska 2018 as a possible cause of the variations observed at the onset of HS4. Your conclusion is based on your Figure 6, which shows that terrestrial pulses of carbon reduce d13C-CO2 only ~0.1 ‰ per 10 ppm increase in CO2. But you state in the caption that the results in Figure 6 are the means of the model output for the 30 years immediately following the perturbations. So the atmospheric data during the perturbations (i.e. while CO2 is increasing and d13C-CO2 decreasing) are not considered? In my own modeling experiments with the OSU 14-box model (model described in Bauska 2016), fitting d13C-CO2 v. CO2 output during a land carbon pulse, not just the recovery after it, significantly decreases the slope in the Keeling plot and makes a -0.2 ‰ change in d13C-CO2 per 10 ppm increase in CO2 due to land carbon seem more feasible. Do you think that the perturbations themselves are too fast to be recorded in ice cores? Surely this is true for extremely fast pulses, but the results in Figure 6 include perturbations up to 400 years duration, which I think should be captured by ice cores even with relatively large gas age distributions. Put another way, I observe that land carbon pulses in our box model plot as quasi-ellipses in a Keeling plot with the slope of the d13C-CO2 v. CO2 being more negative on the way "up" versus on the way "down," even for multi-centennial carbon releases. So I guess the question is - to what extent is the "up" variability recorded in ice cores? - because it may argue for the Bauska 2018 interpretation. The conclusion in your paper seems particularly strong without elaborating more on this point.

Thank you for raising this issue. Averaging over different intervals and also including the 'up' variability smears out the rather straight line seen in Fig. 6 to something more like a cone, opening at higher ΔCO_2 values, and also moving $\Delta\delta^{13}C$-ΔCO_2 pairs towards the ice core value. We provide now more background information, add a second panel to Fig. 6 of the manuscript (Fig. 4 below, Fig. 7 in the revised manuscript) and change the corresponding paragraphs starting on p.20, l.29 to now read:
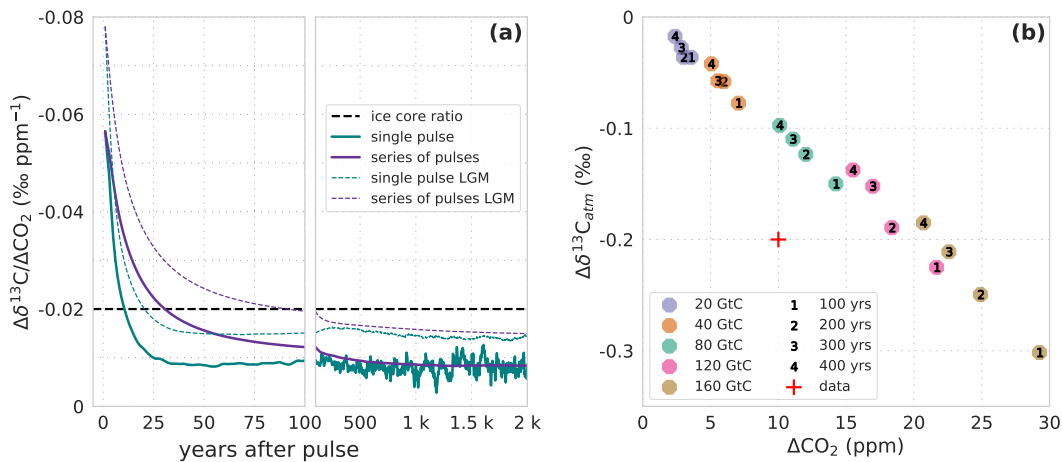

Figure 4: **New Fig. 7 for the revised manuscript:** (a) First 2 kyrs of the $\Delta\delta^{13}C$ to ΔCO_2 ratio of a 100 GtC pulse (WEA_{100}, LGM_{100}) plotted over time of single pulses (teal crosses) and series of pulses up to the "year after pulse" where plotted (purple crosses). Dashed horizontal line indicates a $\Delta\delta^{13}C$ to ΔCO_2 ratio of 10 ppm to -0.2 ‰ as seen in ice core records for HS1 and HS4. (b) Response in ΔCO_2 and $\Delta\delta^{13}C_{atm}$ to a uniform release of 20, 40, 80, 120, and 160 GtC (colors) of isotopically light carbon ($\delta^{13}C$ = -24 ‰) to the atmosphere over 100, 200, 300, and 400 years (numbers). Shown is the mean over 30 years starting in the last year of the release. Red cross indicates the approx. $\Delta\delta^{13}C$ to ΔCO_2 change as seen in ice core records for HS1 and HS4 (Bauska et al., 2016, 2018).

Further, the different behavior of CO2 and $\delta^{13}C_{atm}$ perturbations has also consequences for centennial scale CO2 and $\delta^{13}C_{atm}$ variations such as during Heinrich Stadial (HS) 4 and 1. Variations in CO2 and $\delta^{13}C_{atm}$ during HS4 and HS1 have been measured on Antarctic ice cores. The data show an increase in CO2 on the order of ~10 ppm over 200-300 years, accompanied by a decrease in $\delta^{13}C_{atm}$ of ~0.2 ‰. This results in a value of roughly -0.02 ‰ per ppm for the ratio of the change in $\delta^{13}C$ to the change in CO2 ($r= \Delta\delta^{13}C / \Delta CO_2$). These changes have been attributed to a release of terrestrial carbon to the atmosphere (Bauska et al., 2016, 2018).

We utilize our pulse response simulations under PI and LGM boundary conditions to estimate the changes in r in response to a transient terrestrial carbon input with an isotopic signature of -24 ‰. The results for r will depend on the evolution of the emissions into the atmosphere. For a pulse-like input at time zero the evolution of r after the pulse is shown in Fig. 4 for the first 2,000 years. r is about -0.08 (-0.06) ‰ ppm^{-1} immediately after the release under LGM (PI) boundary conditions. The difference between LGM and PI values of r comes from the difference in the atmospheric C and ^{13}C inventory to which the pulse is added. The magnitude of r is reduced rapidly within the first 25 years and remains approximately constant at -0.015 (-0.01) ‰ ppm^{-1} thereafter. Thus, r recorded in ice after a hypothetical pulse release of carbon would be closer to -0.01 than -0.02 ‰ ppm^{-1} if the age distribution of the ice core samples is wider than a few decades. However, emissions may occur more gradually. For simplicity, we assume an emission pulse sustained over period T according to a two-sided Heaviside function; terrestrial emissions, $e(t)$, suddenly increase to unity, remain elevated for period T, and are then immediately reduced again to zero. r is then readily calculated from the IRFs ($r = \int_0^T dt \cdot e(t) \cdot \text{IRF}(\delta^{13}\text{C})(T - t)/\int_0^T dt \cdot e(t) \cdot \text{IRF}(\text{CO}_2)(T - t)$). The results for r are again plotted in Fig. 4. r is decreasing with the duration T of sustained emissions and falls below -0.02 ‰ ppm^{-1} for T larger than about 90 (30) years for LGM (PI) boundary conditions. Finally, we also performed simulations with the Bern3D-LPX under PI boundary conditions to account for non-linearity that may not be captured in the IRF representation. The releases of varying amounts of terrestrial carbon with $\delta^{13}\text{C}$ = -24 ‰ over 100 to 400 years yield a linear response in ΔCO_2 and $\Delta\delta^{13}\text{C}_{atm}$ (Fig. 4) with a slope r of about -0.01 ‰ ppm^{-1}.

There are uncertainties in these estimates of r. We assumed that the emitted carbon was about -18 ‰ depleted with respect to the atmosphere. The relative uncertainty in this value translates directly to the relative uncertainty in r. The release of material that is isotopically even more depleted would bring our model results in better agreement with the ice core estimate of r. Observations and land model simulations suggest that the $\delta^{13}\text{C}$ depletion in vegetation and soils may vary between -24 ‰, for heavily discriminated C3 plant material, to -5 indicative of C4 plant material Keller et al. (2018). C4 plants were likely more abundant during glacials than interglacials (Collatz et al., 1998). Also, the values shown in Fig. 4 are 30-year means. A wider gas age distribution would reduce the perturbation in $\delta^{13}\text{C}_{atm}$ more than in CO$_2$ (see e.g. Köhler et al., 2011). On the other hand, the increase in While there are uncertainties in our model estimates as well as in the determination of r from the ice core measurements, our analysis suggests that other mechanisms in addition to a terrestrial release appear to have contributed to the CO$_2$ and $\delta^{13}\text{C}_{atm}$ excursions during HS4 and HS1.

We acknowledge that most of the idealized simulations presented in this study were run under preindustrial boundary conditions. A limited set of sensitivity simulations suggest that the IRFs for CO$_2$ and $\delta^{13}\text{C}$ are similar under preindustrial and glacial CO$_2$ in our model. The direct influence of lower atmospheric CO$_2$ on IRF(δ^{13}C) appears limited. Further work is needed to better quantify the dependency of IRFs on the climate state.

We also adjusted the wording in the abstract to better reflect these uncertainties:
Our results may suggest that changes in terrestrial carbon storage were not the sole cause for the abrupt, centennial CO$_2$ and δ^{13}C variations recorded in ice during Heinrich Stadials HS1 and HS4 of the last glacial period. However, model and data uncertainties prevent a firm conclusion.

(2) Another conclusion in the paper is that the PGM-LGM d13C-CO2 difference observed in the Schneider/ Schmitt/ Eggleston work cannot be due to changes in terrestrial carbon storage, or internal reorganizations in the marine carbon cycle without considering burial. But I had a difficult time understanding how the results of your experiments argue for these points. Regarding terrestrial carbon storage, is your point that the PGM-LGM land carbon difference would have been too large because the atmospheric imprint of any smaller land carbon transfer would have been attenuated too much to cause the observed PGM-LGM d13C-CO2 difference? If so, the connection between the model results and the stated conclusion could be clearer. I thought it was also difficult to follow your point about the marine carbon cycle. Perhaps showing the marine and atmospheric d13C data for the PGM v. LGM would help, and stating more clearly exactly how your experimental results support the conclusions.

In light of your comments we modified the text for clarification. The paragraph (p.20, l. 9) reads now:
Our results have consequences for the interpretation of the difference in δ^{13}C between similar climate states such as the Penultimate Glacial Maximum (PGM) and the Last Glacial Maximum (LGM). Substantial temporal δ^{13}C differences between these periods are recorded in ice cores (Schneider et al., 2013; Eggleston et al., 2016) and in marine sediments (Hoogakker et al., 2006; Oliver et al., 2010). Different mechanisms, such as changes in the δ^{13}C signature of weathering and burial fluxes, varying contribution of volcanic outgassing of CO$_2$, and changes in the amount of carbon stored in the land biosphere, especially in yedoma and permafrost soils, have been discussed for the PGM-LGM δ^{13}C offset (e.g. Lourantou et al., 2010; Schneider et al., 2013). An internal reorganization

of the marine carbon cycle without considering changes in burial may not explain the offset. With no changes in the weathering-burial balance, the mass in the atmosphere-ocean-land system remains constant. Then, a change in atmospheric δ^{13}C would require an opposing δ^{13}C change in the ocean. This appears in conflict with marine and ice core records which suggest that δ^{13}C increased both in the ocean and in atmosphere by about 0.3 ‰ between the PGM and LGM (Hoogakker et al., 2006; Oliver et al., 2010; Schneider et al., 2013; Eggleston et al., 2016). However, internal marine carbon cycle reorganizations, e.g., due to changes in circulation, may have altered δ^{13}C in the surface ocean, and in turn δ^{13}C of the burial flux, and thereby the balance between weathering input and burial.

The Bern3D results suggest that changes in organic carbon storage on land (or in the ocean) are not a likely explanation of the isotopic offset. The δ^{13}C signal of a transfer of organic carbon of plausible magnitude to the atmosphere and ocean would have been attenuated too much over time to cause the observed PGM-LGM δ^{13}C difference. Schneider et al. (2013) estimated required changes in land carbon storage to match the ice core and marine temporal offsets in δ^{13}C using preliminary Bern3D results for pulse release simulations. Our results show, in agreement with these earlier results, that the isotopic perturbation associated with a terrestrial carbon release is attenuated to less than 15 % within two millennia for pulse sizes of up to 5,000 GtC and declines thereafter (see black line in Fig. 5b). This would require several thousand GtC to have been stored additionally in the land biosphere during the LGM compared to the PGM in order to explain the δ^{13}C offset (see also Schneider et al., 2013). This amount seems large in light of estimated total carbon stocks of ~1500 GtC in perennially frozen soils in Northern Hemisphere permafrost regions today (Tarnocai et al., 2009) and an even smaller inventory at the LGM (Lindgren et al., 2018).

Taken together, these ad-hoc considerations suggest that long-term imbalances in the weathering (including volcanic emissions) and burial fluxes appear to be a plausible cause for the δ^{13}C differences between PGM and LGM. However, further work, which considers the transient evolution of CO_2, δ^{13}C and other proxies, is required to gain further insight into the contributions of individual mechanisms to long term δ^{13}C changes recorded in ice and marine cores.

I'm very keen to hear your thoughts. Thanks, and good luck with the rest of the submission! - Andy Menking

References

Bauska, T. K., Baggenstos, D., Brook, E. J., Mix, A. C., Marcott, S. A., Petrenko, V. V., Schaefer, H., Severinghaus, J. P., and Lee, J. E. (2016). Carbon isotopes characterize rapid changes in atmospheric carbon dioxide during the last deglaciation. *Proceedings of the National Academy of Sciences*, 113(13):3465–3470.

Bauska, T. K., Brook, E. J., Marcott, S. A., Baggenstos, D., Shackleton, S., Severinghaus, J. P., and Petrenko, V. V. (2018). Controls on Millennial-Scale Atmospheric CO2 Variability During the Last Glacial Period. *Geophysical Research Letters*, 45(15):7731–7740.

Colbourn, G., Ridgwell, A., and Lenton, T. M. (2013). The Rock Geochemical Model (RokGeM) v0.9. *Geoscientific Model Development*, 6(5):1543–1573.

Colbourn, G., Ridgwell, A., and Lenton, T. M. (2015). The time scale of the silicate weathering negative feedback on atmospheric CO2. *Global Biogeochemical Cycles*, 29(5):583–596.

Collatz, G. J., Berry, J. A., and Clark, J. S. (1998). Effects of climate and atmospheric CO 2 partial pressure on the global distribution of C 4 grasses: present, past, and future. *Oecologia*, 114(4):441–454.

Eggleston, S., Schmitt, J., Bereiter, B., Schneider, R., and Fischer, H. (2016). Evolution of the stable carbon isotope composition of atmospheric CO2 over the last glacial cycle. *Paleoceanography*, 31(3):434–452.

Hoogakker, B. A., Rohling, E. J., Palmer, M. R., Tyrrell, T., and Rothwell, R. G. (2006). Underlying causes for long-term global ocean δ13C fluctuations over the last 1.20 Myr. *Earth and Planetary Science Letters*, 248(1-2):15–29.

Jeltsch-Thömmes, A., Battaglia, G., Cartapanis, O., Jaccard, S. L., and Joos, F. (2019). Low terrestrial carbon storage at the Last Glacial Maximum: constraints from multi-proxy data. *Climate of the Past*, 15(2):849–879.

Joos, F. and Bruno, M. (1998). Long-term variability of the terrestrial and oceanic carbon sinks and the budgets of the carbon isotopes 13 C and 14 C. *Global Biogeochemical Cycles*, 12(2):277–295.

Keller, D. P., Lenton, A., Scott, V., Vaughan, N. E., Bauer, N., Ji, D., Jones, C. D., Kravitz, B., Muri, H., and Zickfeld, K. (2018). The Carbon Dioxide Removal Model Intercomparison Project (CDRMIP): Rationale and experimental protocol for CMIP6. *Geoscientific Model Development*, 11(3):1133–1160.

Köhler, P., Knorr, G., Buiron, D., Lourantou, A., and Chappellaz, J. (2011). Abrupt rise in atmospheric CO2 at the onset of the Bølling/Allerød: in-situ ice core data versus true atmospheric signals. *Climate of the Past*, 7(2):473–486.

Lindgren, A., Hugelius, G., and Kuhry, P. (2018). Extensive loss of past permafrost carbon but a net accumulation into present-day soils. *Nature*, 560(7717):219–222.

Lord, N. S., Ridgwell, A., Thorne, M. C., and Lunt, D. J. (2016). An impulse response function for the âlong tailâ of excess atmospheric CO2 in an Earth system model. *Global Biogeochemical Cycles*, 30(1):2–17.

Lourantou, A., Chappellaz, J., Barnola, J. M., Masson-Delmotte, V., and Raynaud, D. (2010). Changes in atmospheric CO2 and its carbon isotopic ratio during the penultimate deglaciation. *Quaternary Science Reviews*, 29(17-18):1983–1992.

Oliver, K. I. C., Hoogakker, B. A. A., Crowhurst, S., Henderson, G. M., Rickaby, R. E. M., Edwards, N. R., and Elderfield, H. (2010). A synthesis of marine sediment core d13C data over the last 150 000 years. *Climate of the Past*, 6(5):645–673.

Peltier, W. R. (1994). Ice Age Paleotopography. *Science*, 265(5169):195 – 201.

Revelle, R. and Suess, H. E. (1957). Carbon Dioxide Exchange Between Atmosphere and Ocean and the Question of an Increase of Atmospheric CO2 during the Past Decades. *Tellus*, 9(1):18–27.

Schneider, R., Schmitt, J., Köhler, P., Joos, F., and Fischer, H. (2013). A reconstruction of atmospheric carbon dioxide and its stable carbon isotopic composition from the penultimate glacial maximum to the last glacial inception. *Climate of the Past*, 9(6):2507–2523.

Siegenthaler, U. and Oeschger, H. (1987). Biospheric CO2 emissions during the past 200 years reconstructed by deconvolution of ice core data. *Tellus B: Chemical and Physical Meteorology*, 39(1-2):140–154.

Tarnocai, C., Canadell, J. G., Schuur, E. A. G., Kuhry, P., Mazhitova, G., and Zimov, S. (2009). Soil organic carbon pools in the northern circumpolar permafrost region. *Global Biogeochemical Cycles*, 23(2):GB2023.

Tschumi, T., Joos, F., Gehlen, M., and Heinze, C. (2011). Deep ocean ventilation, carbon isotopes, marine sedimentation and the deglacial CO2 rise. *Climate of the Past*, 7(3):771–800.
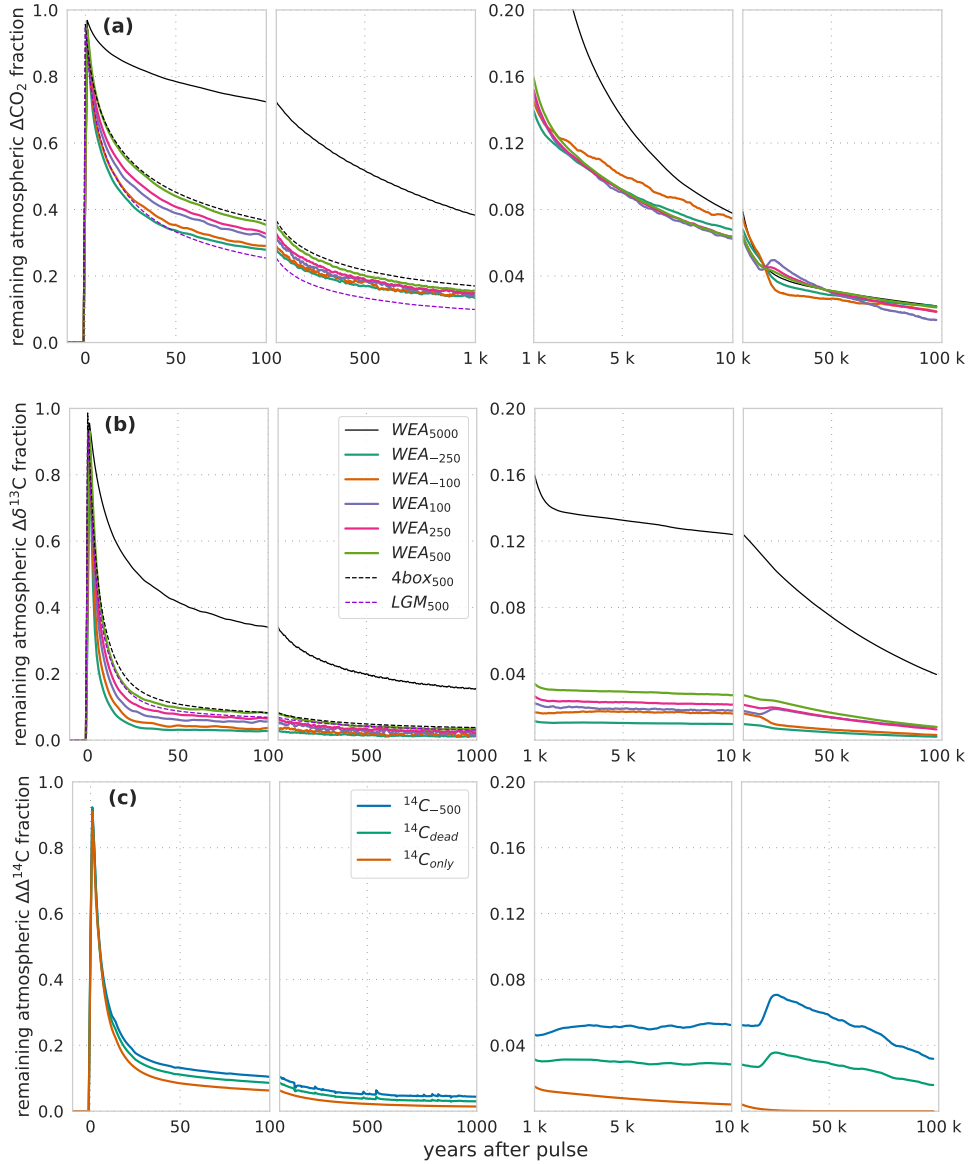
Figure 5: **New Fig. 1 for the revised manuscript:** (a) CO_2,(b) $\delta^{13}C$, and (c) $\Delta^{14}C$ perturbation in the atmosphere for different simulations with different pulse sizes and model configurations. The isotopic signature is $\delta^{13}C$=-24 ‰ for all pulse sizes except the 5000 GtC pulse with $\delta^{13}C$=-28 ‰. Dashed and dotted brown lines in panel (a) and (b) show results from a 500 GtC pulse with no weathering feedback and no ocean sediments, respectively. See Table 1 and section 2.2 for details of the experimental setup of the runs. Note that the scaling of the second y-axis is different for the three panels. Data are filtered with a moving average of 1000 years in the interval 1 kyr - 10 kyrs and 5000 years in the interval 10 kyr - 100 kyrs for better visibility. Factorial simulations (WEA_{500}, SED_{500}, CLO_{500}, $4box_{500}$, and LGM_{500}) for the time interval 1 kyr to 100 kyrs are shown in Fig. 6 for better visibility.

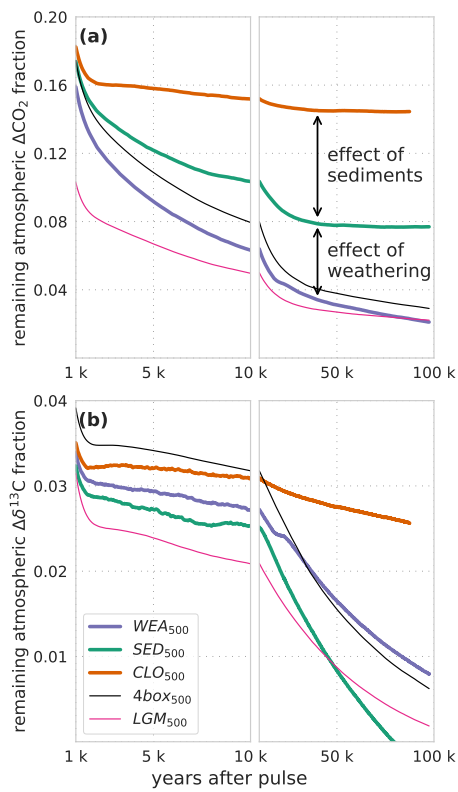Figure 6: **New Fig. 2 for the revised manuscript:** (a) CO_2 and (b) $\delta^{13}C$ perturbation in the atmosphere for the factorial simulations WEA_{500}, SED_{500}, CLO_{500}, $4box_{500}$, and LGM_{500}. Shown is the time interval 1 kyr to 100 kyrs Data are filtered with a moving average of 1000 years in the interval 1 kyr - 10 kyrs and 5000 years in the interval 10 kyr - 100 kyrs for better visibility. Note that experiment CLO_{500} was run for 90 instead of 100 kyrs.

The response to pulse-like perturbations in atmospheric carbon and carbon isotopes

Aurich Jeltsch-Thömmes and Fortunat Joos

Climate and Environmental Physics, Physics Institute and Oeschger Centre for Climate Change Research, University of Bern, Bern, Switzerland

Correspondence: Aurich Jeltsch-Thömmes (aurich.jeltsch-thoemmes@climate.unibe.ch)

Abstract. Measurements of carbon isotope variations in climate archives and isotope-enabled climate modelling foster the understanding of the carbon cycle. Perturbations in atmospheric CO_2, and in its isotopic ratios ($\delta^{13}C$, $\Delta^{14}C$) are removed on different time scales and by partly different processes. We investigate these differences on timescales of up to 100,000 years in idealized pulse release experiments with the Bern3D-LPX Earth system model of intermediate complexity and by analytical solutions from a box model. On timescales from years to many centuries the atmospheric perturbations in CO_2 and $\delta^{13}CO_2$ are reduced by air-sea gas exchange and physical transport from the surface to the deep ocean and by the land biosphere. Isotopic perturbations are initially removed much faster from the atmosphere than perturbations in CO_2 as explained by aquatic carbonate chemistry. On longer time scales, the CO_2 perturbation is removed by carbonate compensation and silicate rock weathering. In contrast, the $\delta^{13}C$ perturbation is removed by the relentless flux of organic and calcium carbonate particles buried in sediments. The associated removal rate is significantly modified by spatial $\delta^{13}C$ gradients within the ocean influencing the isotopic perturbation of the burial flux. Space-time variations in ocean $\delta^{13}C$ perturbations are captured by three Principal Components and Empirical Orthogonal Functions. Analytical impulse response functions for atmospheric CO_2 and $\delta^{13}CO_2$ are provided. Our results ~~show~~ may suggest that changes in terrestrial carbon storage ~~are unlikely~~ were not the sole cause for the abrupt, centennial CO_2 and $\delta^{13}C$ variations recorded in ice during Heinrich Stadials HS1 and HS4 of the last glacial period. ~~Ocean processes likely played a significant role~~ However, model and data uncertainties prevent a firm conclusion. The $\delta^{13}C$ offset between the penultimate and last glacial maximum reconstructed for the ocean and atmosphere is most likely caused by imbalances between weathering, volcanism and burial fluxes.

1 Introduction

Research efforts to understand the past and future evolution of atmospheric CO_2 and of its isotopic signature are ongoing since many decades. Yet, many open questions still remain~~, such as the mechanisms governing glacial-interglacial CO_2 variations over the past 800 thousand years recorded in ice cores (e.g. Neftel et al., 1982; Siegenthaler et al., 2005; Lüthi et al., 2008; Marcott et al., 20~~ ~~. Or more specifically~~. Specifically, to the offsets in the stable isotope signature of CO_2 ($\delta^{13}C_{atm}$) and of dissolved inorganic carbon ($\delta^{13}C_{DIC}$) between the Penultimate (PGM) and Last Glacial Maximum (LGM) and between the two recent interglacials, the Eem and and the Holocene (Schneider et al., 2013; Eggleston et al., 2016; Hoogakker et al., 2006; Oliver et al., 2010). Could

this PGM-LGM δ^{13}C offset result from a change in terrestrial carbon storage, or rather from changes in carbon and carbon isotope fluxes connected to the sedimentary weathering-burial cycle? Further questions remain regarding CO_2 and $\delta^{13}C_{atm}$ variations on centennial and millennial timescales and a possible role of changes in the land biosphere carbon inventory (e.g. Köhler et al., 2010; Skinner et al., 2010; Schmitt et al., 2012; Skinner et al., 2017; Bauska et al., 2018). Reconstructed varia-

5   tions in CO_2 and $\delta^{13}C_{atm}$ during Heinrich Stadial (HS) 4 and 1, two northern hemisphere cold periods during the last glacial, have been attributed to changes in terrestrial carbon storage (e.g. Bauska et al., 2016, 2018).

The perturbations in CO_2 and $\delta^{13}CO_2$ due to a carbon input (or removal) from the land biosphere or from fossil fuel burning are removed by a few principal processes. In the case of CO_2, over the first decades and centuries, it is ocean invasion and land uptake, on millennial timescales $CaCO_3$ compensation, and finally, on timescales of hundreds of thousands of years the remain-

10   ing atmospheric CO_2 perturbation is removed by enhanced silicate rock weathering ~~(e.g. Archer et al., 1998; Joos et al., 2001, 2013; Colbou~~ (e.g. Archer et al., 1998; Joos et al., 2001, 2013; Colbourn et al., 2015; Lord et al., 2016). In the case of δ^{13}C, the perturbation is mixed rather quickly throughout the atmosphere-land-ocean reservoir and is removed on multi-millennial timescales by changes in the isotopic signature of weathering and burial fluxes.

Simulations of climate and CO_2 over thousands of years with dynamic, 3-dimensional models remain still challenging. Over

15   the last decades, computational power has continuously increased and first results from simulations with Earth System Models of Intermediate Complexity (EMICs) covering glacial-interglacial cycles have been published (e.g. Brovkin et al., 2012; Menviel et al., 2012; Ganopolski and Brovkin, 2017). However, to date these long timescales prevented large ensemble simulations with spatially resolved models as well as glacial-interglacial simulations using state-of-the-art Earth System Models. A possible tool to overcome these computational obstacles is the use of reduced form models invoking Impulse Response

20   Functions (IRFs) and Principal Component - Empirical Orthogonal Function (PC-EOF) analysis. IRFs and PC-EOF analysis are instrumental to characterize the fundamental time and spatial scales of model response to a perturbation.

The response of a linear system to a perturbation such as carbon emissions to the atmosphere can be fully characterized by its IRF. The atmosphere-ocean CO_2 cycle can be approximated as a nearly linear system, as long as concentrations do not vary much, i.e. less than a doubling of pre-industrial CO_2 concentrations (Hooss et al., 2001). The perturbation in the atmosphere or

25   ocean is then given by the convolution integral of the emission history and the corresponding IRF (e.g. Joos and Bruno, 1996; Joos et al., 1996). IRFs can easily be described by a sum of exponentials, yielding a cost efficient substitute model for describing the temporal evolution of an atmospheric CO_2 perturbation. IRFs have been widely used to calculate remaining atmospheric fractions of anthropogenic CO_2 emissions on different timescales and to characterize model behaviour and their characteristic response time scales ~~(e.g. Siegenthaler and Oeschger, 1978; Maier-Reimer and Hasselmann, 1987; Sarmiento et al., 1992; Siegenthaler an~~

30   (e.g. Siegenthaler and Oeschger, 1978; Maier-Reimer and Hasselmann, 1987; Sarmiento et al., 1992; Siegenthaler and Joos, 1992; Enting . However, peer-reviewed studies that quantify the IRF for carbon isotopes of CO_2 are scarce (Schimel et al., 1996; Joos and Bruno, 1996) and, to our knowledge, not available for multi-millennial time scales.

Principal Component analysis is widely used to capture the information of multi-dimensional data. The atmospheric perturbation in CO_2 and its isotopes in response to carbon input external to the ocean-atmosphere system is propagated to the ocean.

35   The resulting spatio-temporal (4-D) evolution of marine tracers may be conveniently approximated using PC-EOF analysis.

The perturbation is described as a superposition of spatial empirical orthogonal functions (EOF(x)) multiplied with the corresponding time dependent principal component (PC(t)). Combining IRF and PC-EOF then allows to compute the perturbation in space and time with minimal computational resources (Hooss et al., 2001; Joos et al., 2001)

The main goal of this study is to investigate the time scales and underlying processes for the removal of an atmospheric perturbation in CO_2 and its $\delta^{13}C$ signature in response to an external carbon input. To this end, we performed pulse-release (uptake) experiments over 100,000 years with the Bern3D-LPX EMIC. We determine characteristic Impulse Response (or Green's) Functions (IRF) and describe marine spatio-temporal variations using PC-EOF analysis. Responses in atmospheric radiocarbon signature ($\Delta^{14}C$) are briefly addressed. Implications of our results for the PGM-LGM $\delta^{13}C$ difference and for past centennial CO_2 variations are discussed. Simple expressions that illuminate the fundamental differences in the removal time scales for an atmospheric perturbation in CO_2 versus the associated perturbation in $\delta^{13}CO_2$ are developed in the Appendix. The pulse experiments are thought to represent (i) the sudden carbon uptake from or release to the atmosphere by the land biosphere, (ii) the release of old organic carbon, e.g., from ancient peat or permafrost material, (iii) the burning of all conventional fossil fuel resources, and (iv) a variation in ^{14}C production by cosmic radiation or atomic bomb tests.

2 Model and experimental set-up

2.1 The Bern3D-LPX model

For this study, the Bern3D v2.0s Earth System Model of Intermediate Complexity (EMIC) is used coupled to the dynamic vegetation model LPX-Bern v1.4. The Bern3D consists of a three dimensional geostrophic ocean (Edwards et al., 1998; Müller et al., 2006) with an isopycnal diffusion scheme and Gent-Mc Williams parameterization for eddy-induced transport (Griffies, 1998), a single layer energy-moisture balance atmosphere to which a thermodynamic sea-ice component is coupled (Ritz et al., 2011). We use the ocean model coupled to a 10 layer sediment module (Tschumi et al., 2011; Heinze et al., 1999) with updated sediment parameters (Jeltsch-Thömmes et al., 2019) and to a global representation of rock weathering (Colbourn et al., 2013). The resolution of the Bern3D model components is 41x40 horizontal grid cells with 32 logarithmically spaced depth layers in the ocean. Wind stress at the ocean surface is prescribed from the NCEP/NCAR monthly wind stress climatology (Kalnay et al., 1996) and air-sea gas exchange and carbonate chemistry follow OCMIP-2 protocols (Najjar and Orr, 1999; Orr et al., 1999; Wanninkhof, 2014; Orr and Epitalon, 2015; Orr et al., 2017). The global mean air-sea gas transfer rate is reduced by 19 % to match observational radiocarbon estimates (Müller et al., 2006) and gas transfer velocity scales linearly with wind speed (Krakauer et al., 2006).

Marine productivity is calculated as a function of light availability, temperature, and nutrient concentrations (P, Fe, Si), and is restricted to the euphotic zone in the uppermost 75 m. Tracers, including dissolved inorganic carbon and semi-labile organic carbon (DIC, DOC), the corresponding isotopic forms, as well as alkalinity (Alk), phosphate (PO_4), oxygen (O_2), iron (Fe), silica (Si), and an ideal age tracer, are transported by advection, diffusion, and convection. Biogeochemical cycling is described in detail in Tschumi et al. (2011) and Parekh et al. (2008) and subsequent studies (e.g. Menviel and Joos, 2012; Menviel et al., 2012; Roth and Joos, 2012; Roth et al., 2014; Menviel et al., 2015; Battaglia et al., 2016; Battaglia and Joos,

2018a, b; Jeltsch-Thömmes et al., 2019). Isotopic fractionation between model components is documented in Jeltsch-Thömmes et al. (2019).

The sediment module dynamically calculates the transport, redissolution/remineralization, and bioturbation of solid material, the pore water chemistry, and diffusion in the top 10 cm of the sediment. The governing equations of the sediment model are given in the appendix A of Tschumi et al. (2011). A comparison of simulated versus observation-based sediment composition for the setup used in this study is given in Appendix B of (Jeltsch-Thömmes et al., 2019). A table with all parameters applied here and by (Jeltsch-Thömmes et al., 2019) is given in the appendix (Table C1). Four solid tracers ($CaCO_3$, opal, POC, clay) and seven tracers in the porewater (DIC, DI^{13}C, DI^{14}C, alkalinity, phosphate, oxygen, and silicic acid) are modeled. The dissolution of $CaCO_3$ and POC depends on the respective weight fraction of $CaCO_3$ and POC in the solid phase of the sediment and the pore-water CO_3^{2-} and O_2 concentration, respectively. Denitrification is not considered in this model version, but O_2 is not consumed below a threshold, somewhat reflecting the process of denitrification without modeling NO_3^-. The respective reaction rate parameters for $CaCO_3$ dissolution and POC oxidation are global constants (see Roth et al., 2014; Jeltsch-Thömmes et al., 2019). The model assumes conservation of volume, i.e. the entire column of the sediments is pushed downward if deposition exceeds redissolution into pore waters. Any solid material that is pushed out of the diagenetic zone (top 10 cm) disappears into the subjacent diagenetically consolidated zone (burial or loss flux) (see Tschumi et al., 2011, for more details). The burial flux at preindustrial steady state is 0.22 GtC yr^{-1} in the form of $CaCO_3$, 0.24 GtC yr^{-1} in the form of POC, and 6.96 TmolSi yr^{-1} in the form of opal, all within the observational range. The global inventories in the interactive sediment layers amount to 916 GtC for $CaCO_3$, to 510 GtC for POC, and to 21,460 Tmol for opal. Carbonate chemistry within sediment pore waters is calculated as in the ocean by using the MOCSY routine of Orr and Epitalon (2015).

~~Weathering fluxes of PO$_4$, Alk~~Input fluxes by "weathering" of P, ALK, DIC, DI^{13}C, and ~~silicic acid~~ Si are added uniformly to the coastal surface ocean. ~~The global weathering fluxes~~ At the beginning of transient simulations, the global input fluxes of these compounds are set equal to the burial fluxes diagnosed at the end of the model spin-up. These input fluxes are jointly denoted as "weathering flux". These fluxes are further attributed to weathering of organic material, of $CaCO_3$, of $CaSiO_3$, and to volcanic CO_2 out gassing. The flux of P is assigned to weathering of organic material and related C and ALK fluxes are computed by multiplication of the P flux with the Redfield ratios P:C:Alk = 1:117:-17 for organic material. Similarly, the Si flux is assigned to $CaSiO_3$-weathering and the related ALK flux is computed using Si:ALK=1:2 based on the simplified equation for $CaSiO_3$-weathering: $2CO_2 + H_2O + CaSiO_3 \rightarrow Ca^{2+} + 2HCO_3^- + SiO_2$ (Colbourn et al., 2013). The remaining ALK flux is attributed to $CaCO_3$-weathering with the stoichiometric ratio C:ALK=1:2 following from $CO_2 + H_2O + CaCO_3 \rightarrow Ca^{2+} + 2HCO_3^-$. The volcanic flux is the remaining flux needed to balance the C input flux. The diagnosed fluxes at the end of the spin up are 0.24 GtC yr^{-1} for weathering of organic material, 0.14 GtC yr^{-1} for $CaCO_3$ weathering, 0.08 GtC yr^{-1} for volcanic CO_2 outgassing, and 6.96 Tmol Si yr^{-1} for $CaSiO_3$-weathering. The isotopic signature of the weathering carbon corresponds to the respective signature of the burial fluxes and amounts to δ^{13}C = -9.2 , intermediate between isotopically light organic carbon (δ^{13}C = -20.5) and heavier $CaCO_3$ (δ^{13}C = 2.9). During experiments, weathering fluxes of $CaCO_3$ and $CaSiO_3$, and accordingly DIC, DI^{13}C, and alkalinity, are allowed to vary as a function of surface air temperature, runoff, and net primary productivity (NPP). The parameterization of this weathering feedback follows equations described in detail in Colbourn et al.

(2013). The runoff dependence is parameterized as a function of temperature and for the productivity feedback the NPP from the coupled LPX-Bern model is used. We apply weathering feedbacks in the global average 0-D version (Colbourn et al., 2013, 2015).

The Bern3D model is coupled to the Land surface Processes and eXchanges (LPX) model v1.4 (Lienert and Joos, 2018) which is based on the Lund-Potsdam-Jena (LPJ) model (Sitch et al., 2003). In LPX, coupled nitrogen, water, and carbon cycles are simulated and vegetation composition is determined dynamically and represented with 20 (15 on natural and 5 on anthropogenically used land) plant functional types (PFTs). The PFTs compete within their bioclimatic limits for resources. CO_2 assimilation of plants is implemented following Farquhar et al. (1980) and Haxeltine and Prentice (1996a, b) and isotopic discrimination during photosynthesis is calculated according to Lloyd and Farquhar (1994). The carbon cycles of Bern3D and LPX-Bern are coupled through carbon and isotope exchange fluxes between the land and atmosphere and between the ocean and atmosphere. Climate change information from the Bern3D is passed on to LPX-Bern via a pattern scaling approach (Stocker et al., 2013). Spatial anomaly patterns in monthly temperature and precipitation, derived from a 21st century simulation with the Community Climate System Model (CCSM4), are scaled by the anomaly in global monthly mean surface air temperature as computed interactively by the Bern3D. These anomaly fields are added to the monthly baseline (1901 to 1931 AD) climatology of the Climate Research Unit (CRU) (Harris et al., 2014). A more detailed description of the LPX-Bern model can be found in Keller et al. (2017) and Lienert and Joos (2018).

2.2 Experimental protocol

The Bern3D model is spun-up over 60 thousand years (kyrs) to a pre-industrial steady state with 1850 AD boundary conditions. Atmospheric CO_2 is prescribed to 284.7 ppm, $\delta^{13}C$ to -6.305 ‰, and $\Delta^{14}C$ to 0 ‰. For LPX, the land area under anthropogenic use is fixed to its 1850 AD extent and kept constant in all simulations. The LPX-Bern model is spun-up uncoupled under identical 1850 AD boundary conditions over 2,500 years. Bern3D and LPX-Bern are then coupled and equilibrated for 500 years, again under fixed 1850 AD boundary conditions. After the spin-up, atmospheric CO_2 and its isotopic ratio are calculated interactively, with enabled carbon–climate feedbacks. Pulse experiments are started from the 1850 AD equilibrium state at nominal year -100. After 100 years, i.e., during nominal year 0 of the simulations, an external flux of carbon with characteristic isotopic signatures is removed from or added to the model atmosphere at a constant rate over the year. Runs are continued for 100 kyrs to simulate the redistribution of the added carbon and isotopes in the Earth system.

Table 1 summarizes run names and key characteristics of all simulations. Pulse sizes are varied between -250 GtC (removal) to +500 GtC (addition) with $\delta^{13}C$ of -24 ‰ and $\Delta^{14}C$ of 0 ‰. This corresponds to a hypothetical, sudden uptake or release of carbon from the land biosphere with a typical C3-like $\delta^{13}C$ signature. For simplicity and to ease interpretation, we set the $\Delta^{14}C$ of these land biosphere carbon pulses to the atmospheric signature; thus, we assume that the released material has been recently assimilated and neglect the small depletion in ^{14}C of "young" plant, litter, and soil material. In sensitivity experiments, $\Delta^{14}C$ is set to -500 ‰ and -1,000 ‰ to mimic the release of old, dead organic carbon, for example from buried peat or permafrost soils instead of young plant-derived material. In another simulation, the isotopic signatures are set to the signature for the modern mix of fossil fuels. Finally, we also performed a run where only ^{14}C, but no ^{12}C and ^{13}C is added to represent

Table 1. Overview of simulations

Run name	Pulse size (GtC)	δ^{13}C (‰)	Δ^{14}C (‰)	model setup
ctrl	0	–	–	std.
land biosphere C source				
WEA_{-250}	-250	-24	0	std.
WEA_{-100}	-100	-24	0	std.
WEA_{100}	100	-24	0	std.
WEA_{250}	250	-24	0	std.
WEA_{500}	500	-24	0	std.
old organic C source (old soils / fossil fuels)				
$^{14}C_{-500}$	100	-24	-500	std.
$^{14}C_{dead}$	100	-24	-1000	std.
WEA_{5000}	5000	-28	-1000	std.
radiocarbon production anomaly				
$^{14}C_{only}$	–	–	$(100\ \mathrm{GtC} \times {}^{14}\mathbf{R}_{std})^{a}$	std.
sensitivity to model setup				
SED_{500}	500	-24	0	no wea.[b]
SED_{ctrl}	0	–	–	no wea.[b]
CLO_{500}	500	-24	0	closed[c]
CLO_{ctrl}	0	–	–	closed[c]
$4box_{500}$	500	-24	0	4-box land[d]
$4box_{ctrl}$	0	–	–	4-box land[d]
LGM_{500}	500	-24	0	LGM[e]
LGM_{100}	100	-24	0	LGM[e]
LGM_{ctrl}	0	–	–	LGM[e]

[a] The number of ^{14}C atoms corresponding to 100 GtC of carbon with
Δ^{14}C=0 ‰ is added.

[b] Setup without $CaCO_3$ and $CaSiO_3$ weathering feedbacks.

[c] "Closed system": atm-ocean-land without ocean sediment module
and $CaCO_3$ and $CaSiO_3$ weathering feedbacks.

[d] Setup with 4-box land biosphere instead of LPX

[e] Setup with 4-box land biosphere instead of LPX under LGM conditions.

a change in radiocarbon production in the atmosphere. All these simulations were performed with fully interactive ocean sediments and enabled $CaCO_3$ and $CaSiO_3$ weathering feedbacks. The influence of the weathering feedback and of ocean-sediment interactions is quantified using two additional simulations. First, the weathering input flux is kept time invariant ("no weathering feedback"), Second, the sediment module is, in addition, not included in a so-called "closed" atmosphere-ocean-land model setup.

We also assess the influence of glacial climate boundary conditions and of a different land biosphere model. In two additional simulations, LGM_{500} and $4box_{500}$, the Bern3D setup and spin-up is as in WEA_{500}, except that an atmospheric CO_2 concentration of 278 ppm instead of 284.7 ppm is used and the pulse is released in the first timestep of simulation year 100 instead of distributed over the year. The model configuration includes reactive sediments and weathering feedbacks. A four-box terrestrial biosphere model (Siegenthaler and Oeschger, 1987), that allows for CO_2 fertilization, instead of LPX-Bern is coupled to the Bern3D in these runs. In LGM_{500} the model is forced by glacial boundary conditions instead of preindustrial conditions as in $4box_{500}$ and in WEA_{500}. CO_2 is set to 180 ppm and northern hemisphere ice sheets are set to Last Glacial Maximum coverage (Peltier, 1994). It has to be noted, however, that by forcing the model with 180 ppm during spin-up leads to less carbon stored in the ocean under LGM than PI conditions and results from LGM_{500} should be treated with some caution. Differences in results between WEA_{500} and $4box_{500}$ are due to differences in the two land biosphere models. Differences between $4box_{500}$ and LGM_{500} are exclusively due to differences in climatic boundary conditions.

2.3 Data reduction

The remaining fraction of a pulse-like perturbation or IRF at time t after the pulse release is defined for atmospheric CO_2 as

$$\text{IRF}(CO_{2,a})(t) = \frac{\Delta CO_{2,a}(t)}{\Delta CO_{2,a}^{ini}} = \frac{CO_{2,a}(t) - CO_{2,a}^{ctrl}(t)}{P / \left(2.12 \text{ GtC ppm}^{-1}\right)}. \tag{1}$$

Δ indicates a perturbation, here evaluated as difference between a simulation with pulse release and a corresponding control simulation. P indicates the pulse size in GtC which yields the initial atmospheric CO_2 perturbation in ppm when divided by $2.12 \text{ GtC ppm}^{-1}$. The superscript $ctrl$ refers to the control simulation without pulse, ini to the (maximum) initial perturbation assuming an instantaneous carbon release, and subscript a to the atmosphere. The IRF for $\delta^{13}C_a$ is:

$$\text{IRF}(\delta^{13}C_a)(t) = \frac{\delta^{13}C_a(t) - \delta^{13}C_a^{ctrl}(t)}{\Delta\delta^{13}C_a^{ini}}. \tag{2}$$

$\Delta\delta^{13}C_a^{ini}$ denotes the initial isotopic perturbation in the atmosphere and equals:

$$\Delta\delta^{13}C_a^{ini} = \frac{P}{N_{a,0} + P} \cdot (\delta^{13}C_P - \delta^{13}C_{a,0}). \tag{3}$$

$\delta^{13}C_P$ indicates the isotopic signature of the pulse, the subscript 0 the value prior to the pulse, and N_a the atmospheric carbon inventory. Analogous equations to Eqs. 2 and 3 hold for $\Delta^{14}C$.

An analytical expression for the IRF is calculated from experiment ~~p500~~WEA_{500}. The IRF is fitted by the sum of five exponential terms to

$$\text{IRF}(\text{CO}_{2,a}(t)) = a_0 + \sum_{i=1}^{5} a_i \cdot exp\left(\frac{-t}{\tau_i}\right) \; for \; t \geq 0 \tag{4}$$

using a least-squares optimization routine in Python. The coefficients a_i are fractions of the perturbation, each associated with a timescale τ_i, and a_0 the fraction of the perturbation remaining constantly in the atmosphere ($\tau_0 = \infty$). The sum over all six coefficients a_i equals 1. Modeled values are well reproduced with n=5 exponents. Differences between the original model output and the fit are insignificant for practical applications. Finally, we note that the IRF or remaining atmospheric fraction is in our experimental setup always smaller than one: the carbon is added at a constant rate during year 0 in the pulse simulations and part of this carbon is already taken up by the ocean during this initial year. Similarly, the IRF for $\delta^{13}C_a$ is fitted with n=4 exponents.

Principal component empirical orthogonal function (PC-EOF) analysis is used to fit the ^{13}C isotopic perturbations of dissolved inorganic carbon (DIC) in the ocean ($\Delta\delta^{13}C_{\text{DIC}}$). To this mean, the Python package $eofs$ (Dawson, 2016) is used to calculate principal component timeseries (PC(t)) and the spatial empirical orthogonal functions (EOF($\boldsymbol{x}$)) from the volume-weighted 4-D field of $\Delta\delta^{13}C_{\text{DIC}}(t,\boldsymbol{x})$. PCs and EOFs are then used to build a cost-efficient substitute model of the spatio-temporal evolution of $\Delta\delta^{13}C_{\text{DIC}}$ in response to an atmospheric pulse perturbation. The output frequency for marine 3-D tracer fields after the perturbation is every 10 years during the first 1 kyr, every 200 years until 10 kyrs and every 1 kyr thereafter. In the PC-EOF calculation this gives more weight to the first part of the simulation, where changes in the perturbation are larger.

2.4 ~~Results~~

3 <u>Results</u>

3.1 Earth system response to a pulse release of carbon

Impulse response functions for atmospheric CO$_2$ and δ^{13}C: We first describe the IRF for the atmospheric CO$_2$ perturbation using experiment ~~p250~~ WEA_{250} (Fig. 1a). The initial spike in response to the carbon release is followed by a substantial decline over the first decades due to carbon uptake by the upper ocean and land biosphere. The IRF is reduced to less than 40 % within the first century and decreases further on the timescale of ocean mixing to less than 16 % by year 2,000. The fit by exponentials (Table 2) yields time scales of 6, 47, and 362 years for this initial decline. They represent the continuum of carbon overturning time scales within the ocean and the land biosphere as well as time scales governing air-sea and air-land carbon exchange.

CaCO$_3$ compensation and weathering-burial imbalances remove the atmospheric perturbation on multi-millennial timescales such that after 10 kyrs less than 8 % and after 100 kyrs less than 2 % of the CO$_2$ perturbation remain airborne (Fig. 1a). The fit by exponentials shows that a fraction of 11.2 % of the initial perturbation is removed with a time scale of 5.5 kyrs. We associate these values with the process of CaCO$_3$ compensation. A remaining fraction of 4 to 5 % is removed with a time
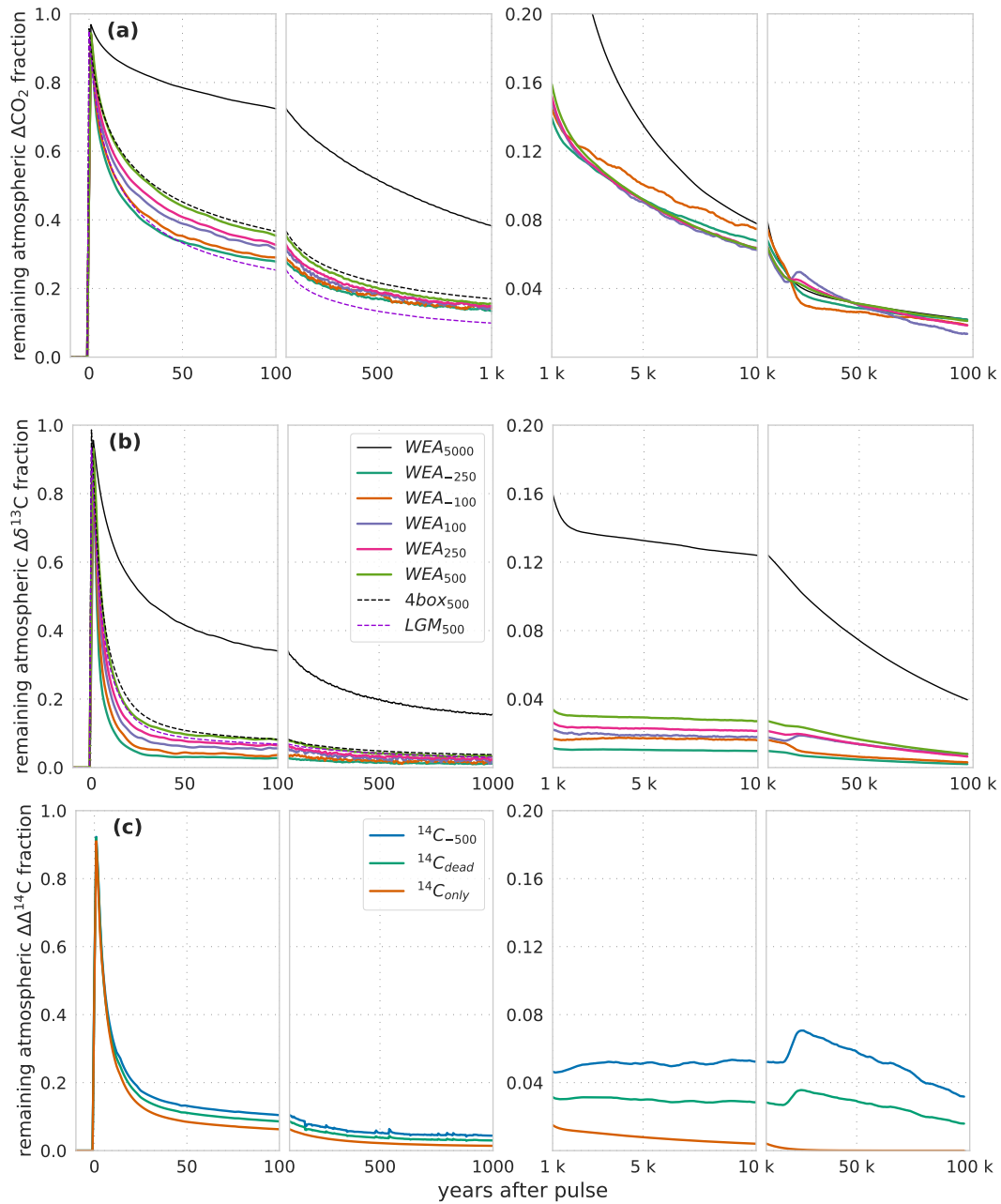
Figure 1. (a) CO_2,(b) $\delta^{13}C$, and (c) $\Delta^{14}C$ perturbation in the atmosphere for different simulations with different pulse sizes and model configurations. The isotopic signature is $\delta^{13}C$=-24 ‰ for all pulse sizes except the 5000 GtC pulse with $\delta^{13}C$=-28 ‰. ~~Dashed and dotted brown lines in panel (a) and (b) show results from a 500 pulse with no weathering feedback and no ocean sediments, respectively.~~ See Table 1 and section 2.2 for details of the experimental setup of the runs. ~~Note that the scaling of the second y-axis is different for the three panels.~~ Data are filtered with a moving average of 1000 ~~years~~ years in the interval 1 kyr - 10 kyrs and 5000 years in the interval 10 kyr - 100 kyrs for better visibility. ~~Note that experiment~~ Factorial simulations (WEA_{500}, SED_{500}, CLO_{500} ~~was run~~, $4box_{500}$, and LGM_{500}) for ~~90 instead of~~ the time interval 1 kyr to 100 kyrs are shown in Fig. 2 for better visibility.

9

Table 2. Fit parameters for IRF($\Delta CO_2(t)$) and IRF($\Delta \delta^{13}C_a(t)$) of ~~p500~~WEA_{500} and IRF($\Delta\Delta^{14}C_{a,dead}(t)$), and IRF($\Delta\Delta^{14}C_{a,only}(t)$). Note that in the case of IRF($\Delta\Delta^{14}C_{a,dead}(t)$) the actual fitting was done only with data until simulation year 15,000 to avoid complications from the sea-ice feedback in the control run (see main text and Fig. 1c).

	CO$_2$		$\delta^{13}C_a$		$\Delta^{14}C_{dead}$		$\Delta^{14}C_{only}$	
i	a_i	τ_i (yrs)	a_i	τ_i (yrs)	a_i	τ_i (yrs)	a_i	τ_i (yrs)
0	0.008	-	0.001	-	0.006	-	0.001	-
1	0.044	68,521	0.034	74,781	0.03	146,4130	0.017	7,510
2	0.112	5,312	0.034	436	0.0004	1,243	0.082	209
3	0.224	362	0.092	75	0.173	85	0.274	15
4	0.310	47	0.840	6	0.790	5	0.629	4
5	0.297	6						

scale of 69 kyrs (Table 2), linked to enhanced silicate rock weathering. The jumps visible at around 20 kyrs in Fig. ~~1~~ 1 arise from a sea ice-albedo feedback in the control run ~~and are thus~~ . They appear most pronounced in the experiments with ~~smaller perturbations.~~ small perturbations. The change in the control run in CO$_2$ is less than 1 ppm and less than 0.03 in $\delta^{13}CO_2$. These jumps are not of further relevance for our discussion. In comparison to others, our results show, up to a few percent, lower

5 remaining fractions for the 5000 GtC pulse (WEA_{5000}) than results presented by Colbourn et al. (2015) and Lord et al. (2016). The remaining airborne fraction of the CO$_2$ perturbation is 5 % and less after 100 kyrs in all studies.

Compared to CO$_2$, the atmospheric δ^{13}C perturbation is initially removed much faster (Fig. 1b). Within the first decades, IRF($\delta^{13}C_a$) is reduced to below 10 %. The further decline is slower and 1 kyr after the pulse, less than 3 % of the initial perturbation remains airborne. The remaining atmospheric perturbation is finally reduced to ≤ 1 % of the initial perturbation

10 at the end of the simulation (Fig. 1b). The fit by exponentials for IRF($\delta^{13}C_a$) (Table 2) shows that 84 % of the perturbation are removed with a timescale of 6 years, reflecting the initial fast decline seen in Fig. 1b when the perturbation is mixed in the upper ocean and living vegetation. About 9 % and 3 % are removed on timescales of 75 and 436 years, respectively, reflecting the decadal and centennial mixing of the perturbation in the land biosphere and deeper ocean. $\sim$3 % of the perturbation are finally removed with a timescale of $\sim$74 kyrs, in agreement with the e-folding timescale of the decline ($\sim$70 kyrs; see further

15 below). However, it has to be kept in mind, that these removal timescales result from a fit and thus several, different solutions are possible.

Processes: Next, we address the processes behind the different temporal evolution of CO$_{2,a}$ and $\delta^{13}C_a$. We focus on the ocean as ocean uptake is thought to dominate on long time scales. A perturbation in atmospheric CO$_2$ or in ^{13}CO$_2$ is communicated by air-sea gas exchange to the surface ocean and further transported, mainly by physical processes, to the deep

20 ocean. The fundamental difference between the IRF for CO$_{2,a}$ and $\delta 13C_a$ is linked to the aquatic carbonate chemistry and the associated equilibrium between dissolved CO$_2$, bicarbonate and carbonate ions (CO$_2$+ H$_2$O $\Leftrightarrow$HCO$_3^-$ + H$^+$ $\Leftrightarrow$CO$_3^{2-}$+2H$^+$) (Dickson et al., 2007). The removal of an atmospheric CO$_2$ perturbation is co-controlled by this acid-base carbonate chemistry

(Revelle and Suess, 1957). In contrast, the removal of a perturbation in the isotopic ratio $^{13}CO_2/^{12}CO_2$ is hardly affected by this chemical buffering, because $^{13}CO_2$ and $^{12}CO_2$ are affected approximately equally by the acid-base chemistry reactions. The chemical buffering diminishes the uptake capacity of the ocean for CO_2, but not for the isotopic ratio. Correspondingly, the IRF for $CO_{2,a}$ decreases less rapidly than the IRF for $\delta^{13}C_a$ and IRF($\delta^{13}C_a$) is smaller than IRF($CO_{2,a}$) over the simulation

5   period.

For an illustrative, semi-quantitative analysis, we developed approximate expressions for the IRF for $CO_{2,a}$ and $\delta^{13}C_a$ for time scales up to 2 kyrs as explained in the Appendix. Simplifying assumptions are that equilibrium between the atmosphere and a fraction of the ocean with the initial carbon inventory $N_{o,0}$ is assumed, while land biosphere carbon uptake and other climate-carbon cycle feedbacks are neglected. Changes in land biosphere carbon storage can be considerable, in particular

10   during the first century (see Fig. 3a). However, the role of the land carbon stock changes becomes smaller, the more carbon is taken up by the ocean and is thus for simplicity not considered in the analytical expression for CO_2. For CO_2 the ~~expressions~~ expression reads:

$$\text{IRF}_\infty(CO_{2,a}) = \frac{N_{a,0}}{N_{a,0} + \frac{1}{\xi}N_{o,0}}, \text{ for } 0 \leq t \leq 2 \text{ kyrs,} \tag{5}$$

The subscript a indicates the atmosphere and o the ocean, 0 the time prior to the pulse and ∞ the time when an effective ocean

15   volume with the initial carbon inventory $N_{o,0}$ is equilibrated with the atmosphere~~, P denotes again the pulse size. ξ is the oceanic buffer or Revelle Factor~~. ξ describes the influence of the acid-base carbonate chemistry on the relationship between the relative perturbation in the CO_2 partial pressure and in dissolved inorganic carbon (DIC) (Revelle and Suess, 1957). ξ varies with environmental conditions and increases with the size of the CO_2 perturbation. ξ is on the order of ~~10.~~ 10 for small pulse sizes. The dependency of IRF(CO_2) on the size of the carbon pulse is implicitly captured in the variable ξ. The key information

20   of eq. 5 is that the magnitude of the IRF is determined by the ratio of the (equilibrated) ocean carbon inventory and the buffer factor, $N_{o,0}/\xi$. The smaller this ratio, the larger is IRF($CO_{2,a}$).

For $\delta^{13}C_{\overline{a},a}$, we also consider the initial carbon inventory of the land biosphere ($\overline{N_{b,0}}$) ~~and develop a corresponding expression~~ $N_{b,0}$), as a substantial amount of the isotopic perturbation is contained in the land biosphere on multi-centennial to millennial timescales (Fig. 3b). The corresponding expression reads (for the derivation see the ~~Appendix~~appendix):

25   $$\text{IRF}_\infty(\delta^{13}C_a) = \frac{N_{a,0} + P}{N_{a,0} + N_{o,0} + N_{b,0} + P} \cdot \frac{(\delta^{13}C_P - \delta^{13}C_{mean})}{(\delta^{13}C_P - \delta^{13}C_{a,0})}, \text{ for } 0 \leq t \leq 2 \text{ kyrs} \tag{6}$$

Equation 6 shows that IRF($\delta^{13}C_a$) is described by the product of two ratios. The first ratio corresponds to the ratio of the carbon inventory in the atmosphere immediately after the pulse release to the total carbon inventory in the ("equilibrated") atmosphere-ocean-land biosphere system. It tells us that the pulse perturbation is mixed uniformly (see also Appendix eq. A20) and in proportion to the carbon inventories of the different reservoirs atmosphere, ocean, land biosphere. The second

30   fraction is about 1.2 and thus a correction term of order 20 % for small pulses sizes as typically applied in this study. It arises as the isotopic signature of the ocean and land biosphere is different from that of the atmosphere. $\delta^{13}C_{mean}$ corresponds to the weighted mean signature of the atmosphere, ocean and land biosphere, with the fraction of the pulse found in each of these reservoirs as weights (Appendix eq. A27). Remarkably, the buffer factor ξ does not directly show up in eq. 6. The reason is,

as noted already above, that CO_2 and $^{13}CO_2$ are both about equally affected by the aquatic chemistry. In turn, their ratio, i.e., $\delta^{13}C$, is hardly affected by this acid-base buffering.

Equation 5 and eq. 6 reveal the fundamental difference between a perturbation in CO_2 (and $^{13}CO_2$) and in the isotopic ratio, $\delta^{13}CO_2$. For small pulse sizes ($P \to 0$), neglecting the influence of the land biosphere and the correction term in eq. 6 for $\delta^{13}C$, eq. 6 and eq. 5 are formally equal, except that a buffer factor ξ of 1, instead of ~ 12 applies for $\delta^{13}C_a$. Eqs. 6 and 5 show: the pulse perturbation is distributed between the atmosphere and ocean proportionally to their initial carbon inventories $N_{a,0}$ and $N_{o,0}$ in the case of $\delta^{13}C_a$, but proportionally to $N_{a,0}$ and $N_{o,0}/\xi$ in the case of CO_2. As a consequence, the perturbation in the ratio $\delta^{13}C_a$ is apparently removed much ~~fast~~ faster than the perturbation in the concentration $CO_{2,a}$, despite that the time scales to transport a perturbation from the surface ocean to the deep ocean by advection, convection, and diffusion are the same.

We may illustrate this difference in the removal rate numerically. ξ is about 12 for a small pulse, $N_{a,0}$ is 600 GtC, $N_{o,0}$ is 37,400 GtC for the whole ocean. Further, the top 300 m with a carbon inventory of $\sim$2,600 GtC are approximately ventilated within a decade ~~.~~ through air-sea gas exchange and upper ocean physical transport processes (circulation, mixing). Then, the evaluation of eq. 5 yields for a small pulse that around 73 % and 16 % of the initial CO_2 perturbation are still found in the atmosphere after about 10 years and 2 kyrs, respectively. It has to be noted here that we assume ξ constant for small perturbations. With increasing pulse sizes, also ξ increases, leaving larger airborne fractions (c.f. WEA_{500} versus WEA_{5000} in Fig. 1a after 1-2 kyrs). Regarding $\delta^{13}C$, the corresponding fractions (eq. 6) are much smaller and 12 % to 31 % and 1 % to 3 % for small pulse sizes (-250 GtC to 500 GtC; see Appendix, text after eq. A14 for more details). We assume the perturbation to have mixed with 500 GtC and 2,700 GtC on land after 10 yr and 2 kyrs, respectively. These values are roughly in agreement with the values shown in Fig. 1a for pulse sizes of up to 500 GtC.

Turning to intermediate time scales ($t \leq 20$ kyrs), $CaCO_3$ compensation further reduces the atmospheric CO_2 perturbation and removes the differences in IRF($CO_{2,a}$) arising from different pulse sizes (Fig. 1a). The process of $CaCO_3$ compensation may be briefly explained as follows. CO_2 is taken up by the ocean and partly reacts to form bicarbonate (HCO_3^-) and hydrogen (H^+) ions. This makes the water more acidic; the carbonate ion concentration ($[CO_3^{2-}]$) is reduced and the water becomes corrosive to $CaCO_3$. In turn, sedimentary $CaCO_3$ dissolves to CO_3^{2-} and Ca^{2+} ions and less alkalinity and carbon, in the form of $CaCO_3$, is buried in the litosphere than delivered by weathering input. Alkalinity and DIC concentrations adjust in response to the excess weathering, a so-called terrrestrial neutralization, and a new equilibrium between weathering and burial fluxes is established. This chain of processes raises the alkalinity twice as much as the DIC concentration in the ocean and additional CO_2 is taken up from the atmosphere.

Again, an approximate expression for the IRF($CO_{2,a}$) is developed. This applies for the time when $CaCO_3$ compensation for the pulse perturbation is completed (see Appendix):

$$\text{IRF}_{CaCO_3}(CO_{2,a}) = 2 \cdot 1.5 \cdot \frac{N_{a,0}}{N_{o,0}}, \ \ \text{for } t \sim 20 \text{ kyrs} \tag{7}$$

The factor 2 in eq. 7 arises from the acid-base carbonate chemistry, the factor 1.5 from the change in the ocean carbon inventory due to excess dissolution (or burial) of $CaCO_3$, equivalent to $\sim 0.5 \times P$. The factor 1.5 is model dependent (see e.g. Archer et al., 1998) and also slightly different from previous Bern3D model versions. This equation shows that the airborne
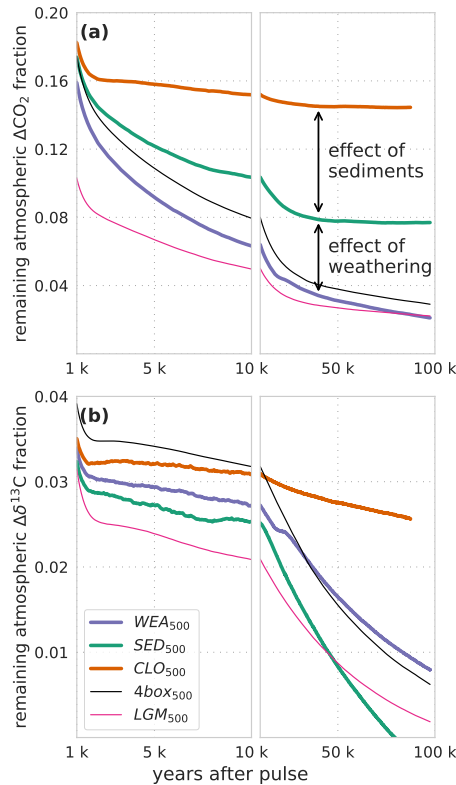
Figure 2. (a) CO_2 and (b) $\delta^{13}C$ perturbation in the atmosphere for the factorial simulations WEA_{500}, SED_{500}, CLO_{500}, $4box_{500}$, and LGM_{500}. Shown is the time interval 1 kyr to 100 kyrs Data are filtered with a moving average of 1000 years in the interval 1 kyr - 10 kyrs and 5000 years in the interval 10 kyr - 100 kyrs for better visibility. Note that experiment CLO_{500} was run for 90 instead of 100 kyrs.

fraction depends on the ratio of the initial atmosphere ($N_{a,0}$) to ocean carbon inventory ($N_{o,0}$), when $CaCO_3$ compensation is completed. Therefore, IRF_{CaCO_3} is (approximately) independent of the pulse size. Equation 7 successfully explains why $IRF(CO_{2,a})$ for pulse sizes from -250 to +5,000 GtC take on a nearly identical value of 5 % around $\sim$20 kyrs after the pulse.

$IRF(\delta^{13}C_a)$ stays nearly constant between 1 and 10 kyrs (Fig. 1b). This implies that $CaCO_3$ compensation has little influence on the removal of the $\delta^{13}C$ perturbation. Reasons are that the change in ocean carbon inventory due to $CaCO_3$ dissolution (burial) is small compared to the total ocean inventory and that the isotopic signature of $CaCO_3$ is similar to that of DIC.

On even longer time scales, the $CaSiO_3$ weathering feedback further removes the remaining perturbation in $CO_{2,a}$ with an e-folding time scale on the order of 70 kyrs. The perturbation in $\delta^{13}C_a$ is removed by the burial flux of organic carbon and $CaCO_3$. This burial flux removes the isotopic perturbation to the lithosphere. Surprisingly, the removal rate is substantially faster than expected from the residence time of carbon and highly sensitive to the gradients in the perturbation of $\delta^{13}C$ ($\Delta\delta^{13}C$) within the ocean as further discussed below in the context of the factorial simulations and in the Appendix.

Factorial simulations: We now turn to the factorial simulations to further quantify the effect of $CaCO_3$ compensation, burial fluxes, and $CaCO_3$ and $CaSiO_3$ weathering feedbacks on the CO_2 and $\delta^{13}C$ perturbations. The evolution of $IRF(CO_{2,a})$

13

for experiment SED_{500} (no terrestrial weathering feedback but with marine sediments) is comparable to ~~p500~~ WEA_{500} until simulation year 1,000 and differs thereafter due to varying weathering rates in ~~p500~~ WEA_{500} (Fig. 1a). There is no ~~additional~~ addition of alkalinity to the ocean from enhanced terrestrial weathering in SED_{500} and $\Delta CO_{2,a}$ levels out at a higher value than in ~~p500~~ WEA_{500}, with about 8 % of the perturbation remaining constantly airborne in SED_{500}. This value is in agreement with previous studies (e.g. Archer et al., 1998). It is somewhat higher than suggested by eq. 7 as this equation represents a simplification.

CaCO$_3$ compensation leads in both, ~~p500~~ WEA_{500} and SED_{500}, to a further removal of $\Delta CO_{2,a}$ on multi-millennial timescales as seen between 1 and 10 kyrs in Fig. 1a. After 10 kyrs, IRF(CO$_{2,a}$) decreases further as a result of weathering-burial imbalances in the CaCO$_3$ flux, also referred to as terrestrial neutralization (e.g. Archer et al., 1998; Colbourn et al., 2015). The e-folding timescale for this terrestrial neutralization from SED_{500} is about 11 kyrs, higher than the value provided by Archer et al. (1998) (8.5 kyrs) but in the range (8 to 12 kyrs) provided by Colbourn et al. (2015).

Comparing $\Delta\delta^{13}C_{atm}$ of SED_{500} and ~~p500~~ WEA_{500}, the evolution is initially comparable but on multi-millennial timescales the isotopic perturbation is, somewhat surprisingly and in contrast to the CO$_2$ perturbation, removed slower in ~~p500~~ WEA_{500} than in SED_{500}. In the case of SED_{500} the e-folding timescale is on the order of 20 to 30 kyrs. This is much shorter than expected from the mean residence time of carbon in the system of about 90 kyrs (Carbon inventory: $\sim$40,000 GtC; burial flux: 0.46 GtC yr^{-1}). The long-term removal time scale of $\Delta\delta^{13}C_{atm}$ is with about 70 kyrs also shorter than the residence time of carbon in simulation ~~p500~~ WEA_{500} with enabled weathering feedbacks. ~~The reason for the shorter e-folding timescale is apparent from Fig. 5g.~~ The isotopic perturbation is larger in the surface ocean than in the ocean mean. In turn, the perturbation is removed more efficiently than expected from the residence time of carbon (see Fig. B1). The isotopic signature of the carbon burial flux is mainly determined by the upper ocean isotopic signature which is more depleted than the ocean mean for ~~p500~~ WEA_{500}. In the case of SED_{500} this gradient is even stronger and ~~the surface perturbation much larger than the ocean mean (not shown) (~~ lasts longer (Fig. B1, see section 3.2 for further explanation). These results highlight the importance of spatial patterns within the ocean for the removal of an isotopic perturbation even for these very long-time scales. However, the absolute perturbation in $\delta^{13}C_a$ for these small pulse sizes and with $\delta^{13}C$=-24 ‰ is rather small after a few kyrs. For example, in the case of SED_{500}, $\Delta\delta^{13}C_a$ decreases to below 0.05 ‰ after $\sim$60 kyrs. The interannual variability from the LPX-Bern is of the same magnitude and also model drift starts to play a role.

Finally, we further exclude the effect of ocean sediment interactions and treat the atmosphere, ocean, and land biosphere as a closed system in CLO_{500}. Considering ocean mixing times of 1-2 kyrs, we would expect the CO$_2$ perturbation for experiment CLO_{500} to reach a steady state within 2 kyrs. The slow response timescale of peat carbon in the LPX-Bern model, however, leads to a further decline of $\Delta CO_{2,a}$ over multiple millennia (Fig. 1a). About 15 % of the initial perturbation remain constantly airborne in the closed system model setting as expected from eq. 5. $\delta^{13}C_a$ levels out around 2 kyrs at around 3 %, as expected from eq. 6. The further decrease on multi-millennial timescales results from model drift in the LPX-Bern.

Next, we compare WEA_{500}, where LPX-Bern is used as land model, with $4box_{500}$, where a 4-box land biosphere is used. Differences in IRF(CO$_{2,a}$) between WEA_{500} and $4box_{500}$ are due to the different land biosphere models. The four-box land biosphere model takes up less of the CVO$_2$ perturbation than LPX-Bern. The root mean squared deviation in IRF(CO$_{2,a}$) from

14

the two simulations is less than 1 % of the perturbation. Differences are most pronounced between simulation year 1 and 10,000 (Fig. 2a). Differences in IRF($\delta^{13}C_a$) (Fig. 2b) are largest in the first decades after the pulse and the root mean square deviation in IRF($\delta^{13}C_a$) amounts to less than 1 % between the two simulations.

Finally, we compare the simulations LGM_{500}, forced by glacial boundary conditions, and B3D$_{500}$, forced by preindustrial conditions. Differences between the two simulations are solely due to the difference in climate and CO$_2$ forcing. IRF(CO$_{2,a}$) is lower by a few percent in LGM_{500} compared to $4box_{500}$. The difference is largest in the first 10 kyrs and up to 12 % of the perturbation. The root mean square deviation between the two simulations amounts to $\sim$2 %. The larger oceanic carbon uptake in LGM_{500} than in $4box_{500}$ can be explained by the higher alkalinity simulated for LGM than for preindustrial conditions. A higher alkalinity implies lower values of the Revelle factor ξ and a larger carbon uptake capacity of the ocean. IRF($\delta^{13}C_a$) shows a similar pattern with lower values for the LGM background compared to the preindustrial background (cf. black dotted and dark violet dotted lines in Fig. 1b). The difference can be understood with the help of eq. 6; inserting the small glacial value for the atmospheric carbon inventory (381.6 GtC) in the nominator of the first term yields IRF$_\infty$($\delta^{13}C_a$)=0.027 compared to IRF$_\infty$($\delta^{13}C_a$)=0.032 when using the preindustrial value (589.4 GtC) in the equation. These estimates of IRF($\delta^{13}C_a$) are in good agreement with the results from LGM_{500} and $4box_{500}$, respectively (Fig. 2b). In summary, the influence of glacial compared to preindustrial boundary conditions on IRF($\delta^{13}C_a$ appears modest in our model.

The budgets of the carbon and carbon isotope perturbation: Next, we discuss the budgets of the carbon and ^{13}C perturbations~~for p250 (Fig. 2)~~. Fig. 3 shows results for simulation WEA_{250}, with a pulse release of 250 GtC, and for simulation WEA_{-250}, with a pulse removal of 250 GtC. Differences between these two runs are clearly visible in Fig. 3, but the general evolution of the budgets is similar. In the following, we give numerical results for simulation WEA_{250}. After 100 years, about 82 GtC are still airborne and the land and the ocean carbon inventories have increased by about 65 GtC and 105 GtC, respectively (Fig. 3a). As time evolves, the oceanic carbon perturbation grows at the cost of the atmosphere and land. On multi-millennial timescales, carbonate compensation and enhanced terrestrial carbonate and silicate weathering increase ocean alkalinity and thereby the uptake capacity for atmospheric CO$_2$ and the remaining atmospheric CO$_2$ fraction decreases. Nevertheless, the carbon perturbation in the atmosphere-ocean-land system exceeds the 250 GtC of the pulse as more carbon is added to the ocean through increased CaCO$_3$ weathering and redissolution/reduced burial of marine sediments (hatched area in Fig. 3a). The maximum perturbation is reached after $\sim$16 kyrs with a total of about 381 GtC in the atmosphere-ocean-land system. Thereafter, this inventory decreases due to weathering-burial imbalances. After 100 kyrs, about 5 GtC of the perturbation remain airborne, 8 GtC are stored in the land biosphere, and the ocean contains 163 GtC more carbon than before the perturbation. Accordingly, 74 GtC of the initial perturbation are lost from the atmosphere-ocean-land system through increased marine burial compared to terrestrial weathering input (hatched area extends below 250 GtC line in Fig. 3a).

The isotopic budget is established by expressing any isotopic inventory by the product of the corresponding carbon inventory times its isotopic signature in units of GtC ‰ . The role of the land biosphere in removing the $\delta^{13}C_a$ perturbation is clearly visible (Fig. 3b). After 100 years, the ocean contains $\sim$50 % of the isotopic perturbation (in GtC ‰), the land biosphere about 35 % and the atmosphere less than 15 %. On millennial timescales, the perturbation is slowly removed from the atmosphere-ocean-land system. The δ^{13}C perturbation of the burial flux (combined POC and CaCO$_3$) follows the negative
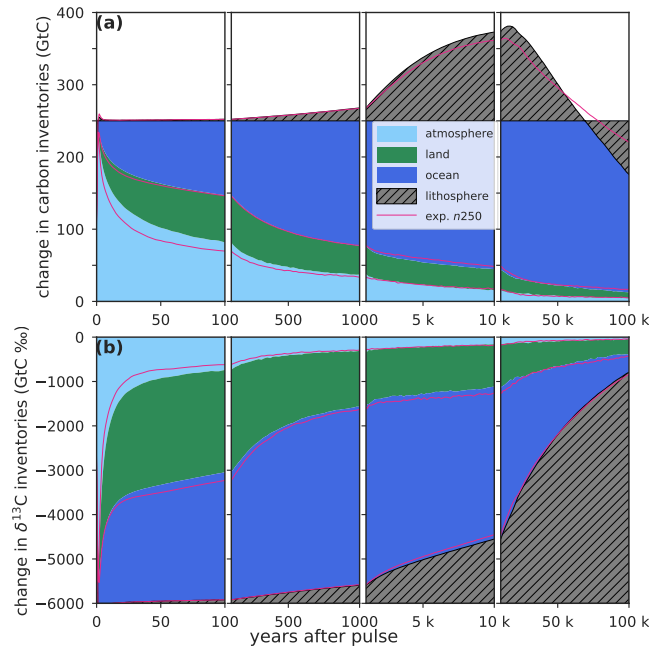
15

Figure 3. The budgets for the perturbations in (a) carbon and (b) δ^{13}C for experiment ~~p250~~ $\underset{\sim}{WEA_{250}}$. Shown are inventories of the perturbations in the atmosphere (light blue), the land biosphere (green), and the ocean (blue). Hatched areas indicate the influence of changes in the lithosphere (including sediments) due to $CaCO_3$ compensation and imbalances in the weathering and burial fluxes on the carbon and isotopic inventories of the ocean-atmosphere-land system. For carbon, this inventory is elevated above the pulse perturbation of 250 GtC until about 70 kyrs and depleted thereafter. For δ^{13}C, the atmosphere-ocean-land inventory is continuously reduced over the course of the simulation. Magenta lines show results for experiment ~~n250~~ $\underset{\sim}{WEA_{-250}}$ multiplied by -1.

δ^{13}C perturbation in surface DIC. In turn, the burial flux mitigates the δ^{13}C perturbation from the atmosphere-ocean-land biosphere system (Fig. ~~2~~ $\underset{\sim}{3}$b).

We further illustrate the contribution of the burial and weathering fluxes to the carbon and isotope budgets for the simulation with (WEA_{500}) and without weathering feedbacks (SED_{500}) in Fig. 4. The inventory in the relatively fast exchanging pools

5   – atmosphere, ocean, reactive sediments, land biosphere - increases by 350 GtC in addition to the pulse input of 500 GtC over the course of simulation SED_{500}. This additional increase is mainly due to a reduction in the burial of $CaCO_3$. In contrast, $CaCO_3$ burial is enhanced in simulation WEA_{500} and ~430 Gt of carbon are removed from the fast exchanging reservoirs. This removal is only partly compensated by enhanced weathering (~380 GtC), leading to a reduction in the inventory of the fast exchanging pools from 500 GtC immediately after the pulse to 453 GtC at 100 kyr. Changes in POC burial fluxes are

10 negligible for the carbon budget.

Turning to the isotopic pertubation budget, the initial perturbation due to the pulse input of -12,000 GtC ‰ is mainly removed by anomalies in the POC burial flux both in SED_{500} (~10,000 GtC ‰) and WEA_{500} (~7,000 GtC ‰). Changes in $CaCO_3$ burial and weathering mitigate about a quarter (~2,900 GtC ‰) of the initial isotopic perturbation in the two simulations. This

16

leaves a relatively small isotopic inventory perturbation of +1,100 and -1,600 GtC‰ in the fast exchanging reservoirs at 100 kyr in simulations SED_{500} and WEA_{500}.

The contributions of the anomalies in the POC and $CaCO_3$ burial fluxes may be approximately attributed to changes in the signature ($\Delta\delta$) and to changes in flux (ΔF) relative to the initial flux, F_0, and signature, δ_0, before the perturbation:

$$\Delta(F \cdot \delta) = F_0 \cdot \Delta\delta + \Delta F \cdot \delta_0 \tag{8}$$

The isotopic perturbation of the POC burial flux is mainly mediated by a change in the signature of the organic carbon buried ($\Delta\delta^{13}C(POC)$). For example, the signature of the total POC burial flux is on average 0.29 ‰ more negative than the corresponding input from weathering in simulation WEA_{500}. This change in signature of the total POC burial flux leads to an effective reduction of the isotopic perturbation. The change in POC burial flux ($\Delta F(POC)$) is, as mentioned above, negligible. Both changes in the signature of the total $CaCO_3$ burial flux and changes in $CaCO_3$ burial contribute significantly to the isotopic perturbation. At the end of simulation WEA_{500}, the mean $\delta^{13}C$ signature of $CaCO_3$ burial is on average 0.14 ‰ more negative than the input from weathering. In turn, the term $F_0 \cdot \Delta\delta$ for $CaCO_3$ burial contributes $\sim$ -3,100 GtC·‰ to the mitigation of the initial isotopic perturbation. This is partly counteracted by excess burial of $CaCO_3$, with $\Delta F \cdot \delta_0$ equal $\sim$1,300 GtC·‰. This yield an overall burial contribution of $\sim$ -1,800 GtC·‰. The $\delta^{13}C$ perturbation is further removed by increased weathering input of $CaCO_3$ (see methods), contributing about 1,100 GtC·‰ over 100 kyrs in WEA_{500}.

In summary, the isotopic perturbation is mainly mitigated by a change in the signature of the mean POC burial flux. The smaller contributions from the $CaCO_3$ cycle to the isotopic budget is related to both a change in the signature of the mean $CaCO_3$ burial flux and to changes in burial and weathering carbon fluxes.

Influence of pulse size: The IRF for atmospheric CO_2 and $\delta^{13}C$ is sensitive to the magnitude of the pulse size (Fig. 1a,b) and we next address related differences between simulations. For CO_2, the remaining atmospheric fraction is larger for larger than for smaller pulse sizes. Differences are most pronounced in the first decades to centuries for small pulse sizes (-250 GtC to 500 GtC) and the first millennia for large pulse sizes (~~p5000~~WEA_{5000}; Fig. 1a). Several processes contribute to these differences.

First, non-linearities in the carbonate chemistry contribute to differences in IRF($CO_{2,a}$) in the first centuries to millennia, where the perturbation is largely contained in the atmosphere-ocean-land biosphere system. We see from eq. 5 that a controlling factor is the oceanic buffer factor. As pulse size increases so does the buffer factor, leading to higher values of IRF($CO_{2,a}$) for ~~p5000~~ WEA_{5000} compared to smaller pulse sizes (Fig. 1a).

Second, productivity on land depends non-linearly on CO_2 (Farquhar et al., 1980) and the loss of carbon from the land biosphere in response to a negative pulse is larger than the uptake in response to a positive pulse of same size. This contributes to the initially smaller remaining atmospheric fraction for negative pulses (see e.g., ~~p250 and n250~~ WEA_{250} and WEA_{-250} in Fig. 1a and ~~2~~3a). The difference is most strongly pronounced in the first centuries and millennia but prevails until the end of the simulation.

Third, also the response in marine export production is not linear for pulses of same absolute size but different sign. The initial decrease in export production after a positive pulse is smaller than the increase after a negative pulse of same size, thereby affecting surface ocean CO_2 concentrations and thus air–sea gas exchange and partly leveling out the effect from the
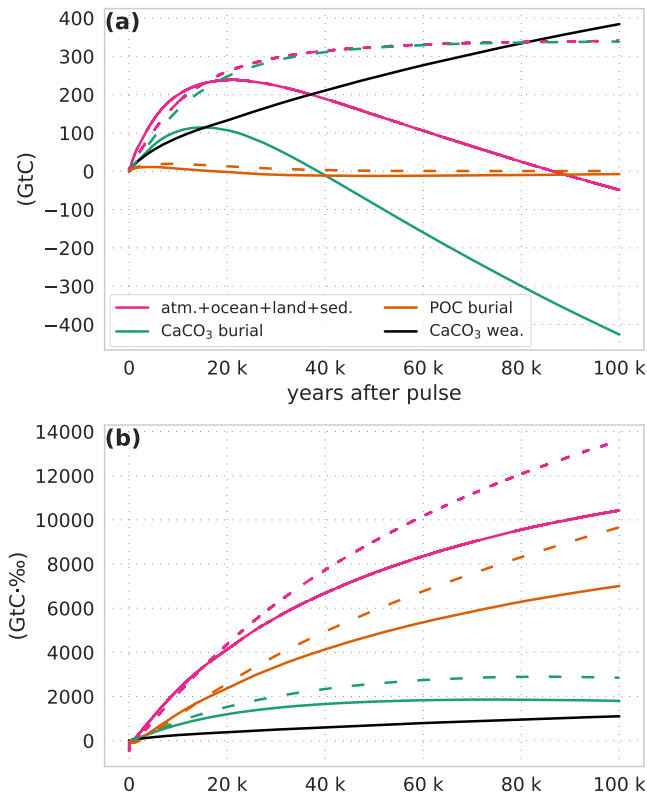
17

Figure 4. The perturbation budget for (a) carbon and (b) carbon isotopes. Solid lines show results from experiment WEA_{500}, dashed lines from experiment SED_{500}. In both panels the pulse (500 GtC, -12,000 GtC·‰) is subtracted from the combined atmosphere-ocean-land-reactive sediment inventory. Burial fluxes are plotted inversely and the sum of burial (red, orange lines) and weathering (black) fluxes yields the combined inventory (pink).

land biosphere. For $\delta^{13}C_a$, the perturbation is smaller for negative than positive pulses of same absolute size (Fig. 1). The difference can be understood with the help of eq. 6. Evaluation of eq. 6 (see Appendix) yields an IRF($\delta^{13}C_a$) of ~2 % for the pulse addition of 250 GtC ($\cancel{p250}WEA_{250}$), but of only ~1 % for a corresponding removal ($\cancel{n250}WEA_{-250}$).

Radiocarbon: Finally, we discuss the $\Delta^{14}C$ perturbation experiments. In experiment $^{14}C_{only}$, a positive pulse of ^{14}C is
5 added to the atmosphere but there is no perturbation in CO_2, analogous to a radiocarbon production pulse by atomic bomb tests or cosmic rays. The initial evolution of the IRF($\Delta^{14}C_a$) is very similar to the one of IRF($\delta^{13}C_a$) (Fig. 1b,c). On longer timescales, radioactive decay additionally removes the perturbation, so that after ~20 kyrs less than 0.1 % of the perturbation is left airborne. In simulations $^{14}C_{-500}$ and $^{14}C_{dead}$, a radiocarbon depleted carbon source of 100 GtC is added to the atmosphere causing a negative perturbation in $\Delta^{14}C$ and a positive perturbation in CO_2 in the atmosphere. As visible from Fig. 1a for
10 $\cancel{p100}WEA_{100}$, a small percentage of the CO_2 perturbation remains airborne even after 100 kyrs. This explains the persistence of a small atmospheric perturbation in $\Delta^{14}C$, well beyond the life time of the initially added ^{14}C. IRF($\Delta^{14}C_a$) is larger for

18

$^{14}C_{-500}$ than for $^{14}C_{dead}$ ~~, as~~ on these very long time scales. This is because the perturbation in CO_2 and, in turn, the long-term perturbation in $\Delta^{14}C_a$ is the same for both experiments. However, the initial perturbation in $\Delta^{14}C$ ~~was smaller than for~~ - the denominator of the response function (see eq. 2) - is smaller in $^{14}C_{-500}$ than $^{14}C_{dead}$.

3.2 The δ^{13}C perturbation of marine dissolved inorganic carbon and its approximation by PC-EOF

5 The ocean mean perturbation in δ^{13}C of DIC ($\Delta\delta^{13}C_{DIC}$) increases in absolute magnitude during the first millennium, as the atmospheric perturbation is propagated to the ocean (Fig. ~~3~~5, thick gray line). The most negative mean perturbation (-0.23 ‰ for experiment ~~p500~~WEA_{500}) occurs ∼1500 years after the pulse release (Fig. ~~3~~5), reflecting ocean mixing timescales. Thereafter, the $\delta^{13}C_{DIC}$ perturbation decreases in magnitude as a result of weathering-burial imbalances (see section 3.1, Fig. ~~2 and 3~~ 3 and 5). At the end of the simulation, less than 15 % of the maximum perturbation (-0.03 ‰) ~~remain~~ remains in the

10 ocean.

Deep ocean invasion of the $\delta^{13}C_{DIC}$ perturbation is first accomplished in the North Atlantic Deep Water (NADW) region. After 100 years, the signal has already propagated to a depth of∼3.5 km in the North Atlantic, whereas it is confined to the upper ocean (>1 km) in the rest of the ocean (Fig. ~~5~~6a). At year 1,000, the $\delta^{13}C_{DIC}$ perturbation is rather uniformly distributed in the ocean. Only the deep North Pacific (region of oldest waters; ideal age >1 kyr in the Bern3D) and waters

15 at intermediate depths in the Southern Ocean show a smaller perturbation (Fig. ~~5~~6c). On multi-millennial times, $\Delta\delta^{13}C_{DIC}$ decreases throughout the ocean. The perturbation, however, is not entirely uniformly distributed as expected from a completed ocean mixing by physical transport. More negative $\Delta\delta^{13}C_{DIC}$ values are present in the upper ocean and in North Atlantic Deep Water than in the intermediate and deep Southern Ocean, in Antarctic Bottom Water in the Atlantic, and the deep Pacific (Fig. ~~5~~6e,g). Reasons behind are changes in the fractionation during air-sea gas exchange due to higher temperatures,

20 enhanced by reduced fractionation during phytoplankton growth due to elevated CO_2 concentrations. Both processes lead to more negative δ^{13}C signatures in the surface ocean. Additionally, gross air-sea fluxes are increased as a result of the higher CO_2 concentrations, decreasing the air-sea disequilibrium. This leads to more negative δ^{13}C signatures in mid- and low-latitude surface waters and less negative in cold high-latitude waters (see e.g. Menviel et al., 2015). This surface to deep $\Delta\delta^{13}C_{DIC}$ gradient is dampened in the case of experiment ~~p500~~ WEA_{500} by enhanced weathering of $CaCO_3$ on land, adding carbon with

25 a positive δ^{13}C signature (∼2.9 ‰) to the surface ocean. As discussed above, these spatial $\Delta\delta^{13}$C gradients are important and co-govern the removal rate of the δ^{13}C perturbation. The larger than average δ^{13}C perturbation in the surface is communicated to phytoplankton and zooplankton, feeding the burial flux of biogenic material. This accelerates the removal of the δ^{13}C perturbation in comparison to a uniformly mixed ocean.

Next, the temporal evolution of the $\delta^{13}C_{DIC}$ perturbation and its spatial pattern are described by PC-EOF (Fig. ~~4~~7). The first

30 PC-EOF pair captures approximately the $\delta^{13}C_{DIC}$ evolution after 1 kyr, while the second and third PC-EOF pairs capture, toghether with the first pair, the decadal-to-century scale penetration of the perturbation into the ocean. The first EOF pattern (Fig. ~~4~~7a) shows negative values throughout the ocean, with a pattern similar to that modelled for year 50,000 (Fig. ~~5~~6g). The corresponding PC timeseries increases during the first decades after the pulse, followed by a slow decline on multi-millennial timescales (Fig. ~~4~~7b). This first PC captures the evolution of ocean mean $\Delta\delta^{13}C_{DIC}$ well after 1 kyr (Fig. ~~3~~ 5 blue versus gray
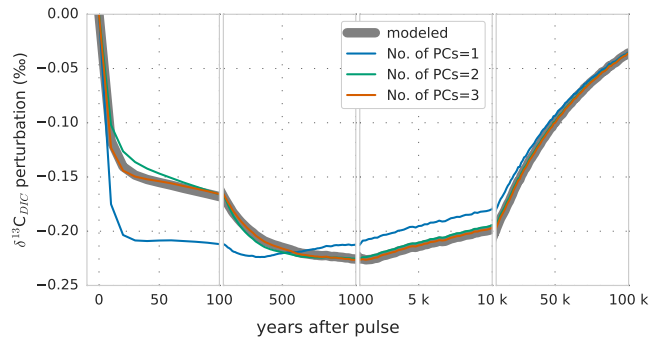
19

Figure 5. Modeled ~~and reconstructed~~ <u>global-average</u> perturbation of <u>the isotopic signature of dissolved inorganic carbon in the ocean</u> ($\delta^{13}C_{\overline{DIC}}$ <u>DIC; thick gray line) in response to a carbon pulse to the atmosphere of 500 GtC with a δ^{13}C signature of -24 ‰. The thin colored lines show the perturbation as reconstructed</u> with one <u>(blue)</u>, two <u>(green, dash)</u>, and three <u>(red)</u> principal components~~for a 500 carbon pulse with δ^{13}C = -24~~.

lines). In contrast to the first EOF, the second EOF has a clear dipole pattern with negative values in surface and intermediate waters and in the NADW region, and positive values below ~ 1 km depth (Fig. ~~4~~7c). The corresponding PC timeseries has high positive values in the first decades of the simulation, declining over the next centuries, becoming negative around year 500, and approaching zero on multi-millennial timescales. In combination with the first PC-EOF pair this leads to strongly negative δ^{13}C values in surface and intermediate waters in the first centuries of the simulation whereas on longer timescales the depth gradient in $\Delta\delta^{13}C_{DIC}$ disappears. The third PC-EOF, finally, is of importance during the first century (Fig. ~~4~~7b) and captures regional features, e.g. related to North Atlantic Deep Water or Intermediate Waters (Fig. ~~4~~7d).
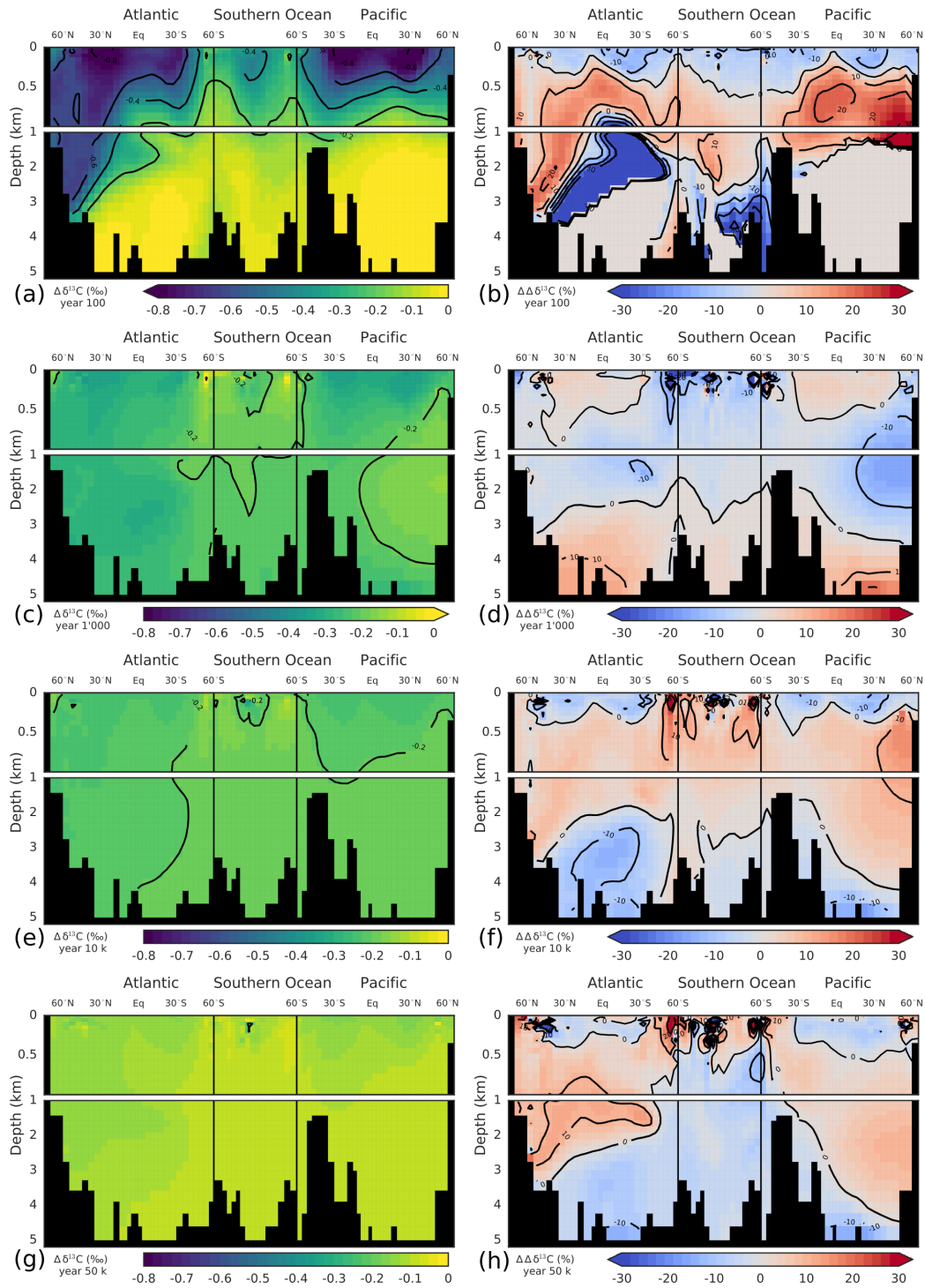
Figure 6. ~~EOF pattern~~ <u>Modeled $\delta^{13}C_{DIC}$ perturbation in ‰ (a,c,e,g) and difference between modeled and reconstructed $\delta^{13}C_{DIC}$</u> <u>perturbation using the first three principal components. These differences are shown in</u> % of the <u>modeled perturbation (b,d,f,h). Shown</u> <u>are time slices 100</u> years (a,<u>b)</u>~~first~~, <u>1</u> kyr (c,<u>d), 10</u> kyrs (e,f)~~second~~, and <u>50</u> kyrs (~~d~~<u>g,</u>h) ~~third principal component~~<u>after the pulse release</u> of carbon. ~~Corresponding PC timeseries are shown~~ <u>Note that</u> in panel (b) <u>perturbation values smaller than |0.05|</u> ‰ <u>(abyssal Atlantic and</u> <u>Pacific) have been masked for better visibility as the perturbation has not yet propagated into these regions (see panel (a)).</u>

21

The global mean $\Delta\delta^{13}C_{DIC}$ is well described by the first two PCs (Fig. ~~3~~5, green vs gray line). The third PC-EOF pair mostly adds performance during the first century (cf. green and orange lines in Fig. ~~3~~5) and reduces the root mean squared error (RMSE) between reconstructed and modelled global mean $\Delta\delta^{13}C_{DIC}$ from 0.003 ‰ with two PC-EOF pairs to 0.001 ‰ with three PC-EOF pairs used in the reconstruction.

5   For the reconstruction of the spatio-temporal evolution of $\Delta\delta^{13}C_{DIC}$, we will now use the first three PC-EOF pairs. The RMSE between the modelled and reconstructed 3-D field is highest (0.1 ‰) for the first 3-D output at year 10 after the pulse and decreases to 0.03 ‰ at year 100. As visible from Fig. ~~5~~6a and b, largest deviations between modeled and reconstructed $\Delta\delta^{13}C_{DIC}$ are found in the thermocline of the Pacific and in the deep northern Atlantic. Further, the modelled perturbation has not yet propagated to the deep Pacific and Atlantic by year 100 (Fig. ~~5~~6a), whereas the PC-EOF reconstruction displays a

10 $\Delta\delta^{13}C_{DIC}$ signal in these water masses. The performance of the reconstruction increases over the course of the simulation. The RMSE of the $\Delta\delta^{13}C_{DIC}$ fields amounts to 0.01 ‰ at 1 and 10 kyrs and decreases to 0.007 ‰ 50 kyrs after the pulse. Overall, reconstructing $\Delta\delta^{13}C_{DIC}$ with three PC-EOF pairs shows good results and deviations from the modeled $\Delta\delta^{13}C_{DIC}$ are of the order of 10 % of the perturbation and smaller on centennial to millennial timescales (Fig. ~~5~~6d,f,h). To reconstruct the modelled evolution of $\Delta\delta^{13}C_{DIC}$ precisely during the first few centuries after a perturbation, more than three PC-EOF

15 pairs are necessary. In summary, the spatio-temporal evolution of $\Delta\delta^{13}C_{DIC}$ over 100 years to 100 kyrs after a pulse input of carbon into the atmosphere is described accurately and conveniently by three PC-EOFs pairs.

4   Discussion and conclusion

The aim of this study is to investigate the evolution of a $\delta^{13}C$ perturbation in the Earth System in response to a carbon input to the atmosphere on time scales from centuries to 100 kyrs. To this end, the response of the Bern3D-LPX model was probed by

20 pulse-like emissions of carbon to the atmosphere from an external source such as land biosphere carbon release or fossil fuel burning. The $\delta^{13}C$ response is compared to that of atmospheric CO_2 and radiocarbon.

    The impulse response (or Green's) functions (IRF) for atmospheric CO_2 and its $\delta^{13}C$ signature are fitted by a sum of exponential functions. Additionally, we show that the spatio-temporal evolution of a $\delta^{13}C_{DIC}$ perturbation is reasonably represented with three PC-EOF pairs. Deviations between the PC-EOF reconstruction and modeled $\delta^{13}C_{DIC}$ results are

25 largest in the first decades after the pulse and are on the order of 10 % of the perturbation on millennial time scales. This allows the construction of a computationally efficient substitute model which can be applied to investigate, e.g., reconstructed $\delta^{13}C_{DIC}$ variations from marine sediments in future studies. The evolution of the atmospheric CO_2 perturbation in the coupled Bern3D-LPX model is comparable to results from earlier studies addressing the pulse-like input of carbon into the atmosphere ~~(e.g. Maier-Reimer and Hasselmann, 1987; Siegenthaler and Joos, 1992; Archer et al., 1998; Ridgwell and Hargreaves, 2007; Archer et al~~

30 (e.g. Maier-Reimer and Hasselmann, 1987; Siegenthaler and Joos, 1992; Archer et al., 1998; Ridgwell and Hargreaves, 2007; Archer et al . The inclusion of peat lands in the LPX-Bern model adds a (small) additional sink on multi-millennial timescales, previously not considered in such simulations. For the carbon isotopes, corresponding long-term pulse response simulations that consider
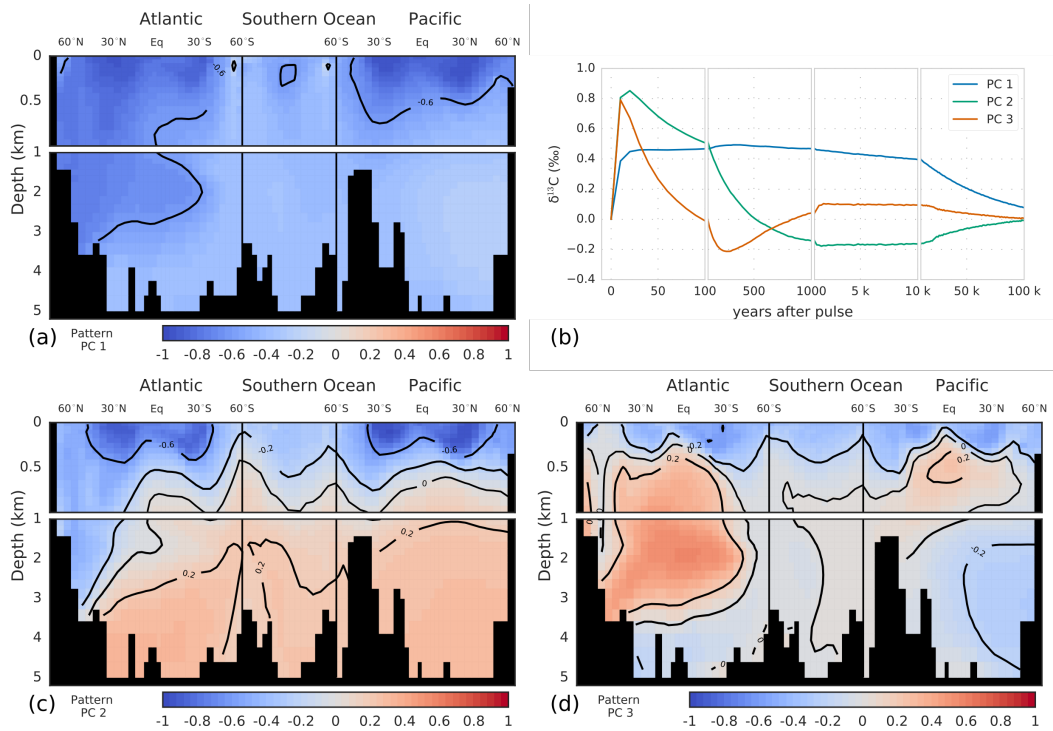
Figure 7. ~~Modeled $\delta^{13}C_{DIC}$ perturbation (a,c,e,g) and difference between modeled and reconstructed $\delta^{13}C_{DIC}$ perturbation using~~ EOF pattern of the ~~first three principal components in (b,d,f,h). Shown are time slices 100 years~~ (a,b) first, ~~1~~ (c,d), ~~10 (e,f)~~ second, and ~~50 (g,h~~d) ~~after the pulse release of carbon~~third principal component. ~~Note that~~ Corresponding PC timeseries are shown in ~~panel~~ (b)~~perturbation values smaller than |0.05| (abyssal Atlantic and Pacific) have been masked for better visibility as the perturbation has not yet propagated into these regions (see panel (a))~~.

ocean-sediment and weathering feedbacks appear missing in the literature. The "short-term" response from years to a couple of millennia is consistent with earlier results (Joos and Bruno, 1996).

We quantify the processes leading to the different removal timescales of atmospheric CO_2 and $\delta^{13}C_{atm}$ perturbations with the help of factorial experiments. The role of different processes are further illustrated by analytical descriptions derived from a two box atmosphere-ocean and three box atmosphere-ocean-land model provided in the Appendix. The removal of an atmospheric perturbation in the isotopic ratio $^{13}C/^{12}C$ is, unlike for CO_2, not buffered by marine carbonate chemistry. The atmospheric $\delta^{13}C$ perturbation is partitioned among the ocean, land biosphere, and atmosphere roughly in proportion to their carbon inventory over about 2 kyrs. This leaves only a very small fraction airborne (1 to 3 % for pulses of a few hundred GtC) after the signal is mixed within these three reservoirs. In contrast, a substantial fraction of carbon emissions and the CO_2 perturbation remains airborne for millennia. On time scales of a few millennia to 20 kyrs, the initial atmospheric CO_2 perturbation is lowered by carbonate compensation to a fraction of about 8 %. In contrast, this chemical buffering does hardly affect the atmospheric $\delta^{13}C$ perturbation. On even longer time scales, the CO_2 and the isotopic perturbation is removed by

different, though related processes. For δ^{13}C, the continuous flux of biogenic calcium carbonate and organic carbon particles carries the isotopic perturbation from the surface ocean to the lithosphere. For CO_2, the excess weathering of silicate rocks in response to the CO_2 and climate perturbation adds alkalinity to the ocean which leads to a complete removal of the atmospheric CO_2 perturbation.

5   Gradients in the $\delta^{13}C_{DIC}$ perturbation strongly influence the long-term removal timescale of the isotopic perturbation. In the pulse experiments, $\Delta\delta^{13}$C is enlarged in the surface relative to the deep ocean by temperature-dependent fractionation during air-sea gas exchange (Mook, 1986), CO_2-dependent fractionation by phytoplankton (Freeman and Hayes, 1992), and altered air-sea disequilibrium resulting from changes in gross exchange fluxes due to altered CO_2. Changes in $CaCO_3$ weathering on the other hand, diminish the surface perturbation (e.g. experiment ~~p500~~ WEA_{500} vs SED_{500} in Fig. 1a). As a result of

10 this gradient in $\Delta\delta^{13}$C, the isotopic perturbation is removed faster by particle burial than expected from a uniformly mixed ocean. This highlights the importance to resolve spatial structures in the perturbation to represent its removal time scales. More generally and beyond pulse release experiments, any process that changes the δ^{13}C signature of the relentless flux of organic and calcium carbonate particles, will influence the δ^{13}C loss flux from the ocean-atmosphere-land biosphere system to the litosphere (for examples see (Jeltsch-Thömmes et al., 2019; Roth et al., 2014; Tschumi et al., 2011)).

15   Our results have consequences for the interpretation of the difference in δ^{13}C between similar climate states such as the Penultimate Glacial Maximum (PGM) and the Last Glacial Maximum (LGM)~~or between the Eem and the Holocene warm periods.~~. Substantial temporal δ^{13}C differences between these periods are recorded in ice cores (Schneider et al., 2013; Eggleston et al., 2016) and in marine sediments (Hoogakker et al., 2006; Oliver et al., 2010). Different mechanisms, such as changes in the δ^{13}C signature of weathering and burial fluxes, varying contribution of volcanic outgassing of CO_2, and changes in

20 the amount of carbon stored in the land biosphere, especially in yedoma and permafrost soils, have been discussed for the PGM-LGM δ^{13}C offset (e.g. Lourantou et al., 2010; Schneider et al., 2013). An internal reorganization of the marine carbon cycle without considering changes in burial ~~can~~ may not explain the offset~~as the~~. With no changes in the weathering-burial balance, the mass in the atmosphere-ocean-land system remains constant. Then, a change in atmospheric δ^{13}C ~~signature of the combined atmosphere-ocean system changed.~~ would require an opposing δ^{13}C change in the ocean. This appears in conflict

25 with marine and ice core records which suggest that δ^{13}C increased both in the ocean and in atmosphere by about 0.3 ‰ between the PGM and LGM (Hoogakker et al., 2006; Oliver et al., 2010; Schneider et al., 2013; Eggleston et al., 2016). However, internal marine carbon cycle reorganizations, e.g., due to changes in circulation, may have altered δ^{13}C in the surface ocean, and in turn δ^{13}C of the burial flux, and thereby the balance between weathering input and burial.

     The Bern3D results suggest that changes in organic carbon storage on land (or in the ocean) are not a likely explanation of the

30 isotopic offset. ~~Rather, long-term imbalances in the weathering, volcanic, and burial fluxes appear to be a plausible cause~~ The δ^{13}C signal of a transfer of organic carbon of plausible magnitude to the atmosphere and ocean would have been attenuated too much over time to cause the observed PGM-LGM δ^{13}C difference. Schneider et al. (2013) estimated required changes in land carbon storage to match the ice core and marine temporal offsets in δ^{13}C using preliminary Bern3D results for pulse release simulations. Our results show, in agreement with these earlier results, that the isotopic perturbation associated with a terrestrial

35 carbon release is attenuated to less than 15 % within two millennia for pulse sizes of up to 5,000 GtC and declines thereafter

(see black line in Fig. 1b). This would require several thousand GtC to have been stored additionally in the land biosphere during the LGM compared to the PGM in order to explain the $\delta^{13}C$ offset (see also Schneider et al., 2013). This amount seems large in light of estimated total carbon stocks of ~1500 GtC in perennially frozen soils in Northern Hemisphere permafrost regions today (Tarnocai et al., 2009) and an even smaller inventory at the LGM ~~Lindgren et al. (2018)~~(Lindgren et al., 2018).

5   Taken together, these ad-hoc considerations suggest that long-term imbalances in the weathering (including volcanic emissions) and burial fluxes appear to be a plausible cause for the $\delta^{13}C$ differences between PGM and LGM. However, further work, which considers the transient evolution of CO_2, $\delta^{13}C$ and other proxies, is required to gain further insight into the contributions of individual mechanisms to long term $\delta^{13}C$ changes recorded in ice and marine cores.

   Further, the different behavior of CO_2 and $\delta^{13}C_{atm}$ perturbations has also consequences for centennial scale CO_2 and

10 $\delta^{13}C_{atm}$ variations such as during Heinrich Stadial (HS) 4 and 1. Variations in CO_2 and $\delta^{13}C_{atm}$ during HS4 and HS1 have been measured on Antarctic ice cores~~and~~. The data show an increase in CO_2 on the order of ~10 ~~ppm~~ppm over 200-300 years~~. The increase in CO_2 is~~, accompanied by a decrease in $\delta^{13}C_{atm}$ of ~0.2 ‰. This results in a value of roughly -0.02 ‰ per ppm for the ratio of the change in $\delta^{13}C$ to the change in CO_2 ($r = \Delta\delta^{13}C / \Delta CO_2$). These changes have been attributed to a release of terrestrial carbon to the atmosphere (Bauska et al., 2016, 2018). ~~From our experiments and eqs. 5 and 6,however,~~

15 ~~we would expect for a centennial scale event a stronger increase in~~

   We utilize our pulse response simulations under PI and LGM boundary conditions to estimate the changes in r in response to a transient terrestrial carbon input with an isotopic signature of -24 ‰. The results for r will depend on the evolution of the emissions into the atmosphere. For a pulse-like input at time zero the evolution of r after the pulse is shown in Fig. 8 for the first 2,000 years. r is about -0.08 (-0.06) ‰ ppm^{-1} immediately after the release under LGM (PI) boundary conditions. The

20 difference between LGM and PI values of r comes from the difference in the atmospheric C and ^{13}C inventory to which the pulse is added. The magnitude of r is reduced rapidly within the first 25 years and remains approximately constant at -0.015 (-0.01) ‰ ppm^{-1} thereafter. Thus, r recorded in ice after a hypothetical pulse release of carbon would be closer to -0.01 than -0.02 ‰ ppm^{-1} if the age distribution of the ice core samples is wider than a few decades. However, emissions may occur more gradually. For simplicity, we assume an emission pulse sustained over period T according to a two-sided Heaviside function;

25 terrestrial emissions, $e(t)$, suddenly increase to unity, remain elevated for period T, and are then immediately reduced again to zero. r is then readily calculated from the IRFs ($r = \int_0^T dt \cdot e(t) \cdot \text{IRF}(\delta^{13}C)(T-t) / \int_0^T dt \cdot e(t) \cdot \text{IRF}(CO_2)(T-t)$). The results for r are again plotted in Fig. 8. r is decreasing with the duration T of sustained emissions and falls below -0.02 ‰ ppm^{-1} for ~~a decrease in $\delta^{13}C_{atm}$ of ~0.2 . Idealized simulations show that~~ T larger than about 90 (30) years for LGM (PI) boundary conditions. Finally, we also performed simulations with the Bern3D-LPX under PI boundary conditions to account

30 for non-linearity that may not be captured in the IRF representation. The releases of varying amounts of terrestrial carbon with $\delta^{13}C$ = -24 ‰ over 100 to 400 years yield a linear response in ΔCO_2 and $\Delta\delta^{13}C_{atm}$ (Fig. ~~??) . Response in ΔCO_2 and~~ ~~$\Delta\delta^{13}C_{atm}$ to a uniform release of 20, 40, 80, 120, and 160 (colors) of isotopically light carbon ($\delta^{13}C$ = -24) to the atmosphere~~ ~~over 100, 200, 300, and 400 years (numbers). Shown is the mean over 30 years starting in the last year of the release. For a~~ ~~$\delta^{13}C_{atm}$ decrease of ~0.2 the results indicate a CO_2 change of~~ 8) with a slope r of about ~~20 ppm rather than 10 ppm (Fig.~~

35 ~~??). This estimate of 20 ppm may represent an upper limit as the assumed~~ -0.01 ‰ ppm^{-1}, in agreement with the IRF results.
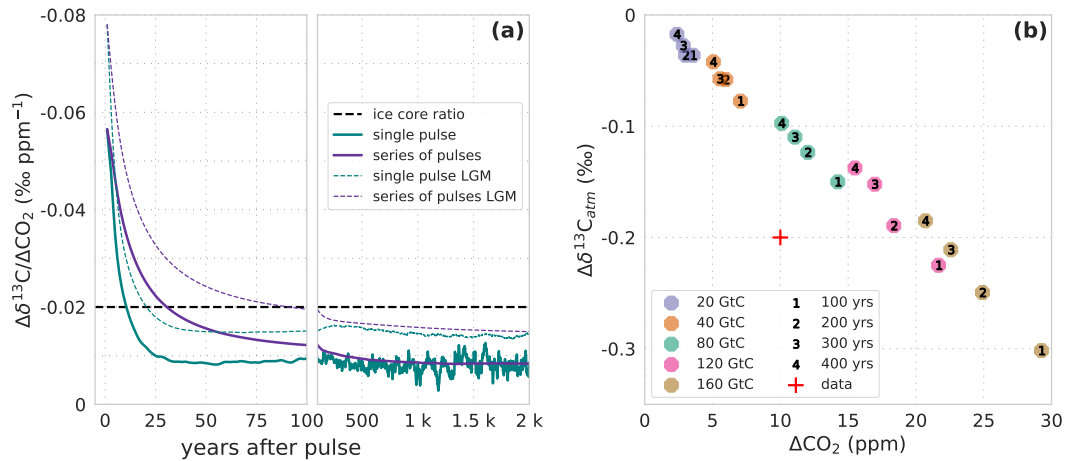
Figure 8. (a) First 2 kyrs of the $\Delta\delta^{13}$C to ΔCO_2 ratio of a 100 GtC pulse (WEA_{100}, LGM_{100}) plotted over time of single pulses (teal crosses) and series of pulses up to the "year after pulse" where plotted (purple crosses). Dashed horizontal line indicates a $\Delta\delta^{13}$C to ΔCO_2 ratio of 10 ppm to -0.2 ‰ as seen in ice core records for HS1 and HS4. (b) Response in ΔCO_2 and $\Delta\delta^{13}C_{atm}$ to a uniform release of 20, 40, 80, 120, and 160 GtC (colors) of isotopically light carbon (δ^{13}C = -24 ‰) to the atmosphere over 100, 200, 300, and 400 years (numbers). Shown is the mean over 30 years starting in the last year of the release. Red cross indicates the approx. $\Delta\delta^{13}$C to ΔCO_2 change as seen in ice core records for HS1 and HS4 (Bauska et al., 2016, 2018).

There are uncertainties in these estimates of r. We assumed that the emitted carbon was about -18 ‰ depleted with respect to the atmosphere. The relative uncertainty in this value translates directly to the relative uncertainty in r. The release of material that is isotopically even more depleted would bring our model results in better agreement with the ice core estimate of r. Observations and land model simulations suggest that the δ^{13}C ~~signature of~~ depletion in vegetation and soils may vary

5 between -24 ~~is for~~ ‰, for heavily discriminated C3 ~~plants and negative compared to that~~ plant material, to -5 ‰ indicative of C4 ~~plants, which were potentially favored during the glacial~~ plant material Keller et al. (2018). C4 plants were likely more abundant during glacials than interglacials (Collatz et al., 1998). Also, the values shown in Fig. ~~??~~ 8 for century-scale emissions are 30-year means. A wider gas age distribution would reduce the perturbation in $\delta^{13}C_{atm}$ more than in CO_2 (see e.g. Köhler et al., 2011). ~~An external input, such as a release of terrestrial carbon to the atmosphere, as~~ On the other hand, the CO_2 increase

10 may had occurred in less than 100 years (Bauska et al., 2018) and correspondingly a more negative value of r is expected for such a fast compared to a cenntenial scale increase. Given these uncertainties in our model estimates as well as in the determination of r from the ice core measurements, we are not in a position to firmly conclude whether a terrestrial carbon release was the sole mechanism for the HS1 and HS4 CO_2 events or not. Other mechanisms in addition to a terrestrial release may have contributed to the CO_2 and $\delta^{13}C_{atm}$ ~~excursion~~ excursions during HS4 and HS1~~seems thus unlikely~~.

15 We acknowledge that most of the idealized simulations presented in this study were run under preindustrial boundary conditions. A limited set of sensitivity simulations suggest that the IRFs for CO_2 and δ^{13}C are similar under preindustrial

and glacial CO_2 in our model. The direct influence of lower atmospheric CO_2 on IRF(δ^{13}C) appears limited. Further work is needed to better quantify the dependency of IRFs on the climate state.

In conclusion, the responses in atmospheric CO_2 and in $\delta^{13}C_{atm}$ to a carbon input (or removal) are different, with implications for the interpretation of paleo proxy data. The difference in response is related to the aquatic carbonate chemistry and the
5 burial weathering cycle, which affect $CO_{2,a}$ and its isotopic ratio differently.

Appendix A: Analytical expressions for the Impulse Response Functions of $CO_{2,a}$ and $\delta^{13}C_a$

10 **Ocean invasion of an atmospheric CO_2 perturbation:** The difference in the IRF for carbon and the isotopic ratios can be understood in terms of the aquatic carbonate chemistry. We develop approximate expressions for the IRF of atmospheric CO_2 (eq. A7) and δ^{13}C (eq. A29), starting in this section with IRF(CO_2).

For small pulses, changes in sea surface temperature and in CO_2 solubility, changes in ocean circulation, and changes in the marine biological cycle are small and neglected in the following. Changes in land biosphere carbon storage can be considerable,
15 in particular during the first century. However, the role of land carbon stock changes becomes smaller, the more carbon is taken up by the ocean and ~~can be neglected again~~is neglected for simplicity.

We consider a two box model of the atmosphere (index: a) and ocean (index: o) with area A=A_a=A_o and heights h_a and h_o. All boxes are assumed to be well mixed. Before the pulse addition, the model is in equilibrium and the initial CO_2 partial pressure is pCO$_{2,0}$=pCO$_{\overline{a,0}2,a,0}$=pCO$_{\overline{o,0}2,o,0}$. The initial concentration ~~in the atmosphere is $C_{a,0}$. In the ocean, the initial~~ of
20 dissolved inorganic carbon (DIC) ~~concentration~~ in the ocean is DIC$_0$ ~~. The carbon inventories in the atmosphere and ocean are N_a=$C_a \cdot h_a \cdot A$ and~~ and the carbon inventory in the ocean is given by N_o=DIC$\cdot h_o \cdot A$. We ~~express the atmospheric partial pressure and inventory~~relate the atmospheric carbon inventory, N_a, to a time-varying atmospheric concentration C_a and to the fixed volume of the model atmosphere: N_a=$C_a \cdot h_a \cdot A$. We are free to select the units of the model-specific concentration C_a. Here, we express C_a in units of ~~DIC$_0$ and define an atmospheric concentration~~, DIC$_0$ and set the initial atmospheric
25 concentration $C_{a,0}$ equal to DIC$_0$. The atmospheric inventory is proportional to the atmospheric partial pressure, pCO$_{2,a}$ and, correspondingly, C_a has to be proportional to pCO$_{2,a}$. This leads to the following definition of C_a:

$$C_a = \frac{\text{pCO}_{2,a}}{\text{pCO}_{2,0}}\text{DIC}_0, \tag{A1}$$

~~and~~ C is specifically defined for our box model and should not be confused with the concentration or mixing ratio of CO_2 in the real-world atmosphere. The atmospheric scale height h_a is given by the requirement that volume times concentration

equals inventory:

$$h_a = \frac{N_{a,0}}{A \cdot \text{DIC}_0}. \tag{A2}$$

The perturbation (Δ) from the initial equilibrium in pCO_2, and similarly for other quantities, is defined by: $\Delta pCO_2(t) = pCO_2(t) - pCO_2(t_0)$. The perturbation in $pCO_{2,o}$ is related to that in DIC by the Revelle factor ξ (Revelle and Suess, 1957):

5

$$\xi = \frac{\Delta pCO_{2,o}}{pCO_{2,0}} \cdot \frac{\text{DIC}_0}{\Delta \text{DIC}} \tag{A3}$$

We note that the carbonate chemistry is non-linear and ξ varies with environmental conditions (DIC, alkalinity, temperature, salinity). Assuming a constant Revelle factor ξ is therefore an approximation. In particular, ξ increases with increasing DIC. As a consequence, the "effective" value of ξ increases with increasing carbon emission and is thus the larger the larger the
10   magnitude of the carbon pulses. This yields for the perturbation in the net air-to-sea carbon flux per unit area, $\Delta f_{a->o,net}$:
$\Delta f_{a \to o,net}$:

$$\Delta f_{a->o,net} {\Delta f}_{a \to o,net} = k_g \cdot (\Delta pCO_{2,a} - \Delta pCO_{2,o}) = g \cdot (\Delta C_a - \xi \Delta \text{DIC}), \tag{A4}$$

$\Delta pCO_{2,a}$ and $\Delta pCO_{2,o}$ were replaced with the help of eq. A1 and A3 to obtain the right-hand side of eq. A4. k_g is the gas transfer rate relative to the partial pressure (Wanninkhof, 1992) and g the rate relative to DIC:

15   $$g = k_g \cdot \frac{pCO_{2,0}}{\text{DIC}_0}. \tag{A5}$$

The IRF, or equivalent the airborne fraction, is defined by:

$$\text{IRF}(CO_{2,a}(t)) = \frac{\Delta N_a(t)}{P} = \frac{\Delta N_a(t)}{\Delta N_a(t) + \Delta N_o(t)}, \qquad \text{for } t > t_0 \tag{A6}$$

P is the magnitude of the initial carbon pulse at time t_0 and this released carbon is conserved within the model atmosphere and ocean. The net air-to-sea flux becomes zero, when a new equilibrium at time t_∞ is reached; it follows from eq. A1 that
20   $C_{a,0} = \text{DIC}_0$ and from eq. A4 that $\Delta \text{DIC}_\infty = \Delta C_{a,\infty}/\xi$. Finally, using this and $\Delta N_a = \Delta C_a \cdot h_a \cdot A$ and $\Delta N_o = \Delta \text{DIC} \cdot h_o \cdot A = \Delta C_a/\xi \cdot h_o \cdot A$ yields for the IRF in an ocean-atmosphere system at equilibrium:

$$\text{IRF}_\infty(CO_{2,a}) = \frac{h_a}{h_a + \frac{1}{\xi} h_o} = \frac{N_{a,0}}{N_{a,0} + \frac{1}{\xi} N_{o,0}}. \tag{A7}$$

Distribution of a δ^{13}C perturbation within the atmosphere-ocean-land biosphere system: We now turn to the isotope ^{13}C. The isotopic ratio is given by (see e.g. Mook, 1986)):

25   $$^{13}R(C) = {}^{13}C/{}^{12}C, \tag{A8}$$

and the isotopic signature in permil by:

$$\delta^{13}C = \left(\frac{^{13}R}{^{13}R_{std}} - 1 \right) \cdot 1000. \tag{A9}$$

$^{13}R_{std}$ is the standard ratio. Isotopic discrimination is described by factors using the symbol α or by additive terms in δ-notation using symbol ε in permil. It holds:

$$\varepsilon = (\alpha - 1) \cdot 1000. \tag{A10}$$

In the following, we neglect for simplicity the order 1% difference between the concentration of ^{12}C and total C (this difference may be accounted for in the definition and values of the isotopic discrimination factors).

We address first the response during the first two millennia after the pulse. In the following paragraphs, we will develop a simple analytical expression for the IRF (δ^{13}C$_a$) after a new equilibrium for the atmosphere-ocean-land biosphere system is reached. Thus, we neglect carbonate compensation and weathering and burial fluxes. We consider exchange between the atmosphere and ocean, and between the atmosphere and land biosphere reservoirs and assume that these three reservoirs are well mixed.

The box model: The carbon and ^{13}C budgets for the 3-box model are described by:

$$\begin{aligned}
\frac{dN_o^i}{dt} &= F^i_{a->o\,a\to o} - F^i_{o->a\,o\to a} = F^i_{a->o,net\,a\to o,net} \\
\frac{dN_b^i}{dt} &= F^i_{a->b\,a\to b} - F^i_{b->a\,b\to a} = F^i_{a->b,net\,a\to b,net} \\
\frac{dN_a^i}{dt} &= -F^i_{a->o,net\,a\to o,net} - F^i_{a->b,net\,a\to b,net} + \delta(t) \cdot P^i \tag{A11}
\end{aligned}$$

N is the reservoir size (e.g. in GtC), indices a, o, and b denote the atmosphere, ocean, and land biosphere box, respectively. Index i refers either to carbon or ^{13}C. F denotes fluxes between reservoirs. δ is the Kronecker symbol and P^i the pulse released at time $t = t_0 = 0$ to the atmosphere.

The initial atmospheric $\delta^{13}C$ perturbation: The IRF(t) for δ^{13}C$_a$ is given by the perturbation in the isotopic signature, $\Delta\delta^{13}$C$_a$(t), divided by the initial (ini) perturbation. $\Delta\delta^{13}$C$_a^{ini}$. $\Delta\delta^{13}$C$_a^{ini}$ is the perturbation immediately after a carbon input of amount P and with signature ^{13}R$_P$ (δ^{13}C$_P$). Mass balance implies that the amount of ^{13}C before and after the pulse release is equal:

$$N_{a,0} \cdot {}^{13}R_{a,0} + P \cdot {}^{13}R_P = (N_{a,0} + P) \cdot {}^{13}R_a^{ini}. \tag{A12}$$

We convert the ratios to δ-units and subtract on both sides $(N_{a,0} + P) \cdot \delta^{13}C_{a,0}$ to get the initial perturbation:

$$\Delta\delta^{13}\text{C}_a^{ini} = \frac{P}{N_{a,0} + P} \cdot (\delta^{13}\text{C}_P - \delta^{13}\text{C}_{a,0}). \tag{A13}$$

$\Delta\delta^{13}$C$_a^{ini}$ is proportional to the difference between the signature of the pulse and the initial atmospheric signature. Thus, the initial perturbation is relative to the atmospheric δ^{13}C signature.

The relationship between $\delta^{13}C_a$, $\delta^{13}C_o$, and $\delta^{13}C_b$ at equilibrium: In this subsection, relationships between the isotopic signatures are developed by considering equilibrium between the three boxes. This will allow us to simplify the isotopic mass balance equations further below .

The gross air-to-sea flux per unit area is:

$$^{13}f_{a->o} = ^{13}k_g \cdot ^{13}pCO_{2,a} = k_g \cdot pCO_{2,a} \cdot ^{13}\alpha_{a->o} \cdot ^{13}R(pCO_{2,a}), \tag{A14}$$

where $^{13}\alpha_{a->s} = ^{13}k_g/k_g$ is the discrimination factor for the gross air-to-sea transfer. The gross sea-to-air flux is:

$$
\begin{aligned}
^{13}f_{o->a} = ^{13}k_g \cdot ^{13}pCO_{2,o} &= k_g \cdot pCO_{2,o} \left(\frac{^{13}k_g}{k_g} \frac{^{13}R(pCO_{2,o})}{^{13}R(DIC)} \right) \cdot ^{13}R(DIC) \\
&= k_g \cdot pCO_{2,o} \cdot ^{13}\alpha_{o->a} \cdot ^{13}R(DIC). \tag{A15}
\end{aligned}
$$

The term in parentheses is the the discrimination factor for the transfer of carbon from the DIC pool to the atmosphere, $^{13}\alpha_{o->a}$. At equilibrium (eq), the two gross fluxes cancel each other. It follows with $pCO_{2,a,eq} = pCO_{2,o,eq}$ and $^{13}pCO_{2,a,eq} = ^{13}pCO_{2,o,eq}$:

$$^{13}R_{eq}(pCO_{2,a}) = \frac{^{13}\alpha_{o->a}}{^{13}\alpha_{a->o}} \cdot ^{13}R_{eq}(DIC) = \frac{1}{\alpha_{a,o}} \cdot ^{13}R_{eq}(DIC). \tag{A16}$$

This equation gives the equilibrium relationship between the atmospheric and oceanic signature. $\alpha_{a,o}$ denotes the equilibrium discrimination factor between $pCO_{2,a}$ and DIC. $\alpha_{a,o}$ depends on temperature and somewhat on carbonate chemistry (Mook, 1986) and is about 1.008 and thus close to 1.

A similar relationship is readily developed for the isotopic ratio of the total carbon in the land biosphere. The gross fluxes between the land and atmosphere are:

$$
\begin{aligned}
^{13}F_{a->b} &= F_{a->b} \cdot ^{13}\alpha_{a->b} \cdot ^{13}R(pCO_{2,a}) \\
^{13}F_{b->a} &= F_{b->a} \cdot ^{13}\alpha_{b->a} \cdot ^{13}R(N_b). \tag{A17}
\end{aligned}
$$

This yields at equilibrium:

$$^{13}R_{eq}(pCO_{2,a}) = \frac{1}{\alpha_{a,b}} \cdot ^{13}R_{eq}(N_b) \tag{A18}$$

Eqs. A16 and A18 are readily converted into δ notation:

$$
\begin{aligned}
\delta^{13}C_{o,eq} &= \left(1 + \frac{\varepsilon_{a,o}}{1000}\right) \delta^{13}C_{a,eq} + \varepsilon_{a,o} \cong \delta^{13}C_{a,eq} + \varepsilon_{a,o}. \\
\delta^{13}C_{b,eq} &= \left(1 + \frac{\varepsilon_{a,b}}{1000}\right) \delta^{13}C_{a,eq} + \varepsilon_{a,b} \cong \delta^{13}C_{a,eq} + \varepsilon_{a,b}. \tag{A19}
\end{aligned}
$$

Eqs. A16, A18 and A19, allow us to express the isotopic signature of the land biosphere and the ocean by the isotopic signature of the atmosphere at equilibrium. These equations hold both for the initial equilibrium (t_0) before the pulse release and when a new equilibrium is reached at t_∞. In practice is t_∞ about 2 kyrs. It follows immediately from eq. A19 that the isotopic signatures at the new equilibrium are about equal for the three reservoirs:

$$\Delta\delta^{13}C_\infty = \Delta\delta^{13}C_{a,\infty} \cong \Delta\delta^{13}C_{o,\infty} \cong \Delta\delta^{13}C_{b,\infty}. \tag{A20}$$

In other words, the isotopic signal is mixed uniformly through the atmosphere, ocean, and land biosphere when assuming that these three reservoirs are well mixed as in this Appendix section.

Solving the mass balance equations of the isotopic pertubation for $\Delta\delta^{13}C$: The mass balance equations for the ocean-land biosphere-atmosphere system are given for carbon by:

$$N_{a,0} + N_{o,0} + N_{b,0} + P = N_{a,\infty} + N_{o,\infty} + N_{b,\infty}, \qquad \text{for } t > t_0$$

$$P = \Delta N_a + \Delta N_o + \Delta N_b. \tag{A21}$$

The second equation, describes the perturbation only. We use eqs. A16 and A18 to replace $N_o \cdot {}^{13}R_o$ with $\alpha_{a,o} \cdot N_o \cdot {}^{13}R_a$ and similar for the land reservoir and write the mass balance for ^{13}C:

$$(N_{a,0} + \alpha_{a,o} \cdot N_{o,0} + \alpha_{a,b} \cdot N_{b,0}) \cdot {}^{13}R_{a,0} + P \cdot {}^{13}R_P \qquad \text{for } t > t_0$$

$$= (N_{a,\infty} + \alpha_{a,o} \cdot N_{o,\infty} + \alpha_{a,b} \cdot N_{b,\infty}) \cdot {}^{13}R_{a,\infty}. \tag{A22}$$

Now we convert to δ units:

$$(N_{a,0} + \alpha_{a,o} \cdot N_{o,0} + \alpha_{a,b} \cdot N_{b,0} + P) \cdot 1000 + (N_{a,0} + \alpha_{a,o} \cdot N_{o,0} + \alpha_{a,b} \cdot N_{b,0}) \cdot \delta^{13}C_{a,0} + P \cdot \delta^{13}C_P$$

$$= (N_{a,\infty} + \alpha_{a,o} \cdot N_{o,\infty} + \alpha_{a,b} \cdot N_{b,\infty}) \cdot 1000 + (N_{a,\infty} + \alpha_{a,o} \cdot N_{o,\infty} + \alpha_{a,b} \cdot N_{b,\infty}) \cdot \delta^{13}C_{a,\infty}. \tag{A23}$$

We subtract on both side the mass balance equation for carbon (eq. A21) multiplied by factor 1000. Note that $\alpha_{a,o}$ and $\alpha_{a,b}$ are present in the carbon terms in eq. A23, but not in the mass balance for carbon (eq. A21). This difference results in the first two terms in eq. A24 below.

$$-\Delta N_{o,\infty} \cdot \overbrace{(\alpha_{a,o} - 1) \cdot 1000}^{\delta^{13}C_{DIC,0} - \delta^{13}C_{a,0}} \quad -\Delta N_{b,\infty} \cdot \overbrace{(\alpha_{a,b} - 1) \cdot 1000}^{\delta^{13}C_{b,0} - \delta^{13}C_{a,0}}$$

$$+(N_{a,0} + \alpha_{a,o} \cdot N_{o,0} + \alpha_{a,b} \cdot N_{b,0}) \cdot \delta^{13}C_{a,0} + P \cdot \delta^{13}C_P$$

$$= (N_{a,\infty} + \alpha_{a,o} \cdot N_{o,\infty} + \alpha_{a,b} \cdot N_{b,\infty}) \cdot \delta^{13}C_{a,\infty}. \tag{A24}$$

Next, we subtract on both sides the third left hand side term, $(N_{a,0} + \alpha_{a,o} \cdot N_{o,0} + \alpha_{a,b} \cdot N_{b,0}) \cdot \delta^{13}C_{a,0}$, as well as the term $P \cdot \delta^{13}C_{a,0}$. We rearrange and use again the mass balance for carbon to get:

$$-\Delta N_{o,\infty} \cdot (\delta^{13}C_{DIC,0} - \delta^{13}C_{a,0} \cdot (1 + \varepsilon_{a,o}/1000))$$

$$-\Delta N_{b,\infty} \cdot (\delta^{13}C_{b,0} - \delta^{13}C_{a,0} \cdot (1 + \varepsilon_{a,b}/1000)) - P \cdot (\delta^{13}C_a - \delta^{13}C_P)$$

$$= (N_{a,0} + N_{o,0} \cdot (1 + \varepsilon_{a,o}/1000) + N_{b,0} \cdot (1 + \varepsilon_{a,b}/1000) + P) \cdot \Delta\delta^{13}C_{a,\infty}$$

$$\tag{A25}$$

The terms with $\varepsilon/1000$ represent a small correction (< 0.02) and can be safely neglected. We replace P with $\Delta N_{a,\infty} + \Delta N_{o,\infty} + \Delta N_{b,\infty}$ in the above equation and exchange the left and right side to get the following mass balance for the δ^{13}C perturbation:

$$(N_{a,0} + N_{o,0} + N_{b,0} + P) \cdot \Delta\delta^{13}C_{a,\infty}$$

$$= \Delta N_{a,\infty} \cdot (\delta^{13}C_P - \delta^{13}C_{a,0}) + \Delta N_{o,\infty} \cdot (\delta^{13}C_P - \delta^{13}C_{DIC,0}) + \Delta N_{b,\infty} \cdot (\delta^{13}C_P - \delta^{13}C_{b,0})$$

$$= P \cdot (\delta^{13}C_P - \delta^{13}C_{mean}), \tag{A26}$$

with:

$$\delta^{13}C_{mean} = \frac{\Delta N_{a,\infty}}{P} \cdot \delta^{13}C_{a,0} + \frac{\Delta N_{o,\infty}}{P} \cdot \delta^{13}C_{o,0} + \frac{\Delta N_{b,\infty}}{P} \cdot \delta^{13}C_{b,0} \tag{A27}$$

Equation A26 represents the mass balance for the isotopic perturbation and its interpretation is as follows. The term on the left hand side equals the carbon mass in the system times the perturbation in the signature and therefore equals the total isotopic

5 perturbation in GtC ‰ . In equilibrium, the $\delta^{13}C$ perturbation, $\Delta\delta^{13}C_\infty$, is well mixed (eq. A20) within the total ocean-atmosphere carbon reservoir $(N_{a,0} + N_{o,0} + N_{b,0} + P)$. The terms after the first equal sign provide a different view of the total isotopic perturbation. In this picture, a fraction $\Delta N_{l,\infty}$ of the pulse is added to each reservoir (index l) with the perturbation in signature given by $(\delta^{13}C_P - \delta^{13}C_l)$. This is then summarized after the second equal sign by the product of the carbon input P times the isotopic perturbation of the pulse relative to the mean signature of the reservoirs absorbing this additional carbon,

10 $\delta^{13}C_P - \delta^{13}C_{mean}$.

By rearranging eq. A26 we get the perturbation in the isotopic signature of the atmosphere-ocean-land system:

$$\Delta\delta^{13}C_\infty = \frac{P}{N_{a,0} + N_{o,0} + N_{b,0} + P} \cdot \left(\delta^{13}C_P - \delta^{13}C_{mean}\right). \tag{A28}$$

In other words, the perturbation in the signature scales with the carbon mass ratio of the pulse input to the total mass in the system. This perturbation is also proportional to the difference between the signature of the pulse and the "mean" signature of

15 the system as defined by eq. A27.

IRF($\delta^{13}C_a$) at equilibrium ($t \sim 2$ kyrs): Finally, we use the definition for the IRF and eqs. A13 and A28 to obtain the following expression for the IRF at a new equilibrium for the ocean-atmosphere-land biosphere system:

$$
\begin{aligned}
\text{IRF}_\infty(\delta^{13}C_a) &= \frac{\Delta\delta^{13}C_{a,\infty}}{\Delta\delta^{13}C_a^{ini}} \\
&= \frac{N_{a,0} + P}{N_{a,0} + N_{o,0} + N_{b,0} + P} \cdot \frac{(\delta^{13}C_P - \delta^{13}C_{mean})}{(\delta^{13}C_P - \delta^{13}C_{a,0})}
\end{aligned} \tag{A29}
$$

20 The fraction of the initial perturbation in the atmosphere that remains airborne corresponds roughly to the ratio of the carbon in the atmosphere immediately after the pulse release to the total carbon in the system. The second fraction on the right side modifies this ratio by about +20 % for typical negative isotopic pulse perturbation applied in this study, because the mean signature is slightly heavier than the atmospheric signature. The nominator of this modifier reflects that the pulse perturbation is distributed within the system at the new equilibrium, while the denominator reflects that the pulse is initially added to the

25 atmosphere.

Ocean invasion: numerical examples: Equation A7 and eq. A29 provide simple expressions to approximate the IRF for the perturbation in atmospheric CO_2 and its istopic signature after a pulse-like carbon input. These equations illustrate the fundamental difference in the IRF for $CO_{2,a}$ and for $\delta^{13}C_a$. To ease interpretation, we neglect the land biosphere for the moment. Then, in the limit of $P \to 0$, eq. A7 and eq. A29 are formally identical for carbon and ^{13}C (index: i):

30 $$IRF^i \overset{P\to 0}{=} \frac{N_{a,0}}{N_{a,0} + \frac{1}{\xi^i}N_{o,0}} \cdot M^i \tag{A30}$$

However, for $\delta^{13}C_a$ a Revelle Factor of 1 instead of about 12 applies, while the modifier M is exactly 1 for $CO_{2,a}$ and around 1 for $\delta^{13}C_a$. The perturbation in the isotopic signature is diluted by the entire carbon inventory in the system, whereas the "available" ocean inventory is reduced by the Revelle Factor for the dilution of an atmospheric CO_2 pertubation.

Numerically, the preindustrial carbon inventory is $600\ \mathrm{GtC}$ in the atmosphere and $37,400\ \mathrm{GtC}$ in the ocean. These values are equivalent to a scale height of 69 m for the atmosphere and of 4,300 m for the ocean, when assuming a preindustrial (surface) concentration of DIC of 24 g/m^3 and an ocean area of $3.62 \cdot 10^{14}\ m^2$. The buffer factor is about 12 for small perturbations. This yields for $\mathrm{IRF}_\infty(CO_{2,a})$ a value of about 0.16. In other words, a fraction of about 16 % of a (small) carbon input into the atmosphere is still airborne after about 1 to 2 kyrs, when the ocean and atmosphere have approached a new equilibrium. The observed penetration of CFCs and bomb-produced radiocarbon suggests that an atmospheric perturbation penetrates about the top 300 m of the ocean within a decade. Thus, we expect that about 70 % of the initial perturbation are still found in the atmosphere after a decade. These numbers are comparable in magnitude to the IRF of CO_2 shown in Fig. 1a for 10 years and 2 kyrs after the pulse input. The buffer factor increases with the magnitude of the perturbation in DIC and pCO_2 and thus with pulse size P. Hence, IRF increases with increasing pulse size, as again shown in Fig. 1a. We note that any carbon uptake or release by the land biosphere is not taken into account in eq. A7 and in this discussion, in contrast to the results discussed in the main text.

To determine the IRF for $\delta^{13}C_a$, we take into account that the isotopic signal is also entering the land biosphere and assume a total inventory in the atmosphere-ocean–land system of 40,000 GtC. This yields an IRF_∞ of 1 % to 3.2 % for P varying between -250 to +500 GtC and of about 18 % for P equal 5,000 GtC and using $\delta^{13}C_{mean}$=4 ‰ (calculated with eq. A27). These values are in agreement with the estimates shown in Fig. 1b for year 2,000. Assuming that the isotopic perturbation has mixed within a layer of 300 m in the ocean ($\sim$2,600 GtC) and with the living vegetation on land (500 GtC) yiels a "decadal" IRF of about 12-31 % for small pulse sizes (-250 GtC to 500 GtC), again in agreement with the Bern3D-LPX results.

Carbonate compensation and terrestrial neutralization of the CO_2 perturbation: Next, we address $CaCO_3$ compensation of the carbon added by the pulse. We derive an expression for the $\mathrm{IRF}(CO_{2,a})$ at the time when $CaCO_3$ compensation of the pulse is completed - about 10-20 kyrs after the pulse input. The following calculations are based on Archer et al. (1998). As above, we assume the ocean to consist of a single, well-mixed box which is, after $CaCO_3$ compensation, again in equilibrium with the atmosphere. Concentrations of CO_2, HCO_3^-, and CO_3^{2-} in seawater are related by

$$\frac{pCO_{2,o} \cdot \left[CO_3^{2-}\right]}{\left[HCO_3^-\right]} = \frac{K_2' \cdot K_H}{K_1'} = const. \tag{A31}$$

K_1' and K_2' are the apparent dissociation constants for carbonic acid and K_H is the Henry's Law solubility product for CO_2. For simplicity, we assume the ratio of K_1', K_2', and K_H, which are temperature and salinity dependent, to be constant over the course of the experiments. With above assumption and by taking the ratio of initial and final states and by rearranging we get

$$\frac{pCO_{2,\infty}}{pCO_{2,0}} \approx \left(\frac{\left[HCO_{3,\infty}^-\right]}{\left[HCO_{3,0}^-\right]}\right)^2 \cdot \frac{\left[CO_{3,0}^{2-}\right]}{\left[CO_{3,\infty}^{2-}\right]}. \tag{A32}$$

Sedimentary dissolution of $CaCO_3$ in response to the carbon pulse tends to keep the carbonate ion concentration constant over the course of the simulations, yielding

$$\frac{pCO_{2,\infty}}{pCO_{2,0}} \approx \left(\frac{\left[HCO_{3,\infty}^- \right]}{\left[HCO_{3,0}^- \right]} \right)^2 . \tag{A33}$$

HCO_3^- is by far the dominant form of DIC. This allows one to approximate HCO_3^- by DIC in eq. A33 to get:

$$\frac{pCO_{2,\infty}}{pCO_{2,0}} \approx \left(\frac{DIC_{o,0} + \Delta DIC_o}{DIC_{o,0}} \right)^2 = \left(\frac{N_{o,0} + \Delta N_o}{N_{o,0}} \right)^2 . \tag{A34}$$

Δ refers here to the difference between the final and initial state. With pulse sizes substantially smaller than the oceanic DIC inventory, $\Delta N_o \ll N_{o,0}$ we approximate

$$\frac{pCO_{2,\infty}}{pCO_{2,0}} \approx 1 + 2 \cdot \frac{\Delta N_o}{N_{o,0}} . \tag{A35}$$

From Fig. 23b we see that on multi-millennial timescales the majority of the pulse is taken up by the ocean. Further, $CaCO_3$ 10 compensation and weathering-burial imbalances in the $CaCO_3$ cycle (terrestrial neutralization) add (or remove) additional carbon to (from) the ocean. We thus assume $\Delta N_o \approx 1.5 \cdot P$; P is the pulse size in GtC. The factor 1.5 is model dependent and slightly different here from the value provided by Archer et al. (1998) or in previous versions of the Bern3D model. This yields for the relative increase in pCO_2:

$$\frac{\Delta pCO_2}{pCO_{2,0}} \approx 3 \cdot \frac{P}{N_{o,0}} . \tag{A36}$$

15 We recall the definition of the airborne fraction:

$$IRF(CO_{2,a}) = 2.12 \, GtC \, \mu \, atm^{-1} \cdot \frac{\Delta pCO_{2,a}}{P} . \tag{A37}$$

Finally, with eq. A36 and A37 we express the IRF at the time when $CaCO_3$ compensation is completed by

$$IRF_{CaCO_3}(CO_{2,a}) = 3 \cdot 2.12 \, GtC \, \mu atm^{-1} \cdot \frac{pCO_{2,0}}{N_{o,0}} . \tag{A38}$$

The remaining atmospheric fraction is thus independent of the pulse size for $P \ll N_{o,0}$. Its magnitude results directly from the 20 carbonate chemistry (Archer et al., 1998). With a pre-industrial ocean DIC inventory of 37,400 GtC and surface ocean pCO_2 of 284 μatm we get a remaining airborne perturbation of $\sim$5 %. This is in agreement with results from the Bern3D-LPX model after about 10-20 kyrs (Fig. 1a).

Carbonate compensation of the δ^{13}C perturbation: Carbonate compensation has almost a negligible influence on the δ^{13}C perturbation. The carbonate compensation process acts, aside from small isotopic discrimination, equally on the different 25 isotopes. Therefore, $^{12}CO_{2,a}$ and $^{13}CO_{2,a}$ both decrease according to eq. A38, leaving the isotopic ratio in first order approximation unchanged. Additional effects are, here formulated for a positive pulse, as follows. The dissolution of $CaCO_3$ adds an isotopic perturbation to the ocean-atmosphere-land system. The amount of carbon added corresponds to about half of the

pulse size, P. $CaCO_3$ has a $\delta^{13}C$ signature of about +2.9 ‰ compared to -24 ‰ of the pulse. We reference the $CaCO_3$ isotopic perturbation relative to the mean signature of the ocean in the model ($\sim$0.8 ‰) as this additional carbon remains mainly in the ocean, while the mean signature that applies for the pulse is according to eq. A27 about -3 ‰ for pulse sizes between -250 GtC and 500 GtC. Thus the isotopic perturbation by $CaCO_3$ dissolution is about 20 times smaller than that of the pulse

5 ($0.5 \times P \times$ (2.9 ‰ - 0.8 ‰) : $P \times (-24$ ‰ $+ 3$ ‰) = -1:20). The dissolution of $CaCO_3$ enlarges the carbon reservoir by which the initial atmospheric $\delta^{13}C$ is diluted. However, the amount of added carbon is, except for the 5,000 GtC pulse, small compared the total inventory of the system of about 40,000 GtC. In summary, the influence of $CaCO_3$ compensation on $\delta^{13}C_a$ is small and eq. A29 is still approximately valid for the time scale of $CaCO_3$ compensation.

Removal of the remaining CO_2 perturbation by silicate weathering: Finally, on timescales of hundreds of thousands
10 of years imbalances in the weathering and burial fluxes remove any remaining perturbation in carbon from the atmosphere-ocean-land system. Silicate rock weathering leads to a net removal of carbon from the atmosphere by the following simplified reaction (see Colbourn et al., 2013, for more details):

$$2CO_{2(aq)} + H_2O_{(l)} + CaSiO_{3,(s)} \rightarrow Ca^{2+}_{(aq)} + 2HCO^-_{3(aq)} + SiO_{2(aq)}. \tag{A39}$$
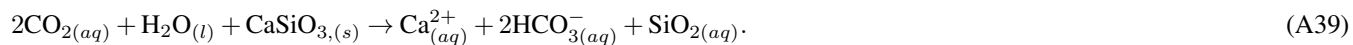
The timescale for this silicate weathering feedback has been determined to be on the order of 240 kyrs (Colbourn et al., 2015)
15 and 270 kyrs ~~(?)~~(Lord et al., 2016), however with a large spread. Silicate rock weathering removes the remaining atmospheric perturbation ($\sim$8 %). Further, the additional alkalinity added to the ocean deepens the saturation horizon, resulting in higher carbon burial in marine sediments and thus also removes the DIC perturbation (see Fig. ~~2~~3a).

Removal of the remaining $\delta^{13}C$ perturbation by burial of organic matter and $CaCO_3$: In the case of $\delta^{13}C$, silicate rock weathering has no direct effect on the $\delta^{13}C$ signature. The perturbation is removed on these long timescales by the replacement
20 of carbon through burial of organic matter and $CaCO_3$ and weathering inputs:

$$\frac{d}{dt}(N_S \cdot \Delta\delta^{13}C_S) = -F_{burial} \cdot \Delta\delta^{13}C_{burial}, \tag{A40}$$

with N_S and $\Delta\delta^{13}C_S$ equal the total mass and mean isotopic perturbation in the atmosphere-ocean-land system and F_{burial} the burial flux of carbon leaving the system and $\Delta\delta^{13}C_{burial}$ its isotopic signature. In simulations with constant weathering rates, the residence time of carbon in the atmosphere-ocean-land system is on the order of $\tau = N/F_{burial} \sim 90$ kyrs
25 (burial/weathering input is 0.46 GtC yr^{-1}, total amount: $\sim$ 40,000 GtC)). Surprisingly, in the factorial simulation with sediments and constant weathering fluxes (SED_{500}), the perturbation is removed much faster than expected from the mean residence time (Fig. 1b, dotted line), because the isotopic perturbation of the burial flux is larger than that of the ocean-atmosphere-land system.

The long-term removal rate of the $\delta^{13}C$ perturbation is sensitive to $\Delta\delta^{13}C$ gradients in the ocean. The isotopic signature of
30 the burial flux is mainly determined by the upper ocean signature. Changes in the gross exchange fluxes of carbon between the atmosphere and the ocean in response to perturbed CO_2 and changes in the isotopic fractionation of air-sea fluxes in response to perturbed temperatures increase the $\Delta\delta^{13}C$ perturbation in the upper ocean relative to the deep. In case of enabled weathering feedbacks, the additional flux of isotopically heavy carbon from excess weathering partly mitigates surface-to-deep $\Delta\delta^{13}C$

35

gradients. In turn, the perturbation is removed faster in simulations with enabled weathering feedback compared to simulations with constant weathering. Taken together, this highlights the role of spatial patterns of the δ^{13}C perturbation even on these very long timescales.

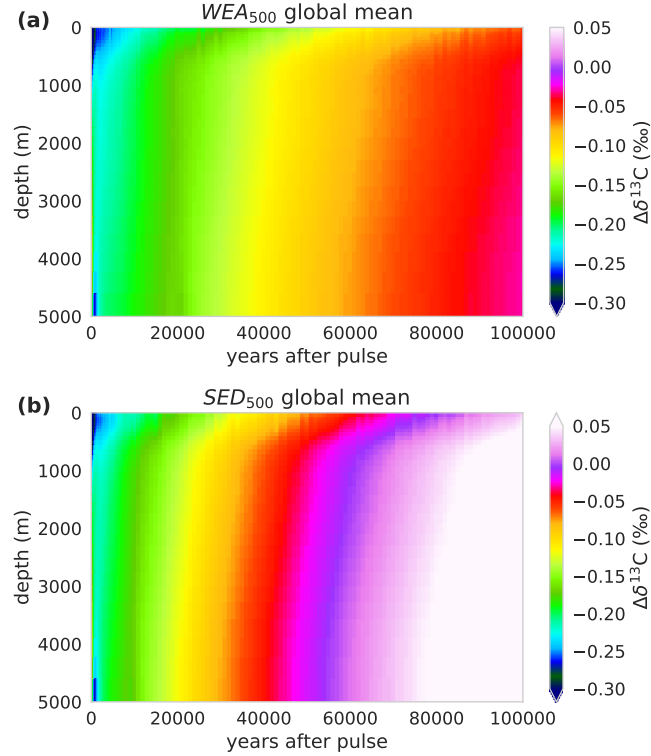## Appendix B: Temporal evolution of surface to deep ocean $\Delta\delta^{13}C_{DIC}$ gradient

Figure B1. Hovmoeller-type diagram of global $\Delta\delta^{13}C_{DIC}$ for experiment (a) WEA_{500} and (b) SED_{500}.

5   **Appendix C: Sediment module and weathering feedback**

Parameterization of weathering feedbacks on land: We use the 0-D version of the Rock Geochemical Model v0.9 (Colbourn et al., 2013) . Weathering of CaCO$_3$ and CaSiO$_3$ are parameterized as functions of temperature (T), runoff (R) and productivity (P) in the following form for CaCO$_3$:

$$F_{CaCO_3} = F_{CaCO_3,0}(1 + k_{Ca}(T - T_0))\frac{R}{R_0}\frac{P}{P_0} \tag{C1}$$

and for $CaSiO_3$:

$$F_{CaSiO_3} = F_{CaSiO_3,0} \cdot e^{\frac{1000E_0}{RT_0^2}(T-T_0)} \cdot \left(\frac{R}{R_0}\right)^\beta \frac{P}{P_0}. \tag{C2}$$

0 indicates the initial value diagnosed prior to the pulse, k_{Ca} stems from a correlation between temperature and HCO_3^- ion concentration of groundwater with a value of 0.049, E_a is the activation energy for silicate weathering (63 kJ mol^{-1}), β is taken as 0.65, and R indicates run-off and is parameterized as a function of temperature:

$$\frac{R}{R_0} = \max\{0, 1 + k_{run}(T - T_0)\} \tag{C3}$$

with $k_{run} = 0.025$. In the case of experiments $4box_{500}$ and LGM_{500}, LPX-Bern was not coupled and instead productivity was parameterized, again following equations given in Colbourn et al. (2013), as:

$$\frac{P}{P_0} = \left(\frac{2\frac{C}{C_0}}{1 + \frac{C}{C_0}}\right)^{0.4} \tag{C4}$$

with C being atmospheric CO_2 in ppm. For further details and discussion of parameter value choices, the reader is referred to Colbourn et al. (2013).

Table C1. Parameters used for the sediment module, similar to what is shown in the appendix A of Tschumi et al. (2011) and with updates from Roth et al. (2014) and Jeltsch-Thömmes et al. (2019).

Parameter	Value	Unit	Reference
Number of time steps per year	96	-	Roth et al. (2014)
Density of solid sediment components	2.6	$g\,cm^{-3}$	Heinze et al. (1999)
Molar weight of POM	32.74	$g\,mol^{-1}$	Heinze et al. (1999)
Molar weight of $CaCO_3$	100.0	$g\,mol^{-1}$	Heinze et al. (1999)
Molar weight of opal	67.2	$g\,mol^{-1}$	Heinze et al. (1999)
Molar weight of clay	430.51	$g\,mol^{-1}$	Heinze et al. (1999)
Terrestrial clay flux	0.8	$g\,m^{-2}yr^{-1}$	Roth et al. (2014)
Rate constant for $CaCO_3$ redissolution	800	$l\,mol^{-1}yr^{-1}$	Jeltsch-Thömmes et al. (2019)
Rate constant for opal redissolution	20	$l\,mol^{-1}yr^{-1}$	Tschumi et al. (2011)
Rate constant for oxydation	100	$l\,mol^{-1}yr^{-1}$	Roth et al. (2014)
Saturation concentration for pore water silicic acid	800	$\mu mol\,l^{-1}$	Heinze et al. (1999)
Pore water diffusion coefficient	5.5×10^{-6}	cm^2s^{-1}	Jeltsch-Thömmes et al. (2019)
Bioturbation diffusion coefficient	15×10^{-3}	cm^2yr^{-1}	Heinze et al. (1999)
Redfield coefficient for phosphate	1	-	Anderson and Sarmiento (1994)
Redfield coefficient for oxygen	170	-	Anderson and Sarmiento (1994)
Redfield coefficient for nitrate	16	-	Anderson and Sarmiento (1994)
Redfield coefficient for carbon	117	-	Anderson and Sarmiento (1994)
Redfield coefficient for Alkalinity	-17	-	Roth et al. (2014)

References

Anderson, L. A. and Sarmiento, J. L.: Redfield ratios of remineralization determined by nutrient data analysis, Global Biogeochemical Cycles, 8, 65–80, https://doi.org/10.1029/93GB03318, 1994.

Archer, D. and Brovkin, V.: The millennial atmospheric lifetime of anthropogenic CO2, Climatic Change, 90, 283–297, https://doi.org/10.1007/s10584-008-9413-1, 2008.

5

Archer, D., Kheshgi, H., and Maier-Reimer, E.: Multiple timescales for neutralization of fossil fuel CO2, Geophysical Research Letters, 24, 405–408, https://doi.org/10.1029/97GL00168, 1997.

Archer, D., Kheshgi, H., and Maier-Reimer, E.: Dynamics of fossil fuel CO2 neutralization by marine CaCO3, Global Biogeochemical Cycles, 12, 259–276, https://doi.org/10.1029/98GB00744, 1998.

10 Archer, D., Eby, M., Brovkin, V., Ridgwell, A., Cao, L., Mikolajewicz, U., Caldeira, K., Matsumoto, K., Munhoven, G., Montenegro, A., and Tokos, K.: Atmospheric Lifetime of Fossil Fuel Carbon Dioxide, Annual Review of Earth and Planetary Sciences, 37, 117–134, https://doi.org/10.1146/annurev.earth.031208.100206, 2009.

Battaglia, G. and Joos, F.: Marine N2O Emissions From Nitrification and Denitrification Constrained by Modern Observations and Projected in Multimillennial Global Warming Simulations, Global Biogeochemical Cycles, 32, 92–121, https://doi.org/10.1002/2017GB005671, 2018a.

Battaglia, G. and Joos, F.: Hazards of decreasing marine oxygen: the near-term and millennial-scale benefits of meeting the Paris climate targets, Earth System Dynamics, 9, 797–816, https://doi.org/10.5194/esd-2017-90, 2018b.

Battaglia, G., Steinacher, M., and Joos, F.: A probabilistic assessment of calcium carbonate export and dissolution in the modern ocean, Biogeosciences, 13, 2823–2848, https://doi.org/10.5194/bg-13-2823-2016, 2016.

Bauska, T. K., Baggenstos, D., Brook, E. J., Mix, A. C., Marcott, S. A., Petrenko, V. V., Schaefer, H., Severinghaus, J. P., and Lee, J. E.: Carbon isotopes characterize rapid changes in atmospheric carbon dioxide during the last deglaciation, Proceedings of the National Academy of Sciences, 113, 3465–3470, https://doi.org/10.1073/pnas.1513868113, 2016.

Bauska, T. K., Brook, E. J., Marcott, S. A., Baggenstos, D., Shackleton, S., Severinghaus, J. P., and Petrenko, V. V.: Controls on Millennial-Scale Atmospheric CO2 Variability During the Last Glacial Period, Geophysical Research Letters, 45, 7731–7740, https://doi.org/10.1029/2018GL077881, 2018.

Bereiter, B., Eggleston, S., Schmitt, J., Nehrbass-Ahles, C., Stocker, T. F., Fischer, H., Kipfstuhl, S., and Chappellaz, J.: Revision of the EPICA Dome C CO2 record from 800 to 600 kyr before present, Geophysical Research Letters, 42, 542–549, https://doi.org/10.1002/2014GL061957, 2015.

Brovkin, V., Ganopolski, A., Archer, D., and Munhoven, G.: Glacial CO2 cycle as a succession of key physical and biogeochemical processes, Climate of the Past, 8, 251–264, https://doi.org/10.5194/cp-8-251-2012, 2012.

Colbourn, G., Ridgwell, A., and Lenton, T. M.: The Rock Geochemical Model (RokGeM) v0.9, Geoscientific Model Development, 6, 1543–1573, https://doi.org/10.5194/gmd-6-1543-2013, 2013.

Colbourn, G., Ridgwell, A., and Lenton, T. M.: The time scale of the silicate weathering negative feedback on atmospheric CO2, Global Biogeochemical Cycles, 29, 583–596, https://doi.org/10.1002/2014GB005054, 2015.

Collatz, G. J., Berry, J. A., and Clark, J. S.: Effects of climate and atmospheric CO 2 partial pressure on the global distribution of C 4 grasses: present, past, and future, Oecologia, 114, 441–454, https://doi.org/10.1007/s004420050468, 1998.

Dawson, A.: eofs: A Library for EOF Analysis of Meteorological, Oceanographic, and Climate Data, Journal of Open Research Software, 4, 4–7, https://doi.org/10.5334/jors.122, 2016.

Dickson, A. G., Sabine, C. L., and Christian, J. R., eds.: Guide to Best Practices for Ocean CO2 Measurements, PICES Special Publication 3, 2007.

Edwards, N. R., Willmott, A. J., and Killworth, P. D.: On the Role of Topography and Wind Stress on the Stability of the Thermohaline Circulation, Journal of Physical Oceanography, 28, 756–778, https://doi.org/10.1175/1520-0485(1998)028<0756:OTROTA>2.0.CO;2, 1998.

Eggleston, S., Schmitt, J., Bereiter, B., Schneider, R., and Fischer, H.: Evolution of the stable carbon isotope composition of atmospheric CO2 over the last glacial cycle, Paleoceanography, 31, 434–452, https://doi.org/10.1002/2015PA002874, 2016.

Enting, I. G., Wigley, T. M. L., and Heimann, M.: Future Emissions and Concentrations of Carbon Dioxide : Key Ocean / Atmosphere / Land Analyses, CSIRO, Division of Atmospheric Research Technical Paper, 31, 1–133, 1994.

Farquhar, G. D., von Caemmerer, S., and Berry, J. A.: A biochemical model of photosynthetic CO2 assimilation in leaves of C3 species, Planta, 149, 78–90, https://doi.org/10.1007/BF00386231, 1980.

Freeman, K. H. and Hayes, J. M.: Fractionation of carbon isotopes by phytoplankton and estimates of ancient CO 2 levels, Global Biogeochemical Cycles, 6, 185–198, https://doi.org/10.1029/92GB00190, 1992.

Ganopolski, A. and Brovkin, V.: Simulation of climate, ice sheets and CO2 evolution during the last four glacial cycles with an Earth system model of intermediate complexity, Climate of the Past, 13, 1695–1716, https://doi.org/10.5194/cp-13-1695-2017, 2017.

Griffies, S. M.: The GentâMcWilliams Skew Flux, Journal of Physical Oceanography, 28, 831–841, https://doi.org/10.1175/1520-0485(1998)028<0831:TGMSF>2.0.CO;2, 1998.

5 Harris, I., Jones, P. D., Osborn, T. J., and Lister, D. H.: Updated high-resolution grids of monthly climatic observations - the CRU TS3.10 Dataset, International Journal of Climatology, 34, 623–642, https://doi.org/10.1002/joc.3711, 2014.

Haxeltine, A. and Prentice, I. C.: BIOME3: An equilibrium terrestrial biosphere model based on ecophysiological constraints, resource availability, and competition among plant functional types, Global Biogeochemical Cycles, 10, 693–709, https://doi.org/10.1029/96GB02344, http://doi.wiley.com/10.1029/96GB02344, 1996a.

10 Haxeltine, A. and Prentice, I. C.: A General Model for the Light-Use Efficiency of Primary Production, Functional Ecology, 10, 551, https://doi.org/10.2307/2390165, 1996b.

Heinze, C., Maier-Reimer, E., Winguth, A. M. E., and Archer, D.: A global oceanic sediment model for long-term climate studies, Global Biogeochemical Cycles, 13, 221–250, https://doi.org/10.1029/98GB02812, 1999.

Hoogakker, B. A., Rohling, E. J., Palmer, M. R., Tyrrell, T., and Rothwell, R. G.: Underlying causes for long-term global ocean $\delta 13C$ fluctuations over the last 1.20 Myr, Earth and Planetary Science Letters, 248, 15–29, https://doi.org/10.1016/j.epsl.2006.05.007, 2006.

15 Hooss, G., Voss, R., Hasselmann, K., Maier-Reimer, E., and Joos, F.: A nonlinear impulse response model of the coupled carbon cycle-climate system (NICCS), Climate Dynamics, 18, 189–202, https://doi.org/10.1007/s003820100170, 2001.

Jeltsch-Thömmes, A., Battaglia, G., Cartapanis, O., Jaccard, S. L., and Joos, F.: Low terrestrial carbon storage at the Last Glacial Maximum: constraints from multi-proxy data, Climate of the Past, 15, 849–879, https://doi.org/10.5194/cp-15-849-2019, 2019.

20 Joos, F. and Bruno, M.: Pulse response functions are cost-efficient tools to model the link between carbon emissions, atmospheric CO2 and global warming, Physics and Chemistry of The Earth, 21, 471–476, https://doi.org/10.1016/S0079-1946(97)81144-5, 1996.

Joos, F., Bruno, M., Fink, R., Siegenthaler, U., Stocker, T. F., and LeQuere, C.: An efficient and accurate representation of complex oceanic and biospheric models of anthropogenic carbon uptake, Tellus B: Chemical and Physical Meteorology, 48, 397–417, https://doi.org/10.1034/j.1600-0889.1996.t01-2-00006.x, 1996.

25 Joos, F., Prentice, I. C., Sitch, S., Meyer, R., Hooss, G., Plattner, G.-k., Gerber, S., and Hasselmann, K.: Global warming feedbacks on terrestrial carbon uptake under the Intergovernmental Panel on Climate Change (IPCC) Emission Scenarios, Global Biogeochemical Cycles, 15, 891–907, https://doi.org/10.1029/2000GB001375, 2001.

Joos, F., Roth, R., Fuglestvedt, J. S., Peters, G. P., Enting, I. G., Von Bloh, W., Brovkin, V., Burke, E. J., Eby, M., Edwards, N. R., Friedrich, T., Frölicher, T. L., Halloran, P. R., Holden, P. B., Jones, C., Kleinen, T., Mackenzie, F. T., Matsumoto, K., Meinshausen, M., Plattner, G. K.,
30 Reisinger, A., Segschneider, J., Shaffer, G., Steinacher, M., Strassmann, K., Tanaka, K., Timmermann, A., and Weaver, A. J.: Carbon dioxide and climate impulse response functions for the computation of greenhouse gas metrics: A multi-model analysis, Atmospheric Chemistry and Physics, 13, 2793–2825, https://doi.org/10.5194/acp-13-2793-2013, 2013.

Kalnay, E., Kanamitsu, M., Kistler, R., Collins, W., Deaven, D., Gandin, L., Iredell, M., Saha, S., White, G., Woollen, J., Zhu, Y., Chelliah, M., Ebisuzaki, W., Higgins, W., Janowiak, J., Mo, K. C., Ropelewski, C., Wang, J., Leetmaa, A., Reynolds, R., Jenne, R., and Joseph, D.:
35 The NCEP/NCAR 40-year reanalysis project, https://doi.org/10.1175/1520-0477(1996)077<0437:TNYRP>2.0.CO;2, 1996.

Keller, D. P., Lenton, A., Scott, V., Vaughan, N. E., Bauer, N., Ji, D., Jones, C. D., Kravitz, B., Muri, H., and Zickfeld, K.: The Carbon Dioxide Removal Model Intercomparison Project (CDRMIP): Rationale and experimental protocol for CMIP6, Geoscientific Model Development, 11, 1133–1160, https://doi.org/10.5194/gmd-11-1133-2018, 2018.

Keller, K. M., Lienert, S., Bozbiyik, A., Stocker, T. F., Churakova Sidorova, O. V., Frank, D. C., Klesse, S., Koven, C. D., Leuenberger, M., Riley, W. J., Saurer, M., Siegwolf, R., Weigt, R. B., and Joos, F.: 20th century changes in carbon isotopes and water-use efficiency: Tree-ring-based evaluation of the CLM4.5 and LPX-Bern models, Biogeosciences, 14, 2641–2673, https://doi.org/10.5194/bg-14-2641-2017, 2017.

5 Köhler, P., Fischer, H., and Schmitt, J.: Atmospheric δ13CO2 and its relation to pCO2 and deep ocean δ13C during the late Pleistocene, Paleoceanography, 25, PA1213, https://doi.org/10.1029/2008PA001703, 2010.

Köhler, P., Knorr, G., Buiron, D., Lourantou, A., and Chappellaz, J.: Abrupt rise in atmospheric CO2 at the onset of the Bølling/Allerød: in-situ ice core data versus true atmospheric signals, Climate of the Past, 7, 473–486, https://doi.org/10.5194/cp-7-473-2011, 2011.

Krakauer, N. Y., Randerson, J. T., Primeau, F. W., Gruber, N., and Menemenlis, D.: Carbon isotope evidence for the latitudinal distribution
10   and wind speed dependence of the air-sea gas transfer velocity, Tellus, Series B: Chemical and Physical Meteorology, 58, 390–417, https://doi.org/10.1111/j.1600-0889.2006.00223.x, 2006.

Lienert, S. and Joos, F.: A Bayesian ensemble data assimilation to constrain model parameters and land-use carbon emissions, Biogeosciences, 15, 2909–2930, https://doi.org/10.5194/bg-15-2909-2018, 2018.

Lindgren, A., Hugelius, G., and Kuhry, P.: Extensive loss of past permafrost carbon but a net accumulation into present-day soils, Nature,
15   560, 219–222, https://doi.org/10.1038/s41586-018-0371-0, 2018.

Lloyd, J. and Farquhar, G. D.: 13C discrimination during CO2 assimilation by the terrestrial biosphere, Oecologia, 99, 201–215, https://doi.org/10.1007/BF00627732, 1994.

Lord, N. S., Ridgwell, A., Thorne, M. C., and Lunt, D. J.: An impulse response function for the âlong tailâ of excess atmospheric CO2 in an Earth system model, Global Biogeochemical Cycles, 30, 2–17, https://doi.org/10.1002/2014GB005074, 2016.

20 Lourantou, A., Chappellaz, J., Barnola, J. M., Masson-Delmotte, V., and Raynaud, D.: Changes in atmospheric CO2 and its carbon isotopic ratio during the penultimate deglaciation, Quaternary Science Reviews, 29, 1983–1992, https://doi.org/10.1016/j.quascirev.2010.05.002, 2010.

Lüthi, D., Le Floch, M., Bereiter, B., Blunier, T., Barnola, J. M., Siegenthaler, U., Raynaud, D., Jouzel, J., Fischer, H., Kawamura, K., and Stocker, T. F.: High-resolution carbon dioxide concentration record 650,000-800,000 years before present, Nature, 453, 379–382,
25   https://doi.org/10.1038/nature06949, 2008.

Maier-Reimer, E. and Hasselmann, K.: Transport and storage of CO2 in the ocean ——an inorganic ocean-circulation carbon cycle model, Climate Dynamics, 2, 63–90, https://doi.org/10.1007/BF01054491, 1987.

Marcott, S. a., Bauska, T. K., Buizert, C., Steig, E. J., Rosen, J. L., Cuffey, K. M., Fudge, T. J., Severinghaus, J. P., Ahn, J., Kalk, M. L., McConnell, J. R., Sowers, T., Taylor, K. C., White, J. W. C., and Brook, E. J.: Centennial-scale changes in the global carbon cycle during
30   the last deglaciation., Nature, 514, 616–9, https://doi.org/10.1038/nature13799, 2014.

Menviel, L. and Joos, F.: Toward explaining the Holocene carbon dioxide and carbon isotope records: Results from transient ocean carbon cycle-climate simulations, Paleoceanography, 27, PA1207, https://doi.org/10.1029/2011PA002224, 2012.

Menviel, L., Joos, F., and Ritz, S. P.: Simulating atmospheric CO2, 13C and the marine carbon cycle during the Last Glacial-Interglacial cycle: Possible role for a deepening of the mean remineralization depth and an increase in the oceanic nutrient inventory, Quaternary
35   Science Reviews, 56, 46–68, https://doi.org/10.1016/j.quascirev.2012.09.012, 2012.

Menviel, L., Mouchet, A., Meissner, K. J., Joos, F., and England, M. H.: Impact of oceanic circulation changes on atmospheric d13CO2, Global Biogeochemical Cycles, 29, 1944–1961, https://doi.org/10.1002/2015GB005207, 2015.

Mook, W.: 13C in atmospheric CO2, Netherlands Journal of Sea Research, 20, 211–223, https://doi.org/10.1016/0077-7579(86)90043-8, 1986.

Müller, S. A., Joos, F., Edwards, N. R., and Stocker, T. F.: Water Mass Distribution and Ventilation Time Scales in a Cost-Efficient, Three-Dimensional Ocean Model, Journal of Climate, 19, 5479–5499, https://doi.org/10.1175/JCLI3911.1, 2006.

5   Najjar, R. G. and Orr, J. C.: Biotic-HOWTO. Internal OCMIP, Tech. rep., LSCE/CEA, Saclay, Gif-sur-Yvette, France, 1999.

Neftel, A., Oeschger, H., Schwander, J., Stauffer, B., and Zumbrunn, R.: Ice core sample measurements give atmospheric CO2 content during the past 40,000 yr, Nature, 295, 220–223, https://doi.org/10.1038/295220a0, 1982.

Oliver, K. I. C., Hoogakker, B. A. A., Crowhurst, S., Henderson, G. M., Rickaby, R. E. M., Edwards, N. R., and Elderfield, H.: A synthesis of marine sediment core d13C data over the last 150 000 years, Climate of the Past, 6, 645–673, https://doi.org/10.5194/cp-6-645-2010, 10   2010.

Orr, J. C. and Epitalon, J. M.: Improved routines to model the ocean carbonate system: Mocsy 2.0, Geoscientific Model Development, 8, 485–499, https://doi.org/10.5194/gmd-8-485-2015, 2015.

Orr, J. C., Najjar, R., Sabine, C. L., and Joos, F.: Abiotic-HOWTO. Internal OCMIP, Tech. rep., LSCE/CEA, Saclay, Gif-sur-Yvette, France, 1999.

15   Orr, J. C., Najjar, R. G., Aumont, O., Bopp, L., Bullister, J. L., Danabasoglu, G., Doney, S. C., Dunne, J. P., Dutay, J. C., Graven, H., Griffies, S. M., John, J. G., Joos, F., Levin, I., Lindsay, K., Matear, R. J., McKinley, G. A., Mouchet, A., Oschlies, A., Romanou, A., Schlitzer, R., Tagliabue, A., Tanhua, T., and Yool, A.: Biogeochemical protocols and diagnostics for the CMIP6 Ocean Model Intercomparison Project (OMIP), Geoscientific Model Development, 10, 2169–2199, https://doi.org/10.5194/gmd-10-2169-2017, 2017.

Parekh, P., Joos, F., and Müller, S. A.: A modeling assessment of the interplay between aeolian iron fluxes and iron-binding ligands in control-20   ling carbon dioxide fluctuations during Antarctic warm events, Paleoceanography, 23, PA4202, https://doi.org/10.1029/2007PA001531, 2008.

Peltier, W. R.: Ice Age Paleotopography, Science, 265, 195 – 201, 1994.

Revelle, R. and Suess, H. E.: Carbon Dioxide Exchange Between Atmosphere and Ocean and the Question of an Increase of Atmospheric CO2 during the Past Decades, Tellus, 9, 18–27, https://doi.org/10.1111/j.2153-3490.1957.tb01849.x, 1957.

25   Ridgwell, A. and Hargreaves, J. C.: Regulation of atmospheric CO 2 by deep-sea sediments in an Earth system model, Global Biogeochemical Cycles, 21, GB2008, https://doi.org/10.1029/2006GB002764, 2007.

Ritz, S., Stocker, T., and Joos, F.: A Coupled Dynamical Ocean-Energy Balance Atmosphere Model for Paleoclimate Studies, Journal of Climate, 24, 349–375, https://doi.org/10.1175/2010JCLI3351.1, 2011.

Roth, R. and Joos, F.: Model limits on the role of volcanic carbon emissions in regulating glacial-interglacial CO2variations, Earth and 30   Planetary Science Letters, 329-330, 141–149, https://doi.org/10.1016/j.epsl.2012.02.019, 2012.

Roth, R., Ritz, S. P., and Joos, F.: Burial-nutrient feedbacks amplify the sensitivity of atmospheric carbon dioxide to changes in organic matter remineralisation, Earth System Dynamics, 5, 321–343, https://doi.org/10.5194/esd-5-321-2014, 2014.

Sarmiento, J. L., Orr, J. C., and Siegenthaler, U.: A perturbation simulation of CO2 uptake in an ocean general circulation model, Journal of Geophysical Research: Oceans, 97, 3621–3645, https://doi.org/10.1029/91JC02849, 1992.

35   Schimel, D., Alves, D., Enting, I. G., Heimann, M., Joos, F., Raynaud, D., and Wigley, T. M. L.: CO2 and the carbon cycle, in: Climate Change 1995 The Science of Climate Change Contribution of Working Group I to the Second Assessment Report of the Intergovernmental Panel on Climate Change, edited by J. T. Houghton, L. G. Meiro Filho, B. A. Callander, N. Harris, A. K. and Maskell, K., pp. 76–86, Cambridge University Press, 1996.

Schmitt, J., Schneider, R., Elsig, J., Leuenberger, D., Lourantou, a., Chappellaz, J., Kohler, P., Joos, F., Stocker, T. F., Leuenberger, M., and Fischer, H.: Carbon Isotope Constraints on the Deglacial CO2 Rise from Ice Cores, Science, 336, 711–714, https://doi.org/10.1126/science.1217161, 2012.

Schneider, R., Schmitt, J., Köhler, P., Joos, F., and Fischer, H.: A reconstruction of atmospheric carbon dioxide and its stable carbon isotopic composition from the penultimate glacial maximum to the last glacial inception, Climate of the Past, 9, 2507–2523, https://doi.org/10.5194/cp-9-2507-2013, 2013.

Siegenthaler, U. and Joos, F.: Use of a simple model for studying oceanic tracer distributions and the global carbon cycle, Tellus B: Chemical and Physical Meteorology, 44, 186–207, https://doi.org/10.1034/j.1600-0889.1992.t01-2-00003.x, 1992.

Siegenthaler, U. and Oeschger, H.: Predicting future atmospheric carbon dioxide levels, Science, 199, 388–395, https://doi.org/10.1126/science.199.4327.388, 1978.

Siegenthaler, U. and Oeschger, H.: Biospheric CO2 emissions during the past 200 years reconstructed by deconvolution of ice core data, Tellus B: Chemical and Physical Meteorology, 39, 140–154, https://doi.org/10.3402/tellusb.v39i1-2.15331, 1987.

Siegenthaler, U., Stocker, T. F., Monnin, E., Lüthi, D., Schwander, J., Stauffer, B., Raynaud, D., Barnola, J.-M., Fischer, H., Masson-Delmotte, V., and Jouzel, J.: Stable Carbon Cycle-Climate Relationship During the Late Pleistocene, Science, 310, 1313–1317, 2005.

Sitch, S., Smith, B., Prentice, I. C., Arneth, A., Bondeau, A., Cramer, W., Kaplan, J. O., Levis, S., Lucht, W., Sykes, M. T., Thonicke, K., and Venevsky, S.: Evaluation of ecosystem dynamics, plant geography and terrestrial carbon cycling in the LPJ dynamic global vegetation model, Global Change Biology, 9, 161–185, https://doi.org/10.1046/j.1365-2486.2003.00569.x, 2003.

Skinner, L. C., Fallon, S., Waelbroeck, C., Michel, E., Barker, S., Klug, A., Stark, A., Peters, K., Schnering, H. G., Umemoto, K., Yamaguchi, K., Fujita, M., Powers, R. E., Parac, T. N., Raymond, K. N., Olenyuk, B., Muddiman, D. C., Smith, R. D., Whiteford, J. A., Stang, P. J., Levin, M. D., Shield, J. E., Egan, S. J., Robson, R., Dress, A. W. M., Roy, S., Ni, Z., Yaghi, O. M., Lu, J., Mondal, A., Zaworotko, M. J., Atwood, J. L., Tominaga, M., Kawano, M., Tang, C., Wiesenfeld, K., Gustafson, S., Pelta, D. A., Verdegay, J. L., Systems, B., Pelzing, M., Skinner, L. C., Fallon, S., Waelbroeck, C., Michel, E., and Barker, S.: Ventilation of the Deep Southern Ocean and Deglacial CO2 Rise, Science, 328, 1147–1151, https://doi.org/10.1126/science.1183627, 2010.

Skinner, L. C., Primeau, F., Freeman, E., de la Fuente, M., Goodwin, P. A., Gottschalk, J., Huang, E., McCave, I. N., Noble, T. L., and Scrivner, A. E.: Radiocarbon constraints on the glacial ocean circulation and its impact on atmospheric CO2, Nature Communications, 8, 16 010, https://doi.org/10.1038/ncomms16010, 2017.

Stocker, B. D., Roth, R., Joos, F., Spahni, R., Steinacher, M., Zaehle, S., Bouwman, L., Xu-Ri, and Prentice, I. C.: Multiple greenhouse-gas feedbacks from the land biosphere under future climate change scenarios, Nature Climate Change, 3, 666–672, https://doi.org/10.1038/nclimate1864, 2013.

Tarnocai, C., Canadell, J. G., Schuur, E. A. G., Kuhry, P., Mazhitova, G., and Zimov, S.: Soil organic carbon pools in the northern circumpolar permafrost region, Global Biogeochemical Cycles, 23, GB2023, https://doi.org/10.1029/2008GB003327, http://doi.wiley.com/10.1029/2008GB003327, 2009.

Tschumi, T., Joos, F., Gehlen, M., and Heinze, C.: Deep ocean ventilation, carbon isotopes, marine sedimentation and the deglacial CO2 rise, Climate of the Past, 7, 771–800, https://doi.org/10.5194/cp-7-771-2011, 2011.

Wanninkhof, R.: Relationship between wind speed and gas exchange over the ocean, Journal of Geophysical Research, 97, 7373–7382, https://doi.org/10.1029/92JC00188, 1992.

Wanninkhof, R.: Relationship between wind speed and gas exchange over the ocean revisited, Limnology and Oceanography: Methods, 12, 351–362, https://doi.org/10.4319/lom.2014.12.351, 2014.